Physicochemical Mechanics of Surfactant-Enhanced Boiling Heat Transfer

by

Han-Jae Jeremy Cho

B.S.E., University of Michigan (2009)
S.M., Massachusetts Institute of Technology (2011)

Submitted to the Department of Mechanical Engineering
in partial fulfillment of the requirements for the degree of

Doctor of Philosophy

at the

MASSACHUSETTS INSTITUTE OF TECHNOLOGY

February 2017

Signature redacted

Author .....
Department of Mechanical Engineering
January 17, 2017

Signature redacted

Certified by .. ..
Evelyn N. Wang
Associate Professor of Mechanical Engineering
Thesis Supervisor

Signature redacted

Accepted by .....
Rohan Abeyaratne
Chairman, Department Committee on Graduate Theses

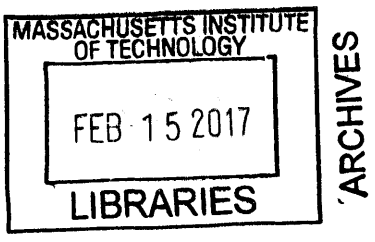

Physicochemical Mechanics of Surfactant-Enhanced Boiling Heat Transfer

by

Han-Jae Jeremy Cho

Submitted to the Department of Mechanical Engineering
on January 17, 2017, in partial fulfillment of the
requirements for the degree of
Doctor of Philosophy

Abstract

Boiling—employed in a variety of industrial and domestic processes such as in power stations, heating/cooling systems, and desalination plants—is involved with a major portion of the world's energy usage. Its substantial utility can be attributed to moving a large quantity of heat over small temperature differences. However, even these small temperature differences can have implications on energy efficiency, device lifetime, and performance. Surfactants, which are molecules that have hydrophobic and hydrophilic components, are known to enhance boiling by changing the way bubbles nucleate on the surface, grow, and depart from the surface. This thesis provides a mechanistic understanding of surfactant enhanced boiling from molecular and macroscopic perspectives with theory and experiments. First, a statistical mechanical model to predict equilibrium and dynamic surface tension from molecular parameters is introduced and experimentally verified. Then, models of bubble nucleation, growth, and departure are developed, taking into account the time-dependent nature of surfactant adsorption processes. From there, models are combined so as to predict the enhancement in boiling performance based primarily on molecular information of the surfactant. Pool boiling experiments conducted with a variety of surfactants have shown agreement with model predictions. With the framework presented in this thesis, large-head and long-tail surfactants were found to be desirable. However, suitable surfactants for specific needs can now be identified, which can aid in the further adoption of surfactants in practice. Finally, using insights gained about the importance of solid-liquid adsorption over liquid-vapor adsorption, a novel method of using electric fields to control surfactant adsorption wherein bubbles can be turned "on" and "off" is demonstrated. Furthermore, an ability to control boiling spatially in addition to temporally is shown. This *active control* of boiling can improve performance and flexibility in existing boiling technologies as well as enable emerging or unprecedented thermal applications.

Thesis Supervisor: Evelyn N. Wang
Title: Associate Professor of Mechanical Engineering

Acknowledgments

I would like to acknowledge my advisor, Prof. Evelyn Wang, whom I am exceptionally fortunate to have had the opportunity to work under. She provided an extremely supportive and engaging environment to work in, but also afforded me freedom in pursuing my own research interests. I would also like to acknowledge my thesis committee members, Prof. Daniel Blankschtein and Prof. Nicolas Hadjiconstantinou, who imparted invaluable knowledge of molecular science to me, and provided helpful feedback at many points along my PhD journey.

Much of my investigation into surfactants would not have been possible without numerous discussions with Dr. Vishnu Sresht, a former student of Prof. Blankschtein. In addition, many of my Device Research Laboratory my colleagues have been incredibly helpful over the years. In particular, I would like to acknowledge Prof. Shalabh Maroo, Dr. Ryan Enright, Prof. Rishi Raj, Prof. Nenad Miljkovic, Dr. Hank Chu, Dr. Solomon Adera, Heena Mutha, Hyunho Kim, Daniel Preston, Yangying Zhu, Youngsup Song, Dr. Sameer Rao, Dr. Dion Antao, Dr. Jiansheng Feng, and Dr. Banafsheh Barabadi who have contributed to my research endeavors in direct ways. I have also had the good fortune of mentoring several outstanding undergraduate students: Jenny Qiu, Diane Kayitesi, Jordan Mizerak, Darci Reed, and Mohamed Ouarrak. I would not have gained key insights about my research without their hard work.

This thesis would not have been possible without the generosity of various organizations. Two funding agencies in particular, the National Science Foundation (through the Center for Materials Science and Engineering, MIT's MRSEC facility) and the Singapore-MIT Alliance for Research and Technology, have primarily funded my work. I also acknowledge Dr. Anat Shiloach, of Unilever, who was gracious enough to allow me to use their bubble tensiometer. Numerous MIT facilities have also been tremendously valuable to my work such as the Microsystems Technology Laboratories, Institute for Soldier Nanotechnologies, Hobby Shop, Edgerton Center, the Swager Group, and the Rohsenow Kendall Laboratory.

Finally, I am immensely grateful for my friends and family who have continually provided support, encouraged me to pursue my goals, and allowed me to indulge in fantastic conversations. But most of all, they have kept me grounded and humble. I am also blessed to have such a patient and loving partner, Candice, who has been my best friend throughout my time at MIT despite geographic separation. In addition, without my parents' dedication to my education, and the trailblazing of my siblings, I could not be at this point today.

CONTENTS

LIST OF FIGURES

LIST OF TABLES

CHAPTER 1

INTRODUCTION

Boiling is the transformation of a liquid into vapor by the formation of bubbles. Water is an essential chemical to all life, but the boiling of water is an anthropogenic activity that has been utilized over millennia as shown in Figure 1-1. Today, boiling is used to generate a majority of electrical power in power plants, for heating/cooling, in chemical processing plants, to treat water, to sterilize, and for numerous other industrial and domestic applications. Despite thousands of years of usage, however, the complete physics of boiling is not fully predictable given that it involves a variety of physical phenomena within the fields of fluid mechanics, heat transfer, and surface chemistry. Recently, though, significant insights into the physical mechanism of boiling have enabled significant improvements in boiling performance that would be beneficial to society given its ubiquity. Recognizing the importance of wetting behavior in boiling, much of the research community has been focused on engineering surfaces with micro- or nano-sized features to enhance boiling performance. Some other work has focused on adding chemicals, such as surfactants, to the liquid which can also improve boiling performance without the need for potentially costly engineered surfaces. Surfactants are molecules that, when dissolved in a liquid, will adsorb to liquid-vapor and solid-liquid interfaces, thereby lowering in-

terfacial energy and altering wetting behavior. While the phenomenon of surfactant enhanced boiling has been observed previously, the comprehensive understanding of the mechanism of enhancement remains elusive. Understanding the phenomenon from a microscopic perspective (physicochemical and molecular behavior) and connecting it to macroscopic behavior (heat-transfer and fluid-mechanics behavior) will be the goal of this thesis.

1.1 Motivation

1.1.1 Brief history of boiling usage

In prehistoric times, the development of pottery enabled cooking of food via boiling [1]. Cooking offers numerous benefits such as killing of harmful pathogens as well as making food more palatable, digestible, and nutritive [2]. Compared to other cooking methods, boiling/simmering in a pot enables direct heating with less constant attention [2]. This can be directly attributed to the high latent heat of water. This allows water to remain near the boiling temperature with minimal liquid loss from evaporation, permitting longer cooking times, even over a powerful heat source such as an open flame.

Usage of boiling outside of cooking began to appear in historic times. In the first century AD, Heron of Alexandria, a Greek mathematician and engineer, invented the *aeolipile*, which is the first known usage of steam for mechanical power. The device consisted a vessel filled with heated water which would generate steam and rotate a spherically-shaped piece. However, researchers believe that these "toys" were used only to teach physics and not for any engineering application [3]. It was not until 1781 when James Watt built the first rotary steam engine, which unlocked an unprecedented mechanical capability that ushered in the Industrial Revolution [4]. By the early 19th century, Richard Trevithick pioneered steam power for locomotive transport. In 1834, Jacob Perkins utilized liquid-vapor phase change (vapor compression cycle) to develop the refrigerator. In the latter 19th century, develop-

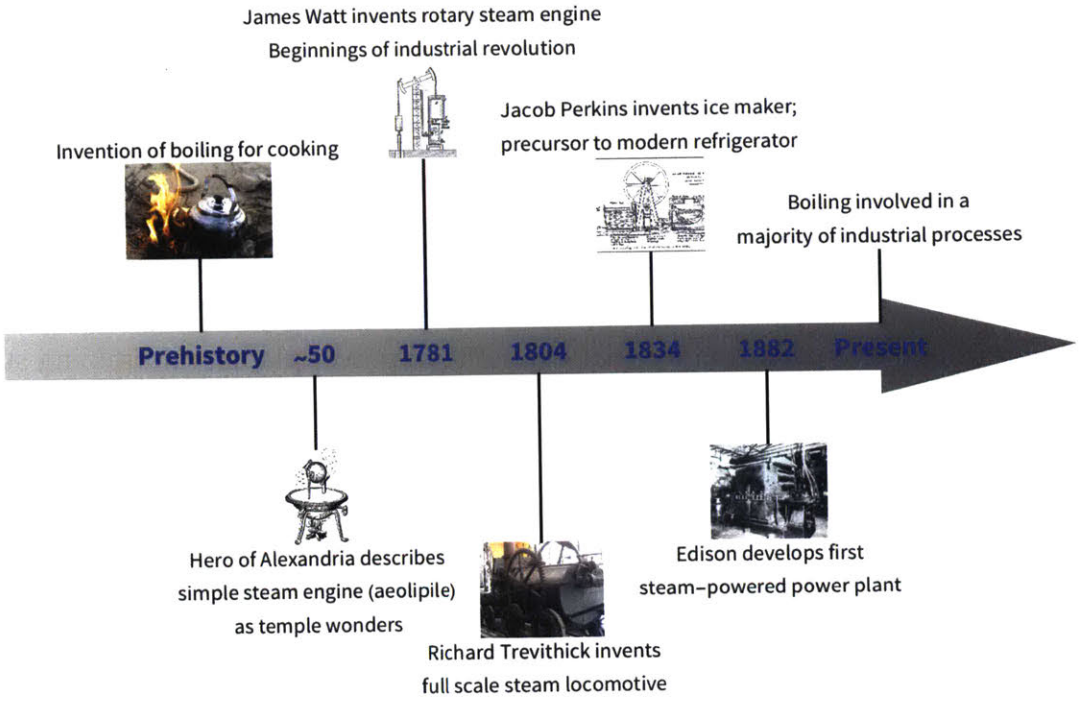

Figure 1-1: **Timeline of milestones in boiling technology.** "Coffee pot on open fire" by Aih. and "TrevithicksEngine" by Igitur are licensed under CC BY 2.0. Pictures of the aeolipile, Watt engine, ice maker, and steam turbine are in the public domain.

ment of the steam turbine in the steam power plant enabled electricity to proliferate. Today, steam-based power plants generate a majority of electricity on the planet [5].

1.1.2 Improving boiling performance

In modern applications, boiling has found immense utility in power generation, water purification, and heating and cooling applications. In addition, steam has many properties that are useful in agriculture, industrial and domestic applications, such as sanitation and sterilization, food processing and chemical processing [6, 7, 8]. Evaporation-condensation cycles are commonly used to purify liquid water in regions of water scarcity [9]. Furthermore, the high heat-transfer capability of phase-change processes, such as in heat pipes, has been useful for thermal management of high-power-density electronics [10]. Recent advancements could usher in new phase-change applications such as miniaturized cooling [11] and solar steam gen-

eration [12]. The growing presence of phase-change processes will continue to emphasize the importance of attaining optimal performance.

Inefficiencies in liquid-vapor phase-change processes primarily manifest themselves as temperature differences, because these embody lost opportunities to extract thermodynamic work (lost exergy). Some superheating or subcooling, is necessary for phase change to occur at an appreciable rate, but minimization of this difference can improve performance. For example, in power plants, minimizing superheat and subcooling at the boiler and condenser, respectively, could improve electrical work output and overall efficiency. Similarly, in a refrigeration cycle, lowering superheat and subcooling at the evaporator and condenser can improve the coefficient of performance. In electronics cooling applications, ineffective heat transfer increases the temperature of the electronic devices, which reduces their lifetime and reliability [13, 14].

The impact of improving boiling technology is, therefore, two-fold. First, small improvements in ubiquitous boiling applications can lead to significant energy savings in world energy consumption. This is particularly important given the broad usage of fossil fuels in boiling applications and concerns about global climate change. Second, new capabilities in boiling could enable unprecedented, highly useful, and disruptive energy technologies, which is becoming increasingly important in a more energy-conscious world.

1.2 Background

1.2.1 The role of wettability

Boiling can be generally described as the nucleation of vapor bubbles on a solid-liquid interface, subsequent growth, and departure from the surface. All of these behaviors depend on wettability, which is the tendency of liquids to stick to surfaces. Let us illustrate wettability concepts in the context of a vapor bubble on a surface as shown in Figure 1-2.

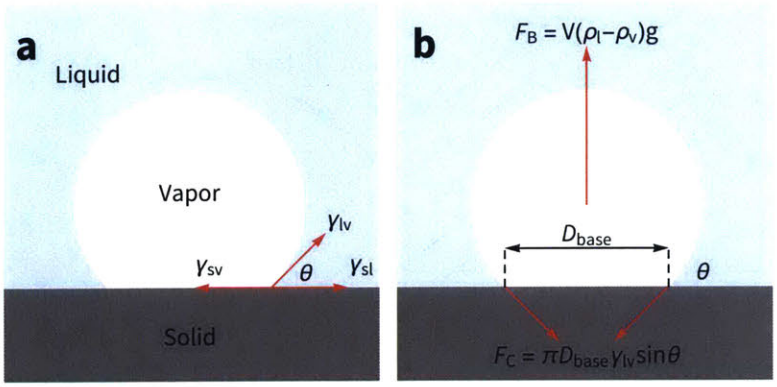

Figure 1-2: **Schematic diagram of a bubble on a surface.** (a) At the three-phase contact line, a horizontal force balance between interfacial tensions occurs. (b) The bubble is being pulled upward due to buoyancy and pulled downward due to surface tension.

Important properties that describe wettability are the contact angle and surface tension (surface energy). The contact angle, θ, is the angle at which a liquid-vapor interface contacts a solid surface (the three-phase contact line), measured from the liquid side (see Figure 1-2a). Along this contact line, a force balance between interfacial (surface) tensions occurs whereby

$$\gamma_{lv}\cos(\theta) = \gamma_{sv} - \gamma_{sl} = \Delta\gamma_s, \tag{1.1}$$

which is the well-known Young equation [15]. Here, γ_{lv}, γ_{sv}, and γ_{sl} are the liquid-vapor, solid-vapor, and solid-liquid interfacial energies, respectively.

Surface tension also holds the bubble adhered to the surface as shown in Figure 1-2b. This force,

$$F_C = \pi D_{base}\gamma_{lv}\sin\theta, \tag{1.2}$$

occurs at the contact line which has a length of πD_{base}. Here, D_{base} is the diameter of the base of the bubble. Meanwhile, buoyancy causes an upward body force for the bubble:

$$F_B = V(\rho_l - \rho_v)g \tag{1.3}$$

where V is the volume of the bubble, ρ_l is the liquid density, ρ_v is the vapor density,

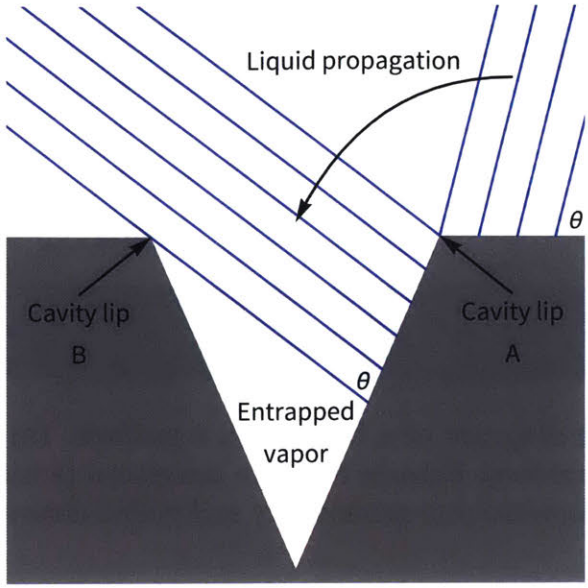

Figure 1-3: **Illustration of liquid propagating over a cavity.** The liquid front (blue lines) moves from right to left and downward into the cavity until a region of vapor is trapped.

and g is the acceleration due to gravity. Once buoyancy overcomes the surface tension force ($F_B > F_C$), then the bubble begins to depart the surface.[1]

In boiling, bubbles grow from nucleation sites. These are usually small vapor regions that exist at cavities or defects on the surface [16]. These entrapped vapor regions occur due to incomplete wetting of the surface across cavities or defects. As an example, let us examine the propagation of a liquid front (liquid-vapor interface) over a cavity as shown in Figure 1-3. The liquid front starts from the right side outside the cavity and propagates left until the contact line reaches cavity lip A. At this point, the liquid-vapor interface will pivot about the cavity lip A until the angle between the liquid-vapor interface and the cavity wall reaches the contact angle. From there, the front will continue to propagate into the cavity until the liquid-vapor interface is cut off by the cavity lip B leaving an entrapped vapor region. This vapor region would then subsequently relax into a shape that has a spherical cap geometry.

Once vapor has been trapped, it does not automatically serve as a nucleation

[1]This is the case in the limit of quasi-static bubble growth and departure behavior where momentum is negligible.

site, however. Due to the curvature of the bubble, the pressure inside the bubble is greater than its liquid surroundings; thus, while the liquid may be at saturation, the vapor could be above the saturation pressure. Assuming a spherical bubble shape, the pressure difference can be calculated using the Young-Laplace equation:

$$\Delta P = \frac{2\gamma_{\mathrm{lv}}}{R_{\mathrm{b}}} \tag{1.4}$$

where R_{b} is the radius of curvature of the bubble. To initiate evaporation and activate the nucleation site, the surrounding liquid needs to be superheated above the saturation temperature in order to bring the vapor to a saturation condition. This additional superheat required can be approximated using the Clausius-Clapeyron relation, which states that

$$\left(\frac{dP}{dT}\right)_{\mathrm{sat}} = \frac{h_{\mathrm{fg}}}{T_{\mathrm{sat}} v_{\mathrm{fg}}} \tag{1.5}$$

where h_{fg} is the specific enthalpy of phase change [$\mathrm{J\,kg^{-1}}$], and v_{fg} is the specific volume difference between liquid and vapor phases [$\mathrm{m^3\,kg^{-1}}$]. Approximating that $\left(\frac{dP}{dT}\right)_{\mathrm{sat}} \approx \frac{\Delta P}{\Delta T_{\mathrm{wall}}}$ and applying the Young-Laplace equation (Eq. 1.4) yields

$$\Delta T_{\mathrm{wall}} = \frac{2\gamma_{\mathrm{lv}} T_{\mathrm{sat}} v_{\mathrm{fg}}}{h_{\mathrm{fg}} R_{\mathrm{b}}}. \tag{1.6}$$

The radius of curvature will depend on the contact angle and cavity geometry. Figure 1-4a shows entrapped vapor regions on a small (α) and a large (β) cavity. For the same material, the contact angle, θ, must be the same for both cavities; as a result, the radius of curvature is smaller for the smaller cavity and the required superheat according to Eq. 1.6 is higher than that of the larger cavity. Hence, for Figure 1-4a, $P_\beta < P_{\mathrm{sat}} < P_\alpha$ and only the larger cavity (β) is active. However, if the contact angle were to be increased to a sufficiently higher value θ' such that $P_\beta < P_\alpha < P_{\mathrm{sat}}$, then both small and large cavities could be activated as shown in Figure 1-4b. Thus, larger contact angles (more hydrophobic surfaces) tend to have higher nucleation densities, which leads to more heat transfer for a given superheat [17]. In effect, larger contact angles can increase the heat-transfer coefficient (HTC)

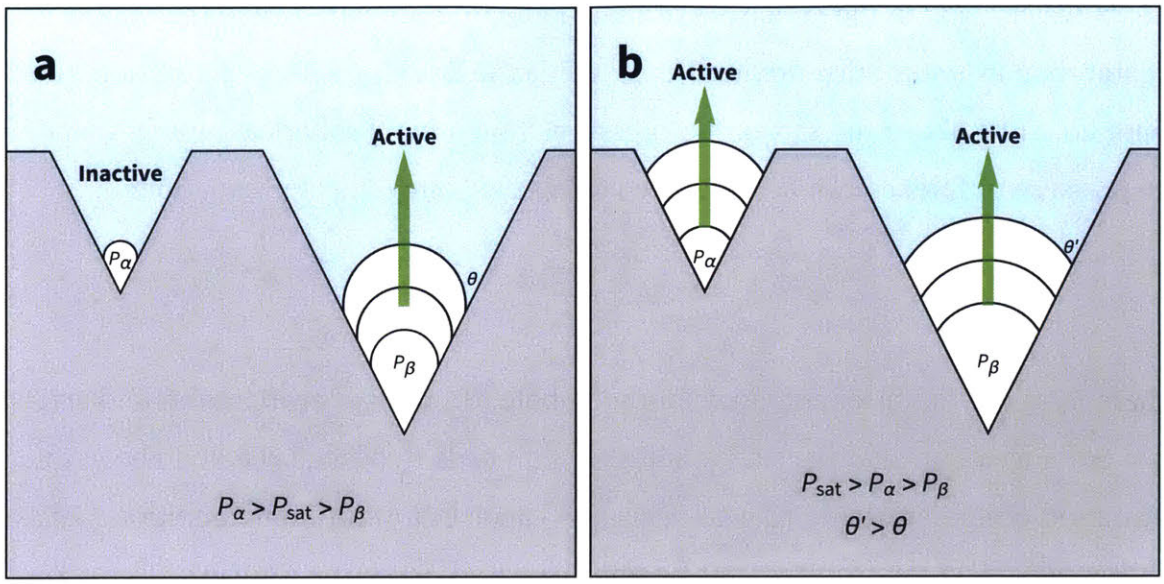

Figure 1-4: **Illustration of enhanced cavity activation.** (a) With a relatively low contact angle, only large cavities with large radii of curvature become active nucleation sites. (b) With higher contact angles—lower bubble pressures—the smaller cavity will be an active nucleation site as well, thereby increasing the overall nucleation density.

which is defined as

$$\text{HTC} = \frac{q''}{\Delta T_{\text{wall}}} \tag{1.7}$$

where q'' is the heat flux [W m^{-2}] and ΔT_{wall} is the difference in temperature between the boiling surface and the saturation temperature (boiling point). The HTC, in effect, describes the effectiveness of the heat-transfer process.

1.2.2 The boiling curve

A common way to evaluate boiling heat-transfer performance is through a boiling curve, which is a plot of heat flux, q'', as a function of wall superheat, ΔT_{wall}. Nukiyama, in 1934, pioneered the use of boiling curves to evaluate performance and identified different regimes of boiling [18]. At low superheats (region A in Figure 1-5), heat transfer is mainly due to natural convection. As the superheat increases, vapor bubbles start to form at the onset of nucleate boiling (ONB) (border of regions A and B). Once bubbles appear in the nucleate boiling regime (region B), they

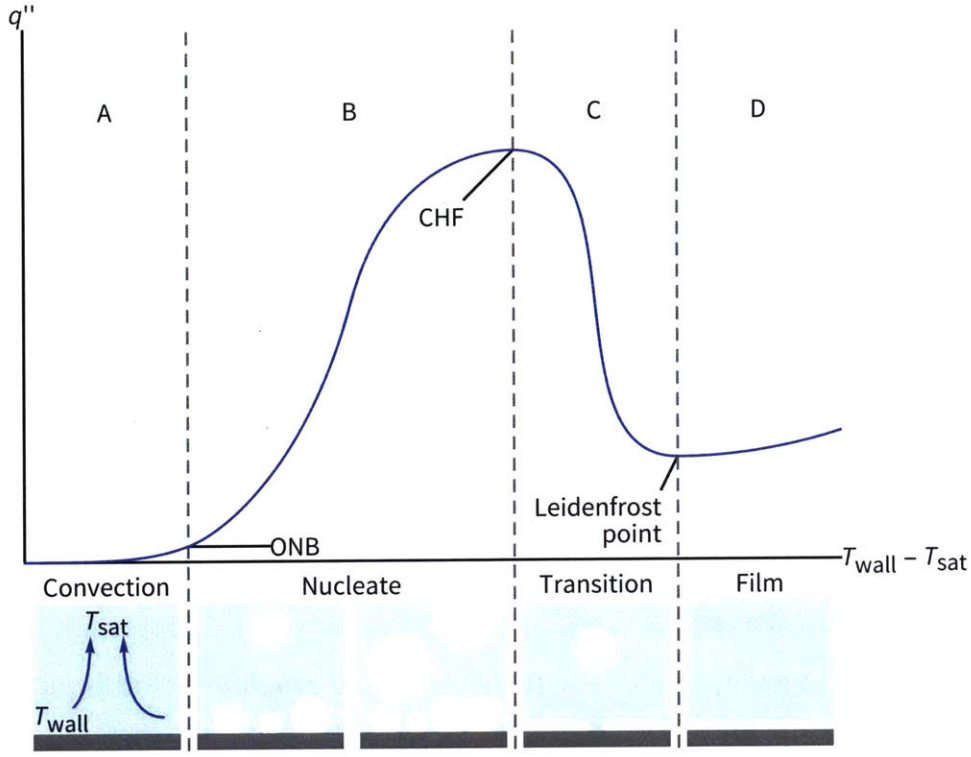

Figure 1-5: **Schematic diagram of a typical boiling curve.** The heat flux (q'') on the y-axis is plotted as a function of the superheat (ΔT) on the x-axis. From lowest to highest superheat, the regimes of boiling are (A) natural convection, (B) nucleate boiling, (C) transition boiling, and (D) film boiling. The onset of nucleate boiling (ONB) occurs at the lowest temperature bubbles are present. In nucleate boiling, heat transfer rises rapidly with an increase in superheat. The critical heat flux (CHF) is the maximum nucleate boiling heat flux. After that, a transition from nucleate to film boiling occurs wherein the temperature rises significantly.

grow until buoyancy overcomes surface tension and the bubble leaves the surface. The repeated growth and departure causes fluid motion that aids in convective heat transfer. The result of this bubble motion induced convection is a sharp increase in the heat flux and the HTC. As the superheat increases, the nucleation density (number of sites from which bubbles grow) increases significantly, giving rise to higher heat transfer rates. Eventually, the high density of vapor bubbles leads to the formation of a vapor film on the heated surface, which acts as a thermal barrier for heat transfer. Once film boiling occurs (region D in Figure 1-5), the temperature increases drastically, usually to the extent of device burn out or catastrophic system failure. The transition to film boiling occurs after the critical heat flux (CHF). As

such, much of the recent research has been focused on strategies to raise the CHF of boiling systems, especially in the context of nuclear power plants and thermal management. In addition, efforts have been made to increase HTC as this can lead to direct improvements in efficiency in many boiling applications that do not require extremely high heat fluxes ($< 100\,\mathrm{W\,cm^{-2}}$).

1.2.3 Boiling surface engineering

In relatively recent work of the past two decades, specially engineered boiling surfaces with micro- and nano-sized features have been shown to have very high CHFs (on the order of several hundred $\mathrm{W\,cm^{-2}}$) as shown in Figure 1-6. Typically, the goal of these surfaces is to enhance wettability via increased roughness. Surfaces that favor wetting and wicking have been shown to prevent dryout/film boiling on the surface [19, 20, 21, 22]. Some examples of structures include nanowires [23, 24, 25], silicon dioxide structured pillars[26], hierarchical structured surfaces [25, 20, 21], sintered particles [27, 28], and nanofluids [29, 30]. Even with the large variety of techniques to enhance wettability, though, most of these surfaces offer similar performance: CHFs of $200\,\mathrm{W\,cm^{-2}}$ to $300\,\mathrm{W\,cm^{-2}}$ at relatively large superheats of 20 °C to 40 °C as shown by the "CHF optimized surfaces" in Figure 1-6a. While some degree of control could be possible by using finer microstructures to effect slightly better HTCs as shown in Figure 1-6b, the HTCs of highly wetting surfaces still remain relatively poor due to high superheats.

More recently, several novel boiling surfaces that employ milliscale features in conjunction with micro/nanoscale features have been shown to have high CHF as well as high HTC (lower superheats). Some examples of these surfaces are biphilic surfaces (heterogeneously wetting surfaces with mixed hydrophobic and hydrophilic zones) [37], microchannels with mixed roughness [36, 38], and biconductive surfaces (heterogeneous surfaces with materials of different thermal conductivity) [35]. These surfaces are designed such that nucleation only occurs on specific areas. The working principle is that nucleation that is more organized leads to more effective

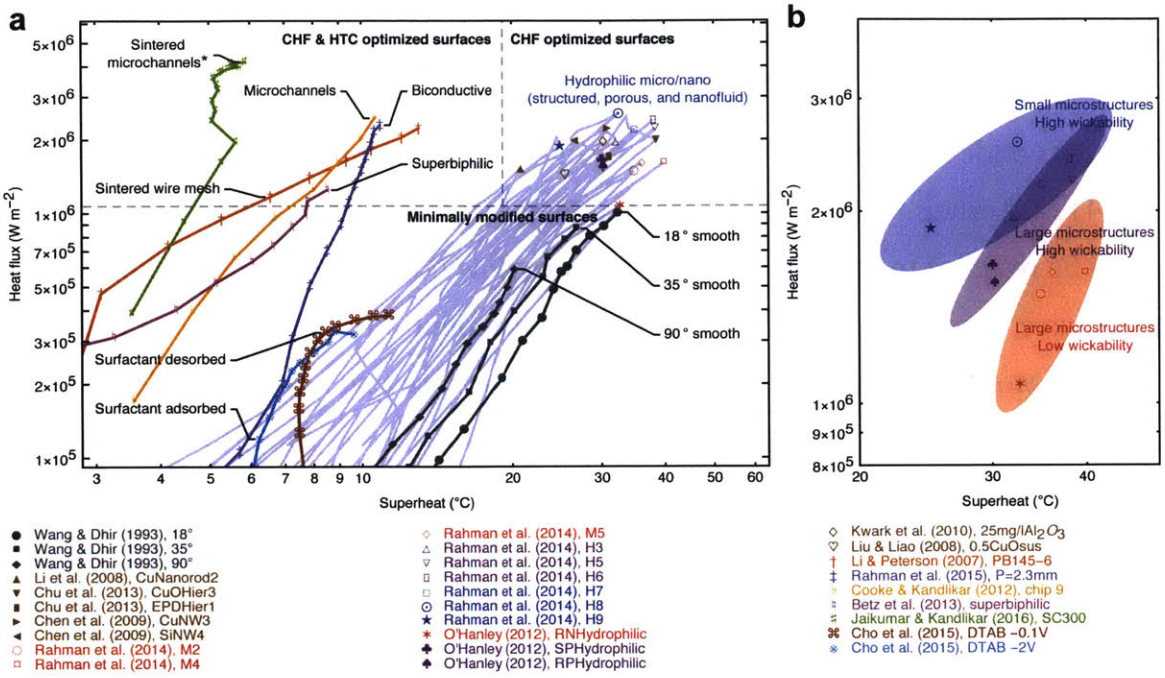

Figure 1-6: **Boiling curves in recent literature.** (a) Boiling curves up to the CHF for various pool-boiling systems reported in the literature. The dependence on contact angle for smooth surfaces is shown in dark grey. The data in the top-right corner is taken from studies in which the CHF was optimized with micro- and nanoscale features and homogenous surface chemistry. The data in the top-left corner data represent work in which both the CHF and HTC were optimized, usually with novel, heterogeneous surfaces. Bottom data points represent work with minimal surface engineering and surfactants in the bulk fluid. (b) CHF values of various micro- and nanostructured surfaces grouped according to microstructure size and wickability. A modified version of this figure appears in our review paper [31]. Data taken from [17, 23, 20, 21, 32, 28, 30, 33, 34, 35, 36, 37, 38, 39].

fluid flow around bubbles thereby increasing convective heat transfer as well as rewetting of the surface underneath departing bubbles so as to prevent film boiling. One significant limitation of surface engineering, however, is the fact that manufacturing these surfaces at large scales are non-trivial and possibly cost-prohibitive. Thus, some researchers have focused on enhancing boiling without modifying the surface; instead, active methods such as electric fields [40] or additives to fluids [41] have also been investigated.

1.2.4 Boiling enhancement with surfactants

Surfactants added to boiling fluids have been known to enhance heat transfer since 1939 [41, 42] when Stroebe used sodium dodecyl sulfate (commonly known as SDS but will be referred to as S12S later) to enhance flow boiling. Since then, numerous studies have shown some degree of HTC enhancement but with some decrease in CHF [41]. Most of the surfactants tested have been those that have been adopted by industry for other purposes, such as SDS, Triton X-100, cetyl trimethylammonium bromide (commonly known as CTAB but will be referred to as 16TAB later), Habon G, and Tween-80. These surfactants are commonly used in food, cosmetic, cleaning, pharmaceutical, and life-science applications, but have not been developed specifically for heat-transfer applications. Despite decades of research, there is no broad consensus of what types of surfactants are ideal for use in boiling, which largely stems from an incomplete understanding of the mechanism of enhancement.

Before delving into surfactants in a boiling context, let us briefly consider some basic surfactant concepts. Surfactants can be generally described as molecules that have a hydrophobic and hydrophilic component. The hydrophobic component is typically some sort of hydrocarbon and is often referred to as a "tail" since these are often hydrocarbon chains (this thesis will mainly focus on alkyl chains). The hydrophilic component is often referred to as the "head" and can be either a polar nonionic (uncharged), cationic (positively charged), anionic (negatively charged), or zwitterionic (having both positive and negative charge with net zero charge) group. When added to water, surfactants dissolve and form a solution of monomers. At a certain concentration called the critical micelle concentration (CMC), surfactants begin to attractively interact with each other. At this point it becomes energetically favorable to grow micelles, or n-mers. Thus, as more surfactants are added above the CMC, the concentration of monomers is approximately fixed while the concentration of n-mers increases. It is above the CMC when bulk fluid properties, such as viscosity, conductivity, and specific heat capacity will begin to change significantly. Below the CMC, these properties are relatively unchanged from that of the pure

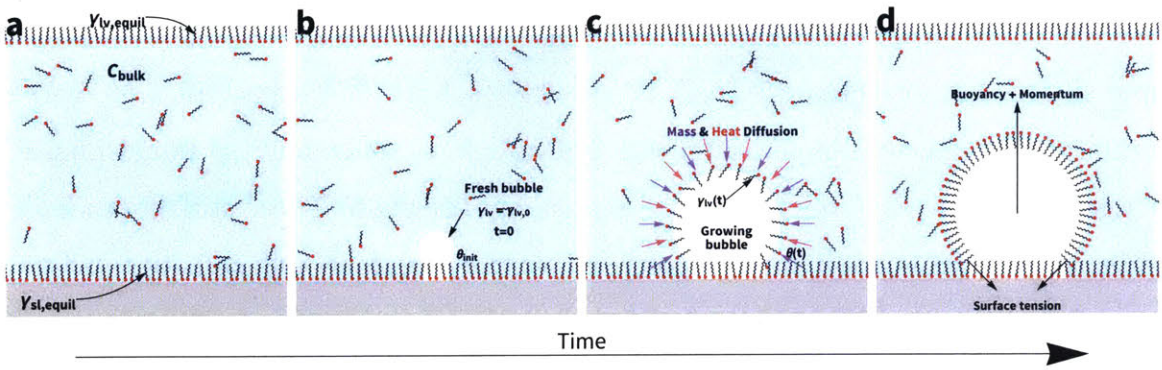

Figure 1-7: **Schematic diagram of surfactant behavior around a growing bubble.** (a) Before nucleation, liquid-vapor and solid-liquid interfaces are equilibrated. (b) At the onset of nucleation, a fresh bubble will have no surfactants at the liquid-vapor interface. (c) As the bubble grows, surfactants diffuse to the liquid- vapor interface. (d) At longer timescales, the liquid-vapor interface will be nearly equilibrated as buoyancy and momentum forces become important.

solvent [41, 43]. However, interfacial energy will change significantly since adsorption primarily happens below the CMC. The adsorption of surfactants to an interface lowers the interfacial energy. Because of the importance of interfacial properties for wetting, most surfactant studies in boiling have focused on submicellar (below CMC) concentrations. CMCs can range orders of magnitude from nM to tens of mM and this is largely due to the relative hydrophobicity of the tail, with more hydrophobic tails (such as longer tails) yielding lower CMCs.

Now, let us examine how surfactants behave in the context of a surfactant boiling system at submicellar concentration, where solid-liquid and liquid-vapor adsorption are important [44]. Surfactants placed in a bulk fluid will eventually have a portion adsorbed to the liquid-vapor and solid-liquid interfaces after some time has elapsed for equilibration (Figure 1-7a). The equilibration process involves diffusion of surfactants from the bulk up to the interface, and a chemical change from a solvated state to an interfacial state. Since equilibration takes time, the interfacial energy in the presence of surfactants is a function of time, i.e., dynamic surface tension [45]. When heat is applied and boiling commences, a newly formed bubble will have a fresh liquid-vapor interface without any surfactants present since inadequate time has elapsed to equilibrate the interface (Figure 1-7b). As the bubble grows over

time, surfactants will have diffused to the liquid-vapor interface, lowering the liquid-vapor surface tension (Figure 1-7c,d). Meanwhile, some of the surfactants that were equilibrated at the solid-liquid interface will now have its contacting liquid phase changed to vapor since the bubble has expanded over them. These surfactants underneath the bubble, now sitting at the solid-vapor interface, will remain fixed to the surface [46]. That is, the surface concentration of surfactants [$\mathrm{mol\,m^{-2}}$] under the bubble is the same as that of solid-liquid equilibrium (surfactants at the solid-vapor interface should not immediately evaporate away given their very low vapor pressures). On the other hand, liquid-vapor surface tension should be a function of bubble lifetime. This leads to bubble nucleation, growth, and departure behavior that is highly dependent on growth rate and superheat, adding a significant layer of complexity over bubble behavior with pure fluids.

While it is clear that both solid-liquid and liquid-vapor effects play a role, the relative importance of the two types of adsorption, among other effects, has not been clearly determined in the existing literature. Studies have shown that adding surfactant below the CMC can shift the boiling curve left and increase HTC (Figure 1-8), which suggets that solid-liquid adsorption causing the surface to become increasing hydrophobic can lead to enhanced nucleation. On the other hand, dynamic surface tension measurements of surfactant solutions showing a drop in liquid-vapor surface tension would suggest that earlier bubble departure would increase heat transfer performance [47, 48, 44, 49]. In fact, most studies tend to attribute enhancement behavior *primarily* to liquid-vapor surface tension changes among numerous other effects [47, 50, 44]. Convective flows around bubbles especially in the vicinity of the thermal boundary layer can be important to heat transfer [51]. These effects affect overall convective heat transfer, but also diffusion of surfactants. Furthermore, the presence of a thermal boundary layer can induce Marangoni flows, which can alter surfactant diffusion as well as surface tension effects [50, 52]. Thus, while many possible factors that affect boiling have been identified, a clear mechanistic description of the phenomenon has not emerged. There still lacks an understanding of what kinds of surfactants are ideal for boiling applications.

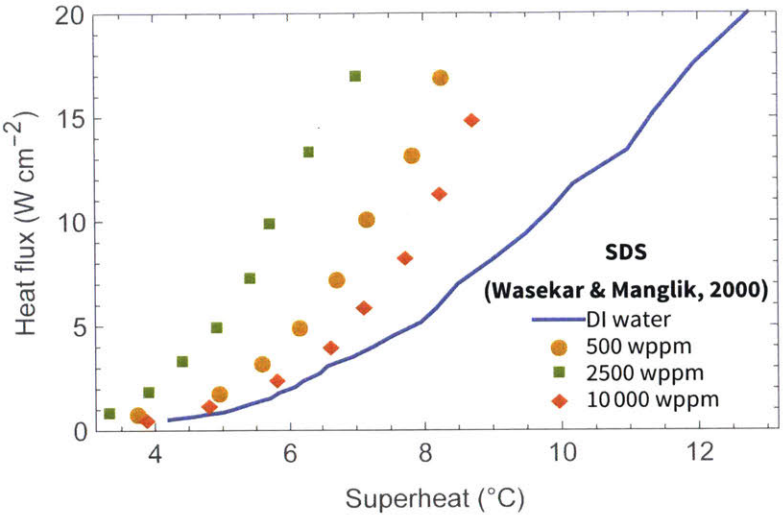

Figure 1-8: **Boiling curves for SDS at various concentrations.** The boiling curve shifts left (increasing HTC) for increasing concentration up until the CMC is reached (approximately 2500 wppm for SDS) [48].

1.3 Thesis objectives and outline

In this thesis, we will provide an understanding of how surfactants enhance boiling heat transfer from molecular and macroscopic perspectives. This micro- to macro-framework will allow us to link the relevant natural phenomena to build a mechanistic description of surfactant boiling (Figure 1-9). In this framework, molecular parameters determine wetting properties. Wetting properties, in turn, affect bubble behavior. Finally, bubble behavior will affect heat transfer. From this framework, we will show that solid-liquid adsorption of surfactants (not liquid-vapor adsorption contrary to previous literature) is *primarily* responsible for heat transfer enhancement. Ultimately, this framework will allow us to see how pool boiling performance can change based on variation of a molecular parameter (such as length of tail), which could help one identify which types of surfactants would be ideal for a particular boiling application. We will show that, in most cases, low-CMC surfactants are desirable.

This work is focused on pool boiling of water with surfactants that come from three homologous, alkyl-terminated families: the nonionic methylglucamine surfactants (commonly known as MEGA-n with n being the number of carbons in the tail),

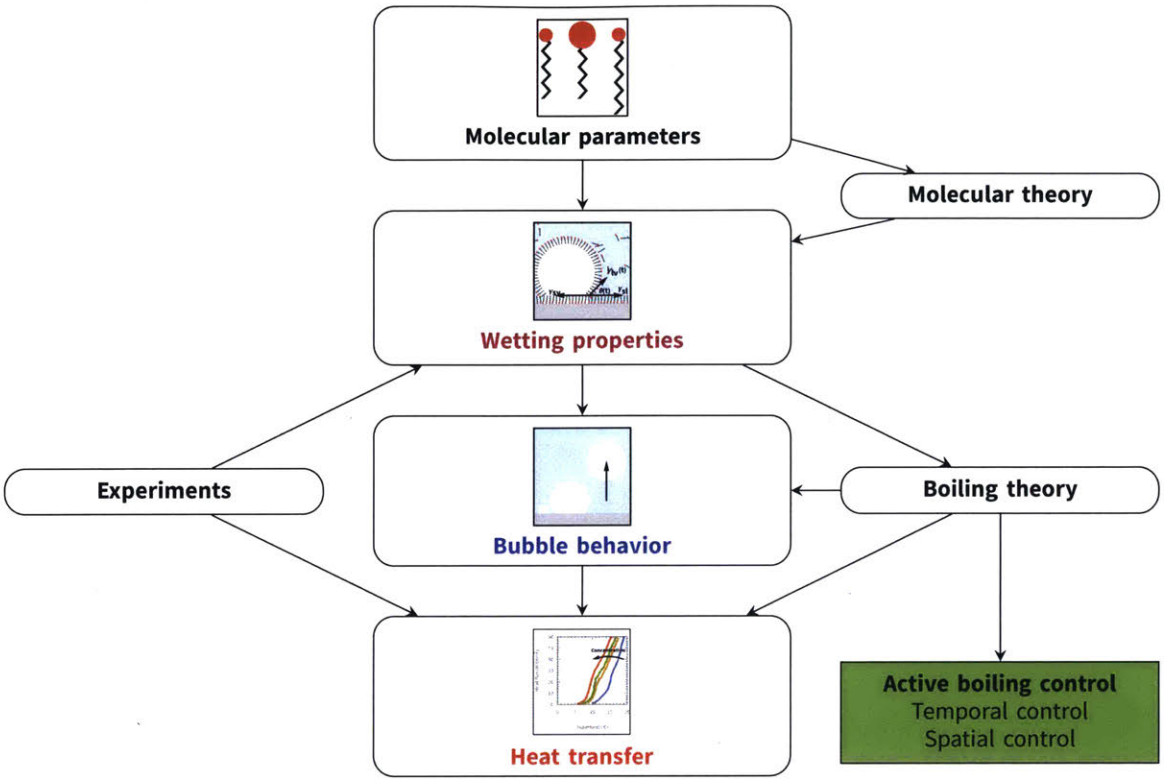

Figure 1-9: **Framework of thesis.** Experiments will measure wetting properties and boiling performance (Chapter 2). Molecular theory will be used to predict wetting properties from molecular parameter (Chapter 3). Boiling theory will be used to connect wetting properties to bubble nucleation, growth, and departure, which will subsequently be used to predict heat-transfer enhancement (Chapter 4). Knowledge gained from developing boiling theory will be used to demonstrate active boiling control with electric fields and surfactants (Chapter 5).

the anionic sodium sulfates (will be referred to as SnS) and the cationic trimethylammonium bromides (nTAB). This is an experimental and theoretical study. Recognizing the importance of adsorption, we have performed experiments to measure liquid-vapor surface tension and contact angle. In addition, numerous boiling experiments have also been performed with the aforementioned surfactant families. These experimental results have guided the development of a theoretical modeling framework to understand surfactant adsorption, diffusion, bubble behavior, and ultimately heat transfer.

We will begin in Chapter 2 where details of the experimental techniques for dynamic and equilibrium surface tension, contact angle, and pool boiling will be discussed. In Chapter 3, we will introduce a model based on statistical mechanics

that can predict the equilibrium surface tension of surfactant solutions as well as a model to determine dynamic surface tension. In Chapter 4, we will discuss a model that describes bubble nucleation, growth, and departure, which, when combined with the surface tension description in Chapter 2, provides the ability to predict boiling curves based on molecular parameters. In Chapter 5, we demonstrate a novel capability of active control of boiling using electric fields, which leverages work from previous Chapters. Finally, in Chapter 6, we summarize our work, discuss future directions that can be made from this work, and comment on the impact of having gained a more complete understanding of surfactant boiling.

CHAPTER 2

EXPERIMENTAL TECHNIQUES

To validate pool boiling heat transfer and wetting properties predicted by modeling, a variety of experiments were performed. Pool boiling curves, static and dynamic liquid-vapor surface tension, as well as contact angles were obtained as they vary with of surfactant type, concentration, and temperature. Temperature, in particular, is a parameter that has seldom been investigated in existing literature with regard to wetting properties but is especially relevant in heat-transfer applications. For heat-transfer measurements, decades of pool boiling experiments have led to established methods for pool boiling experiments, which this current study has adopted. On the other hand with wetting property measurements, while there are various methods to measure surface tension and contact angle, results have been shown to be sensitive to time-dependent effects, contamination, and other non-idealities [53, 54]. Thus, certain modifications and innovations have been made to account for these effects and will be discussed.

Two main experimental setups have been used in this study. Pool boiling experiments were performed on a custom testing rig, the **boiling chamber**, designed to hold approximately 500 mL of fluid. Surface tension and contact angle measurements were performed on a smaller testing rig, the **mini chamber**, designed to hold

approximately 150 mL of fluid.

2.1 Surfactant preparation

Surfactants of methylglucamine (MEGA), sodium sulfate (SS), and trimethylammonium bromide (TAB) families were purchased from Sigma-Aldrich or Alfa Aesar. With the exception of S14S (95 % purity with up to 5 % sodium methyl sulfate), surfactants purchased were of $\geq$ 98 % purity. If liquid solutions were not readily available for purchase, then powder forms were purchased and dissolved at appropriate concentrations in deionized (DI) water to create "source" solutions. During experiments, the "sample" solution, initially pure DI water, would have small quantities of source solution added so as to obtain different sample solution concentrations. Ideally, source solution concentrations were sufficiently high enough that the overall volume of the sample solution did not change much, but sufficiently large enough that volume additions of source solution were not impractically small ($< 5\mu$L). Furthermore, solubility limited the maximum concentration attainable for source solutions. Suitable source concentrations were determined and are shown in Table 2.1. Source solutions were prepared in centrifuge tubes with volumes of 40 mL. Before testing, source solutions were sonicated at 40 °C for up to several hours to ensure more complete dissolution since solutions left at room temperature were observed to phase separate over time.

2.2 Pool boiling experiments

The boiling chamber used for pool boiling experiments (Figure 2-1) was relatively unchanged from that used by Chu et al. [26, 20], and further details can also be found in Chu's thesis [58]. For most experiments, metal foils were used as boiling surface samples and were soldered to the top of copper heating block using Sn-Pb solder paste (Delta 717D, Qualitek). The copper block could be heated from the bottom by five cartridge heaters. These cartridge heaters, electrically connected

Table 2.1: Surfactants used in this study.

	Short name	Charge (e)	Tail length	Mol. weight (u)	CMC @ 25 °C (mM)	CMC @ 100 °C (mM)	Source conc. (mM)
MEGA	MEGA-8	0	8	321.41	70[55]	N/A	389
	MEGA-10	0	10	349.46	4.7[56]	4.0[a]	57.8
SS	S10S	-1	10	260.33	32[b]	38[b]	528
	S12S	-1	12	288.38	7.4[b]	10[b]	173
	S14S	-1	14	316.44	1.8[b]	3.0[b]	17
TAB	10TAB	+1	10	280.29	45[b]	53[b]	714
	12TAB	+1	12	308.34	10[b]	14[b]	173
	14TAB	+1	14	336.39	2.4[b]	4.0[b]	173
	16TAB	+1	16	364.45	0.56[b]	1.1[b]	35

[a] Determined by extrapolating data from Sulthana et al. [56]
[b] Determined by PREDICT software developed by Zoeller and Blankschtein [57].

in series, were powered by a programmable high power supply (KLP-600-4, Kepco) controlled by a LabView® program. The top section of the copper block has a narrow 2 cm × 2 cm square cross-sectional profile and is insulated by Teflon® in order to provide 1-D heat conduction from bottom to top. A glass enclosure with square cross-sectional profile (BST-60-300, Friedrich & Dimmock) was placed on top of the foil and sealed by a silicone gasket. The top of the glass enclosure was fitted with a PEEK covering with port holes made from push-to-connect fittings as well as an opening for a coil reflux condenser (QC-6-4, Quark glass). The condenser was open to atmosphere to maintain system pressure at 1 atm. The fluid side of the condenser was connected to a chiller (RTE-111, Neslab) so chilled water could circulate through the condenser and condense vapor, preventing any mass loss and concentration change. A rope heater wrapped around the glass enclosure and was powered by a Variac to prevent heat loss through the glass, which helped maintain saturation conditions.

Metal foil samples were either gold-coated copper foils, or silver foils. Gold-coated copper foils were fabricated by taking 25 μm-thick, alloy-110 copper (99.9 % Cu) sheets (purchased from Basic Copper) and electroplating 0.5 μm of gold (performed by TDF Metal Finishing) on top of them. Silver foils were 51 μm thick with 99 % purity (purchased from American Elements) and were roughened with 240 grit (CAMI standard) sandpaper for nucleation enhancement.

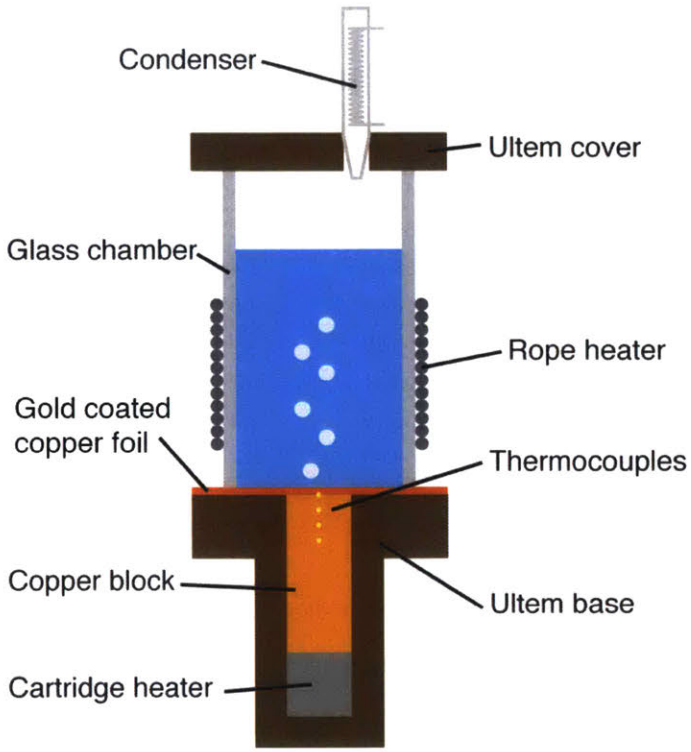

Figure 2-1: **Schematic diagram of boiling chamber.**

To calculate heat flux and measure temperature, four thermocouples spaced 8 mm apart in the constant cross-sectional-area section of the copper block just beneath the foil were used. The topmost thermocouple provided the surface temperature measurement while the other thermocouples provided information to calculate the heat flux. Due to the existence of heat losses (imperfect 1-D conduction), the following fin equation was solved and used to fit the thermocouple data to determine the heat flux at the surface.

$$0 = \frac{\partial^2 T(x)}{\partial x^2} - \frac{h_{cb} P_{cb}}{k_{cb} A_{cb}} (T(x) - T_\infty) \tag{2.1}$$

Here, h_{cb} is the heat transfer coefficient from the copper block to the ambient, P_{cb} is the perimeter of the block cross-sectional profile, k_{cb} is the thermal conductivity of copper, and A_{cb} is the cross-sectional area of the block. The fin equation is valid in this case since the Biot number was calculated to be 0.003. The boundary conditions used were $(\partial T/\partial x)_{x=L} = q''_L/k_{cb}$ and $T(x = 0) = T_{wall}$. An arbitrary value of L

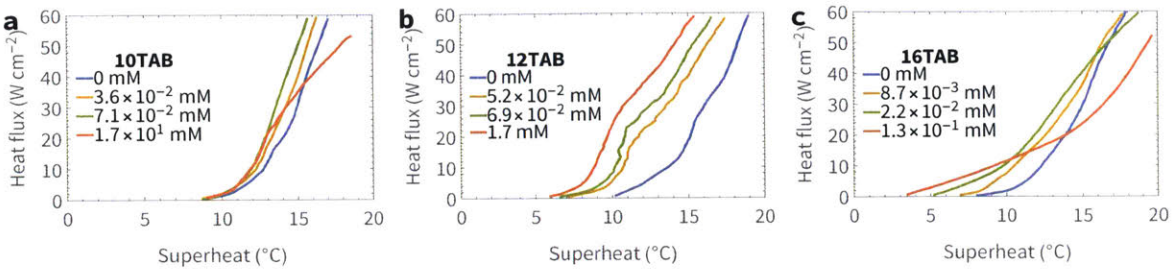

Figure 2-2: **Boiling curves for TAB surfactants.** Boiling curves for (a) 10TAB, (b) 12TAB, and (c) 16TAB at various concentrations.

was applied while q''_L and h_{cb} were used as fitting parameters. The aribtrary L is appropriate since non-dimensionalizing the problem shows that $q''_L L$ together is an unknown quantity. Thus, choosing an L and fitting a q''_L is the same as fitting the quantity $q''_L L$.

Images and movies were taken using a either high-speed (Phantom V7, Vision Research) or a machine-vision (CM3-U3-13Y3C, Point Grey) camera. These were fitted with either a zoom (EF 28-135mm f/3.5-5.6 IS USM, Canon) or macro (MP-E 65mm f/2.8 1-5x Macro Photo, Canon) lens.

Boiling curves were obtained by heating the liquid to a certain power (usually when the heat flux was approximately $60\,\mathrm{W\,cm^{-2}}$) and removing power from the heaters, allowing the surface to cool down from a superheated condition; hence, descending boiling curves were obtained. The cooling rate (approximately $1\,^{\circ}\mathrm{C\,min^{-1}}$ to $2\,^{\circ}\mathrm{C\,min^{-1}}$) was sufficiently slow since boiling curves obtained using slower cooling rates were identical.

Approximately fifteen to twenty concentrations were run for each surfactant. Full boiling curve data can be found in Appendix A.1. With increasing concentration, boiling curves shifted left as expected as shown in Figure 2-2 and this was correlated with an increase in nucleation. Surfactants with lower CMCs (longer tail lengths) shifted more left than higher CMC surfactants. However, the slopes of the boiling curves tended to decrease with lower CMC surfactants. These effects will be explained more in detail in Chapter 4.

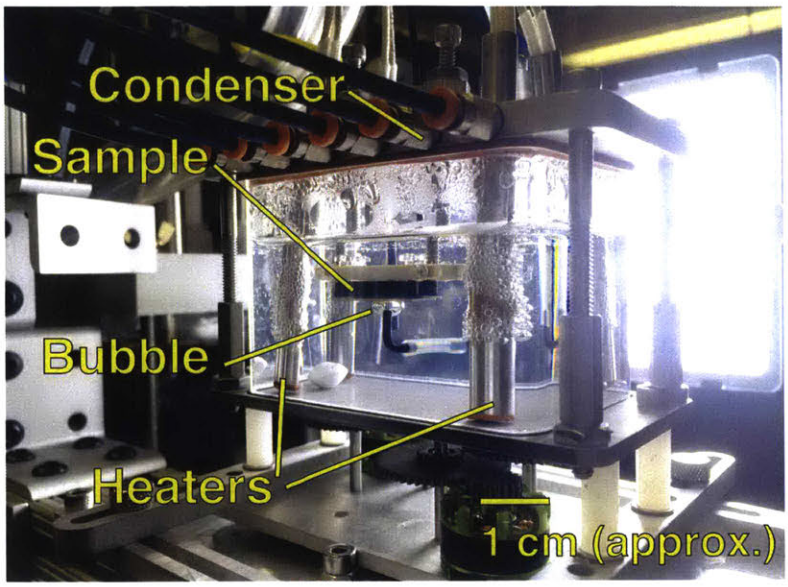

Figure 2-3: **Photograph of the mini chamber.**

2.3 Mini chamber experiments

Wetting property measurements were performed in a mini chamber designed to hold approximately 150 mL of fluid. The mini chamber was custom fabricated in order to facilitate temperature control (by heating the liquid) and preventing mass loss from evaporation by incorporation of a condenser top.

2.3.1 Mini chamber

The mini chamber consisted of liquid rectangular glass tube (BRT-50-75-250, Friedrich & Dimmock) sandwiched between a stainless steel bottom plate and an aluminum top plate (Figure 2-3). The stainless steel plate provided thermal insulation and relatively low magnetic permeability in order to allow rotating magnets below to drive a magnetic stir bars inside the chamber. The aluminum top plate served as a condenser to prevent mass loss. It was thermally conductive and had holes drilled laterally for cooling water flow. COMSOL modeling was performed to ensure that adequate liquid cooling could be provided to condense all evaporating liquid at 100 °C.

Port holes using compression tube fittings were incorporated at the top to allow for thermocouple and sample mounting fixtures to be inserted. Heat was provided

by four 6.35 mm diameter cartridge heaters sheathed by PFA-coated stainless steel tubes (PFA coating performed by American Durafilm). The PFA served to prevent oxidation of the heater sheaths. The heaters were powered by either a programmable high power supply (KLP-600-4, Kepco) controlled by a LabView program or a custom power supply (chamber controller in Figure 2-6) controlled by an Arduino® Uno board.

2.3.2 Equilibrium surface tension measurements

Equilibrium surface tension measurements were performed using the pendant bubble method inside the mini chamber. Though pendant droplet methods are more common [59], the pendant bubble method was chosen since the temperature of the liquid surrounding a bubble could be better controlled by heating the liquid inside the mini chamber rather than trying to heat the vapor around a pendant droplet.

A vertical tube with 1.3 mm ID, with its opening facing upwards provided a source of bubbles and was placed into the mini chamber. The tube could be selectively connected to either a nitrogen gas or vacuum source with flow rates modified by needle valves. This way, the bubble growth rate and direction could be controlled. Growth rate was set to be as slow as practically possible in order to obtain quasi-static behavior ($< 1 \mu \mathrm{L\,s}^{-1}$). Horizontal profile images of the pendant bubble were taken for analysis (Figure 2-4a). The profile images were then processed using a custom image processing algorithm. Measurements were most accurate when the bubble was close to departure from the tube.

The algorithm (written with the ITK library in C++) first binarized the image so dark regions were incorporated into the bubble region. Then, the image was filtered such that any remaining bright spots within the bubble were removed. Next, the profile of the bubble was found (edge detection) by applying a gradient filter on the image and subsequently binarizing the result. The profile points were then imported into a Mathematica® script which curve-fit the solution to the Young-Laplace equation (Figure 2-4b,c). For a pendant bubble/droplet, the following differen-

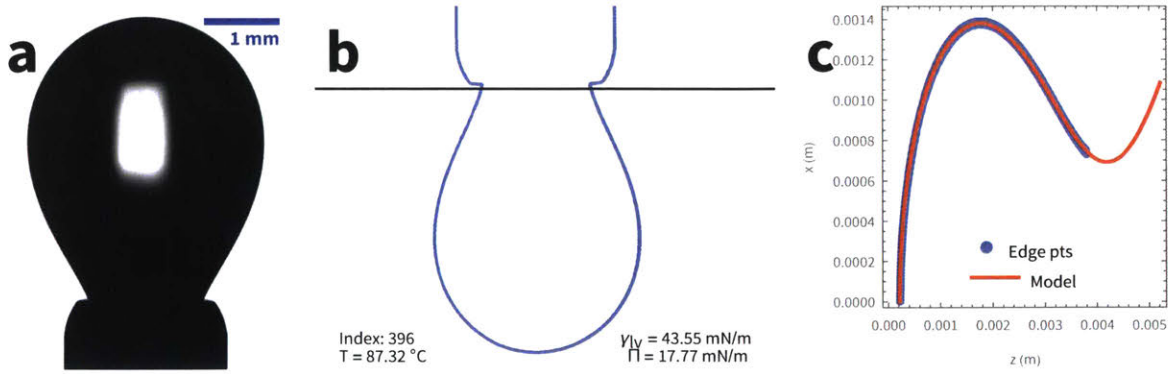

Figure 2-4: **Image processing of a pendant bubble.** (a) A photograph of the pendant bubble profile is taken. (b) The edge points are found using an image processing algorithm. (c) The numerical solution to the Young-Laplace equation is fit to the edge points showing very good agreement.

tial equations (Young-Laplace equation for a vertically axisymmetric bubble/droplet with gravity in the vertical direction) describe the shape of the profile:

$$\frac{d\Theta}{ds} = 2 - \beta z - \frac{\sin\Theta}{x}, \tag{2.2}$$

$$\frac{dx}{ds} = \cos\Theta, \tag{2.3}$$

$$\frac{dy}{ds} = \sin\Theta \tag{2.4}$$

where x is the horizontal axis, z is the vertical axis, s is the axis along the profile, Θ is the tangent angle along the profile, β is a nondimensional shape factor ($\beta = \frac{(\rho_l - \rho_v)gR_0^2}{\gamma_{lv}}$), and R_0 is the radius of curvature at the base [60]. Since there is no analytical solution to these equations, numerical fitting, where γ_{lv} is the unknown parameter, was performed in the Mathematica code. The typical goodness-of-fit for the Young-Laplace solution to the profile was $R^2 > 0.999$. The accuracy of this technique was validated for water at various temperatures and was found to be accurate within $\pm$ 2 %.

Approximately fifteen submicellar concentrations were tested for each surfactant at temperatures ranging from 70 °C to 90 °C in most tests. In all cases, surface tension decreased with increasing concentration as expected. Surface pressure, Π, was also

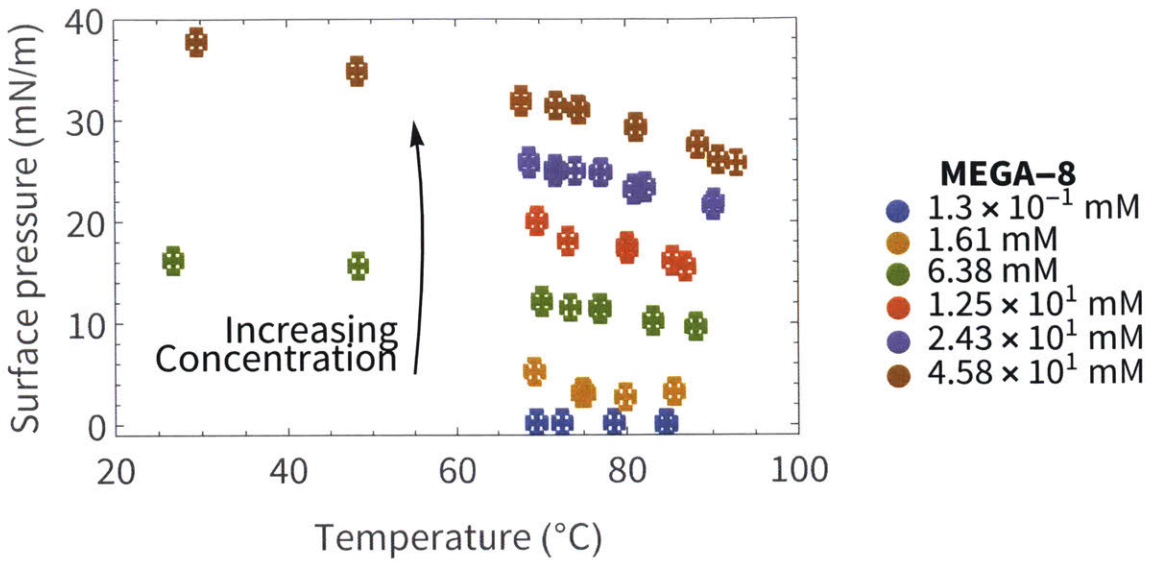

Figure 2-5: **Surface pressure of MEGA-8 solution at various concentrations and temperatures.**

calculated and is defined as

$$\Pi = \gamma_{lv,0} - \gamma_{lv} \tag{2.5}$$

where $\gamma_{lv,0}$ is the surface tension for pure water. Surface pressure was also found to decrease slightly with increasing temperature in all cases (representative data shown in Figure 2-5). More data can be found in Appendix A.2.

2.3.3 Dynamic surface tension measurements

Dynamic surface tension measurements were performed using the maximum bubble pressure (MBP) method [61] on a Sinterface BPA-1S owned by Unilever in Trumbull, CT as shown in Figure 2-6. The MBP method involves placing a capillary tube inside water, flowing air through the tube, and monitoring the pressure inside the tube. The vapor phase will expand through the tube and become pinned at the opening. From this pinned state, the tangential angle of the liquid-vapor interface (measured from the liquid side) to the inner tube wall decreases. Once it is at 0° (hemispherical bubble), the bubble pressure is at a maximum and the radius of curvature is equivalent to the inner radius of the tube; thus, the liquid-vapor surface

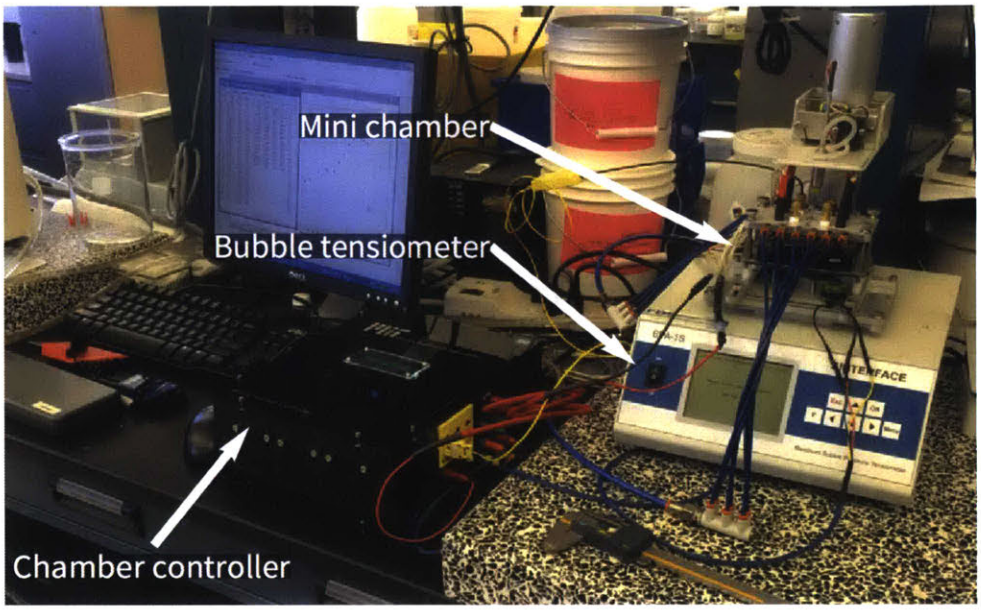

Figure 2-6: **Photograph of the dynamic surface tension measurement setup.**

tension can be measured using the Young-Laplace equation. By modifying the flow rate of gas, different bubble lifetimes emerge, allowing for the measurement of surface tension as a function of bubble (or liquid-vapor interface) lifetime.

Normally, the capillary tube is placed within the fluid inside an open beaker. However, since measurements at elevated temperatures were made (up to 70 °C), the mini chamber with a condenser top was used to prevent mass loss and concentration change. Surfactants were tested at three to five concentrations at temperatures of 30 °C, 50 °C, and 70 °C. Example data of 16TAB is shown in Figure 2-7. Full dynamic surface tension data can be found in Appendix A.3. As expected, equilibration of surface tension occurred faster with increasing concentration.

2.3.4 Contact angle measurements

Advancing and receding contact angles were measured on a gold sample. The gold sample was fabricated by electron beam physical vapor deposition of approximately 300 nm-thick gold on a quartz wafer and then cutting by dicing saw. The samples were placed inverted inside the mini chamber with the same tube for equilibrium surface tension measurements used to supply a bubble for contact angle measure-

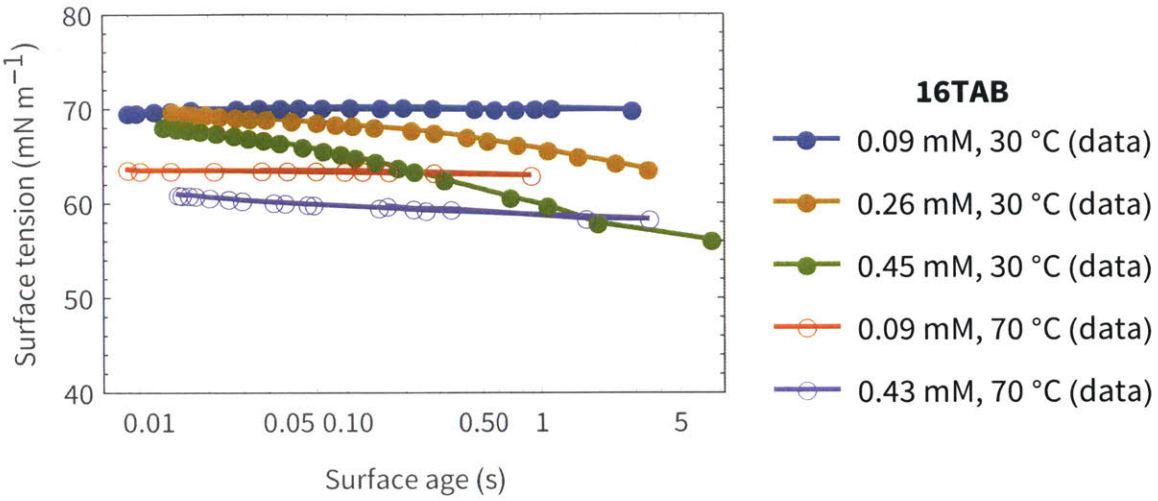

Figure 2-7: **Dynamic surface tension of 16TAB at different temperatures.**

ment. Bubble growth and shrinkage rates were set to be as slow as possible to obtain quasi-static advancing and receding contact angles. Contact angles were measured with the same edge detection algorithm developed for equilibrium surface tension measurements, and subsequently fitting edge pixels near the contact plane to circular profiles as shown in Figure 2-8. Left and right sides were measured independently and incorporated into the uncertainty. The typical goodness-of-fit for circular profiles was $R^2 > 0.998$. The typical uncertainty in contact angle measurement was $\pm$ 1°.

Due to hydrocarbon adsorption, gold exposed to air appears hydrophobic whereas gold that is free of contaminants has a 0° contact angle [62]. However, performing contact angle measurements in a contaminant free environment is challenging. In boiling, constant formation of water vapor bubbles at elevated temperatures could conceivably lead to evaporation and partial cleaning of the surface. In order to more closely replicate this partially cleaned state, the following *in situ* sample cleaning method was devised.

First, the sample in the mini chamber was submerged completely in DI water so that no air pathways to the sample surface existed. Then, purified nitrogen gas bubbles with low hydrocarbon concentration were flowed over the sample. After that, a detergent surfactant, such as S12S, was added to the chamber so as to bring the

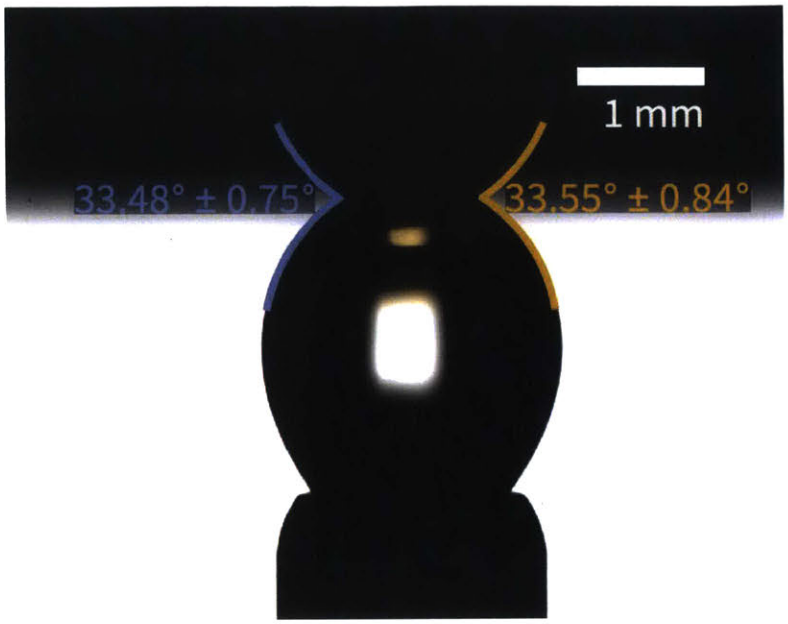

Figure 2-8: **Contact angle measurement of a bubble in pure water in contact with gold.** Contact angle was measured by fitting intersecting circular arcs to the liquid-vapor edge points near three-phase contact line.

concentration approximately five times higher than the CMC. While continuously bubbling nitrogen over the surface, the chamber was then heated to approximately 90 °C for effective detergency. The mechanism of cleaning is believed to be surfactant micelles capturing hydrocarbon contaminants on the surface (detergency effect) with the bubbling flow of nitrogen aiding in convective mass transfer. After heated cleaning for several hours, the chamber was rinsed several times to remove surfactants from the chamber. During rinsing, a relatively large flow rate of nitrogen was applied so as to maintain positive pressure in the chamber and prevent air from entering and contaminating the sample. Finally, 120 mL of DI water was added for the experiment. By employing the above cleaning method, contact angles in gold were approximately 3° for receding and 30° for advancing contact angles. When gold was exposed to air, the advancing and receding contact angles were closer to 90° and 65°, respectively, as shown in Figure 2-9.

Contact angle measurements were performed simultaneously with equilibrium surface tension measurements and approximately fifteen submicellar concentrations were tested for each surfactant at temperatures ranging from 70 °C to 90 °C. Remark-

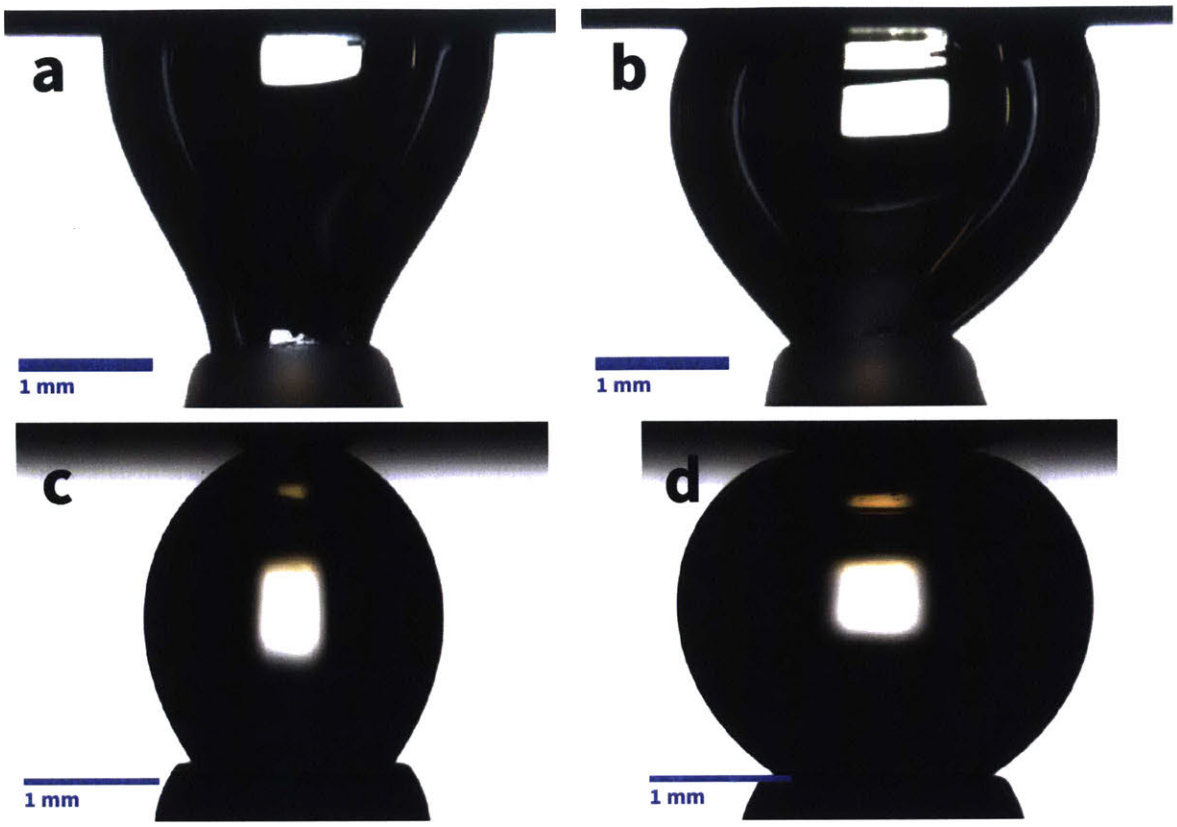

Figure 2-9: **Advancing and receding contact angles with and without cleaning.** Without any cleaning and exposure to air, gold showed an (a) advancing contact angle of approximately 90° and (b) a receding contact angle of approximately 65°. After *in situ* cleaning, the (c) advancing contact angle was approximately 30° while the (d) receding contact angle was approximately 3°.

ably, receding contact angles were found to stay approximately constant at all concentrations (Appendix A.2). Advancing contact angles were observed to approach the receding value with increasing concentration, thereby lowering contact angle hysteresis. If the receding contact angle is taken to be closer to the true intrinsic contact angle of the surface,[1] then some analysis can be made regarding the actual intrinsic contact angle of the surface. If the contact angle is approximately constant with concentration, i.e.

$$\theta = \arccos\left(\frac{\gamma_{sv} - \gamma_{sl}}{\gamma_{lv}}\right) \approx \text{constant}, \tag{2.6}$$

[1]If the surface is assumed to be heterogeneous, comprising of hydrophilic gold and a less hydrophilic contaminant, then the receding contact angle should be closer to that of the intrinsic contact angle of gold (see Carey's explanation [16]).

then it implies that

$$\gamma_{lv} \propto \gamma_{sv} - \gamma_{sl}. \tag{2.7}$$

In other words, liquid-vapor adsorption is approximately proportional to solid-liquid adsorption, which is reasonable given that adsorption mechanics should be highly dictated by the surfactant itself as will be discussed in Chapter 3. The effect of solid-liquid adsorption, then, is to make the surface more hydrophobic. This is apparent when we calculate what the "initial" contact angle on this surfactant-coated surface would be if we placed a bubble free of any surfactants at the liquid-vapor interface on top of it. We call this the initial contact angle because this would be the contact angle of a bubble in the limit that the interface lifetime is zero ($t = 0$) when no surfactants have diffused to the liquid-vapor interface. Initial contact angle data can also be found in Appendix A.2. Here,

$$\theta_{init} = \arccos\left(\frac{\gamma_{sv} - \gamma_{sl}}{\gamma_{lv,0}}\right). \tag{2.8}$$

As shown in Figure 2-10, it is apparent that the surface becomes more hydrophobic as concentration increases, and this has significant implications to nucleation behavior as will be discussed in Chapter 4.

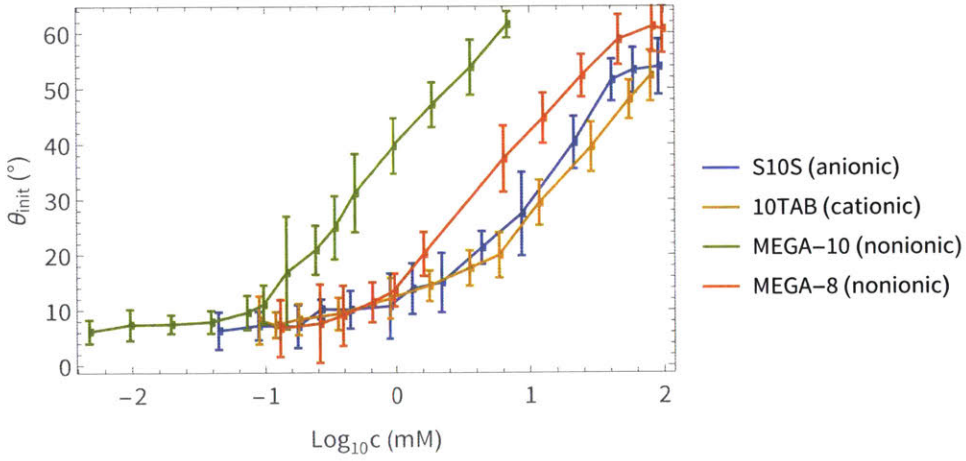

Figure 2-10: **Initial contact angle as a function of concentration for various surfactants.** MEGA-8, MEGA-10, S10S, and 10TAB all exhibit an increase in initial contact angle (contact angle solely due to solid-liquid adsorption and not liquid-vapor adsorption; based on receding contact angle) as concentration increases.

2.4 Summary

In this Chapter, we first described surfactants used in this study as well as how they were prepared. Then, we discussed pool boiling experiments and methodology. After that, we described the mini chamber which was used to perform liquid-vapor surface tension measurements (equilibrium and dynamic) and contact angle measurements. Surface tension measurements performed at various temperatures and concentrations, in conjunction with literature data, is used to validate the wetting property prediction models described in Chapter 3. From contact angle measurements, we found that θ is approximately a constant with concentration, which is an approximation we will use to relate liquid-vapor adsorption to solid-liquid adsorption in Chapter 4.

CHAPTER 3

PREDICTION OF SURFACE TENSION WITH SURFACTANTS

Surface tension change is the defining aspect of surfactants and is especially important to boiling performance as it dictates bubble nucleation, growth, and departure. In this chapter, we will first detail a model to predict equilibrium liquid-vapor surface tension using molecular thermodynamics, and then we will incorporate this model into a dynamic surface tension model. As discussed in Section 2.3.4, understanding liquid-vapor surface tension can also reveal behavior about solid-liquid adsorption. Thus, the findings presented here will provide the necessary information to model bubble behavior from molecular parameters, and ultimately heat transfer in Chapter 4. For a background on some of the thermodynamic concepts described in this Chapter please see Appendix B.

3.1 Previous modeling approaches

One of the earliest endeavors in understanding surface tension came from Gibbs and is often the point of departure for interpreting surface tension measurements [63].

The Gibbs isotherm states that

$$-d\gamma_i = d\Pi_i = \Gamma_i d\mu_i \tag{3.1}$$

where, for some species i, γ_i is its contribution to surface tension, Π_i is its contribution to surface pressure, Γ_i is its excess (total adsorption or surface concentration [$\mathrm{mol\,m^{-2}}$]), and μ_i is its chemical potential. Then, by using the generic chemical potential formula

$$\mu_i = \mu_i^{\circ} + kT \ln a_i \tag{3.2}$$

where μ_i° is the standard state chemical potential, k is the Boltzmann constant, and a_i is the chemical activity,

$$\Gamma_i = -\frac{1}{kT}\frac{d\gamma_i}{d\ln a_i}. \tag{3.3}$$

Therefore, surface adsorption can be extracted based on the slope of a surface tension isotherm (surface tension as a function of concentration). Though Eq. 3.3 does not get into specifics of molecular behavior, it provides a basis for the the important variables at play: surface adsorption, surface tension, concentration, and activity coefficient.[1]

A more detailed physical picture of the liquid-vapor interface where the monolayer has finite thickness is shown in Figure 3-1. For ionic surfactants, an electric double layer (EDL) forms due to the high concentration of charge at the monolayer. The diffuse electric double layer is modeled according to the Poisson-Boltzmann equation (Gouy-Chapman theory [64, 65]). By taking into account the finite size of ionic particles, a gap with thickness δ_{gap} can be expected between the diffuse layer and the monolayer (Stern layer [66]).

By incorporating effects of the EDL, Davies came up with a simple adsorption isotherm (relationship between surface concentration [$\mathrm{mol\,m^{-2}}$] and bulk concentration [$\mathrm{mol\,m^{-3}}$]) [67]. Combined with an equation of state (relationship between surface pressure [$\mathrm{N\,m^{-1}}$] and surface concentration) he developed earlier that as-

[1]Activity coefficient, f_i, where $a_i = f_i \frac{c_i}{c_i^{\circ}}$, is a factor that describes how ideal (non-interacting) a species is. When it is ideal, it is equal to unity.

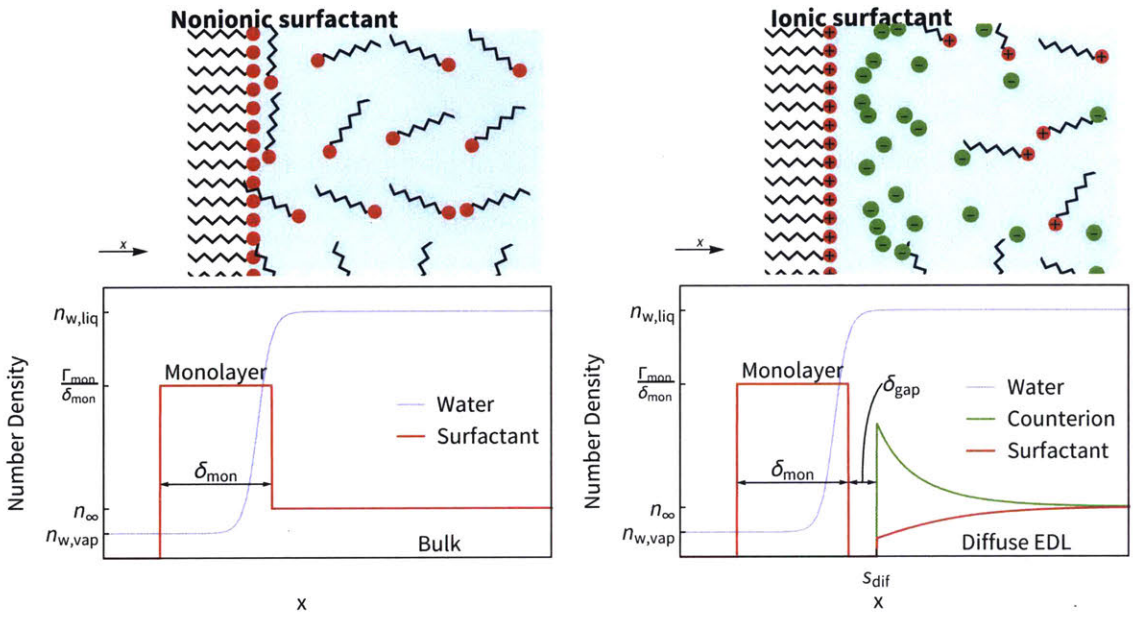

Figure 3-1: **Illustration of the surfactant monolayer.** (a) Nonionic and (b) ionic surfactant monolayers at the liquid-vapor interface in equilibrium with nearby solvated surfactants. Number densities of water, surfactants, and counterions (for ionic surfactants) are plotted. The x axis is normal to the interface.

sumes the monolayer behaves like a 2D gas [68], a simple surface tension isotherm can be derived. However, Davies' approach assumes ideal, dilute solution behavior even at the interface (activity coefficient is unity), and does not consider interparticle interactions outside of the electric field. Lucassen-Reynders [69] utilized an activity based chemical potential model developed by Butler [70] to obtain a more realistic surface tension isotherm. However, this approach assumes electroneutrality at the interface and ignores the double layer contribution as other have noted [71, 72]. Borwankar and Wasan accounted for the EDL contribution by assigning separate adsorptions to the EDL and a Gibbs dividing surface in their approach of obtaining a surface tension isotherm [71]. Kralchevsky et al. further considered the effects of counterion binding, i.e. counterions slightly disrupting the monolayer, in their approach [72]. In all of the above approaches, however, very few molecular parameters can be explicitly set as a result of a reliance on unspecified activity coefficients, which highly depend on intermolecular forces. Thus, while these models can offer useful analysis of experimental data, the ability to predict surface tension

of an arbitrary surfactant is limited.

Work by Nikas et al. [73], and Mulqueen et al. [74, 75] have taken a different approach. Rather than rely on generic isotherms or chemical potential descriptions, the chemical potential was derived from an equation of state that took into account intermolecular interactions defined by molecular properties. The equation of state is based on a ball-and-stick model, where heads are assumed to be hard sphere "balls" and tails are "sticks" attracted to each other due to van der Waals (vdW) forces. Using the Gibbs adsorption description, they were able to obtain adsorption isotherms, and surface tension isotherms as functions of molecular parameters. This provided significantly better prediction capability. However, a single fitting parameter for a given surfactant is needed since the change in standard state chemical potentials from bulk to monolayer, $\mu^{\circ}_{\text{mon}} - \mu^{\circ}_{\text{bulk}}$, is unknown.

The surface tension model described in this Chapter takes a similar approach as Nikas et al. and Mulqueen et al. However, instead of starting from an equation of state, a statistical mechanical partition function will be built. From this partition function, all thermodynamic potentials can be described as shown in Figure 3-2.

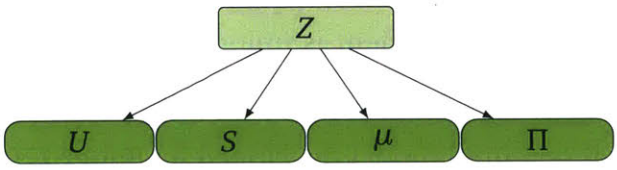

Figure 3-2: **The relationship between the partition function and thermodynamic variables.** All thermodynamic variables can be directly derived from the partition function.

From the partition function, Z, the equation of state and the adsorption isotherm can be obtained, from which the surface tension isotherm (surface tension as a function of concentration) can be determined as shown in Figure 3-3. The equation of state relates surface pressure, Π [$\mathrm{N\,m^{-1}}$], to surface adsorption (surface concentration), Γ [$\mathrm{mol\,m^{-2}}$]. The adsorption isotherm relates surface adsorption, Γ, to bulk concentration, n [$\mathrm{mol\,m^{-3}}$], and can be found by deriving the chemical potential of the monolayer from the partition function and equating it to the bulk chemical

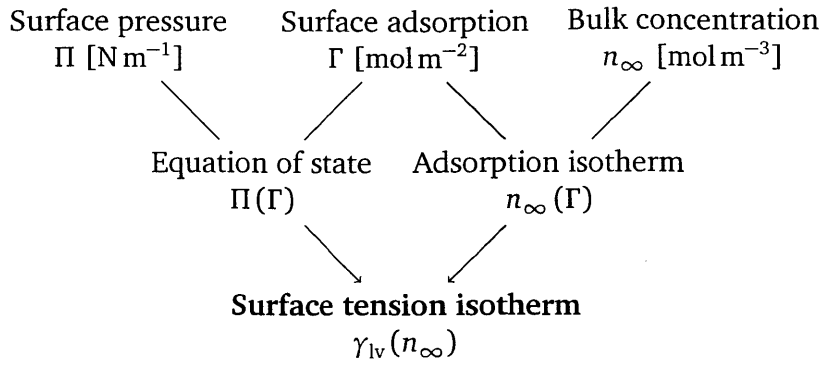

Figure 3-3: **Obtaining the surface tension isotherm from the equation of state and adsorption isotherm.** The equation of state and adsorption isotherm (green) can be derived from the partition function. The two can be combined to obtain the surface tension isotherm.

potential:

$$\mu_{\text{mon}} = \mu_{\text{bulk}}. \tag{3.4}$$

3.2 The interacting ball-and-stick description

As with numerous other statistical mechanical treatments, a simplified view of molecules and their interactions (e.g. hard sphere models) will be used for sake of clarity and mathematical convenience. That being said, even simplified views can be quite accurate, such as in the case of the van der Waals equation of state for noble gases. Like Nikas et al. and Mulqueen et al., heads are modeled as hard spheres, while tails are modeled as interacting sticks. The parameters that pertain to the head are the excluded area (equivalent to twice the cross-sectional area), a_{exc}, the charge, z, and mass. Using tails that are straight alkyl chains, the only parameter required for tails is the number of carbons, n_c, since this can determine interaction energy and mass.

The interaction between tails is determined by a model developed by Salem [76], which provides a convenient way to approximate chain interactions by integration without having to explicitly sum every interaction between chain links (CH_2 groups). Here, the interaction for two parallel molecular chains, $u(r)$ separated a distance r

apart is

$$u(r) = \frac{\chi n_c}{4\lambda r^5}\left(\frac{\lambda n_c}{r\left(\frac{\lambda^2 n_c^2}{r^2}+1\right)} + 3\arctan\left(\frac{\lambda n_c}{r}\right)\right) \tag{3.5}$$

where λ is the distance between carbon units (1.257 Å), and χ is the r^{-6} interaction energy term between two CH_2 chain units ($\chi = 9.31 \times 10^{-78}\,\mathrm{J\,m^{-6}}$). As a result, two chains have an interaction energy that scales with r^{-6} for large r and r^{-5} for small r. The mean total interaction energy felt by a single chain surrounded by other chains around it, $\overline{w}$, can be determined by the mean field approximation integral

$$\overline{w} = \int_d^\infty u(r)\frac{N}{A}2\pi r dr \tag{3.6}$$

where $\frac{N}{A}$ is the 2D number density of chains and d is the distance of closest approach before steric forces dominate ($d = 2.933$ Å, which is equivalent to the radial diameter of the chains). Integrating this yields

$$\overline{w} = \underbrace{\chi\frac{\pi n_c \arctan\left(\frac{n_c\lambda}{d}\right)}{2d^3\lambda}}_{\alpha}\underbrace{\frac{N}{A}}_{\Gamma_{mon}}. \tag{3.7}$$

Now it is apparent that all terms that constitute the interaction parameter, α, are constant; hence, $\overline{w} \propto \Gamma_{mon}$.

3.3 The electric double layer

Before delving into the statistical mechanical model, our treatment of the EDL model will be detailed since many EDL related terms will be present in the final model. Most importantly, we will derive the monolayer electric potential as a function of surface concentration.

3.3.1 Double layer model

If a monolayer surfactant species has charge, then there should be a counterion to maintain bulk electroneutrality. We expect that the surfactant should form a monolayer due to the hydrophobic effect. By forming a monolayer, however, there is now a charge distribution at the surface, which should produce an electric potential that drives counterions to form a diffuse EDL in response. Ions in solution cannot completely touch the monolayer due to size effects. Hence, there is a charged separation between counterions in solution and surfactant ions in the monolayer, δ_{gap}. We expect the potential to look like

$$\phi(x) = \begin{cases} \phi_{\text{mon}} & x = s_{\text{dif}} - \delta_{\text{gap}} \\ \phi_{\text{gap}}(x) & s_{\text{dif}} - \delta_{\text{gap}} < x < s_{\text{dif}} \\ \phi_{\text{dif}}(x) & x \geq s_{\text{dif}} \end{cases} \tag{3.8}$$

where ϕ_{mon} is the potential at the monolayer, ϕ_{gap} is the potential between the monolayer and diffuse layer, ϕ_{dif} is the potential of the diffuse layer, and s_{dif} is the point at which the diffuse layer starts (Figure 3-1).

3.3.2 Diffuse layer potential

From Boltzmann statistics, we expect that the concentration of an ideal dissolved ionic species, n_i, should be

$$n_i = n_{i,\infty} e^{\frac{-ze\phi}{kT}}. \tag{3.9}$$

From electrostatics, we also have a relationship between the net charge density and the shape of the potential (Poisson equation). For a monovalent system,

$$\frac{d^2\phi}{dx^2} = -\frac{\rho_{\text{f}}}{\varepsilon\varepsilon_0} = \frac{zen_\infty}{\varepsilon\varepsilon_0}\left(e^{\frac{ze\phi}{kT}} - e^{\frac{-ze\phi}{kT}}\right). \tag{3.10}$$

The combination of Eqs. 3.9 and 3.10 constitutes the Poisson-Boltzmann equation. The solution to this differential equation for a monovalent species (Gouy-Chapman

solution) is

$$\phi = \frac{4kT}{ze}\tanh^{-1}\left[e^{-\kappa x}\tanh\left(\frac{ze\phi_{\text{dif},0}}{4kT}\right)\right]; \quad \kappa = \sqrt{\frac{2e^2 n_\infty}{\varepsilon\varepsilon_0 kT}} \tag{3.11}$$

where $\frac{1}{\kappa}$ is the Debye length. Plugging in this solution into the Boltzmann equation (Eq. 3.9) will result in concentration as a function of x. Then, integrating $n_i - n_{i,\infty}$ from ∞ to 0 (bulk to surface) recovers the surface excess. We should expect from charge neutrality that

$$\Gamma_{\text{mon}} + \Gamma_{\text{s,dif}} = \Gamma_{\text{c,dif}} \tag{3.12}$$

where Γ_{mon} is the amount of surfactant adsorbed at the monolayer, $\Gamma_{\text{s,dif}}$ is the amount of surfactant excess in the diffuse layer (should be negative), and $\Gamma_{\text{c,dif}}$ is the excess of counterions in the diffuse layer. We find that the total number of surfactants in the monolayer is

$$\Gamma_{\text{mon}} = \frac{\sqrt{8n_\infty \varepsilon\varepsilon_0 kT}}{e}\sinh\left(\frac{e\phi_{\text{dif},0}}{2kT}\right) \tag{3.13}$$

which is equivalent to the well-known Grahame equation that describes the charge density of a double layer:

$$\sigma = \sqrt{8n_\infty \varepsilon\varepsilon_0 kT}\sinh\left(\frac{ze\phi_{\text{dif},0}}{2kT}\right). \tag{3.14}$$

Thus, rearranging Eq. 3.13 yields an equation for the diffuse layer potential:

$$\phi_{\text{dif},0} = \frac{2kT}{e}\sinh^{-1}\left(\frac{e\Gamma_{\text{mon}}}{\sqrt{8n_\infty \varepsilon\varepsilon_0 kT}}\right). \tag{3.15}$$

It should be noted that $\sinh^{-1}(z) = \ln\left(z + \sqrt{1+z^2}\right)$—a logarithmic expression—suggesting that the diffuse potential resembles a chemical potential. This psuedo-chemical potential has a dependency on temperature, which can be expected since the diffuse layer is a result of chemical arrangement due to a competition of thermal kinetics and electrostatic forces.

3.3.3 Stern gap potential

The Stern layer gap between two potentials can be conveniently modeled as a flat-plate capacitor. This results in the potential within the gap being

$$\phi_{\text{gap}}(x) = \frac{\sigma}{\varepsilon_{\text{gap}}\varepsilon_0}(s_{\text{dif}} - x) + \phi_{\text{dif},0} = \frac{e\Gamma_{\text{mon}}}{\varepsilon_{\text{gap}}\varepsilon_0}(s_{\text{dif}} - x) + \phi_{\text{dif},0} \tag{3.16}$$

where ε_{gap} is the effective dielectric constant. Based on the recommendation from Mulqueen et al. where $\varepsilon_{\text{gap}} = 42$ [74] at 25 °C, the approximation

$$\varepsilon_{\text{gap}}(T) = \frac{42}{\varepsilon_0(25\,^\circ\text{C})}\varepsilon_0(T) \tag{3.17}$$

is used to capture the temperature dependency of ε_{gap}. $\varepsilon_0(T)$ can be conveniently approximated by $\varepsilon_0(T) = 10^{1.94315 - 0.0019720\frac{T-273.15\,\text{K}}{1\,\text{K}}}$ [77].

Combining the diffuse and gap potentials (Eqs. 3.15 and 3.16) reveals the full monolayer potential in terms of Γ_{mon}.

$$\phi_{\text{mon}} = \frac{e\Gamma_{\text{mon}}}{\varepsilon_{\text{gap}}\varepsilon_0}\delta_{\text{gap}} + \frac{2kT}{e}\sinh^{-1}\left(\frac{e\Gamma_{\text{mon}}}{\sqrt{8n_\infty\varepsilon\varepsilon_0 kT}}\right). \tag{3.18}$$

This is the main EDL result that will be incorporated in to the statistical mechanical model.

3.4 Statistical mechanical model

3.4.1 The partition function

The general form of the partition function used relates a 2D phase to a 3D bulk phase and is the same one used to derive the well-known Langmuir equation [78]:

$$Z = \underbrace{\frac{\zeta^N}{N!}}_{\text{partition function for } N \text{ indistinguishable particles}} \times \underbrace{\frac{(A/a_{\text{exc}})!}{(A/a_{\text{exc}} - N)!N!}}_{\text{combinations to occupy } A/a_{\text{exc}} \text{ sites}}. \tag{3.19}$$

The partition function consists of a partition function for N indistinguishable particles, each with their own single-particle partition function, ζ. This is then multiplied by the number of combinations to occupy the available adsorption sites. For a classical, continuous single-particle system confined to two dimensions, the single-particle partition function, ζ, is an integration over phase space [79]:

$$\zeta = \frac{1}{h^2} \int e^{-\frac{E}{kT}} d^2\mathbf{r} d^2\mathbf{p} \tag{3.20}$$

where h is the Planck constant and E is the energy of a single particle. The key parameter in Eq. 3.20 is the energy E. How E is defined essentially determines all thermodynamic terms and the behavior of the system. In our system, we consider kinetic energy, van der Waals (vdW) interaction energy, electrostatic potential, and potential energy:

$$E = \underbrace{\frac{p^2}{2m}}_{\text{kinetic}} + \underbrace{\frac{\overline{w}}{2}}_{\text{vdW}} + \underbrace{e\phi}_{\text{electrostatic}} + \underbrace{g_{\text{mon}}}_{\text{potential}} . \tag{3.21}$$

Note that the mean interaction term $\overline{w}$ (Eq. 3.7) is divided by two since it is derived from the mutual interaction $u(r)$ potential between two particles (chains in this case). Also note that neglecting all energy terms except potential energy ($E = g_{\text{mon}}$), which is a constant for a given temperature and pressure, yields the Langmuir isotherm. Integrating Eq. 3.20 produces the final partition function.

$$Z = \frac{\left((A - N a_{\text{exc}}) \exp\left(\frac{-a\Gamma/2 - e\phi - g_{\text{mon}}}{kT}\right)/\Lambda^2\right)^N}{N!} \frac{(A/a_{\text{exc}})!}{(A/a_{\text{exc}} - N)!N!} \tag{3.22}$$

Here, Λ is the thermal de Broglie wavelength and is defined as

$$\Lambda \equiv \frac{h}{\sqrt{2\pi m k T}}. \tag{3.23}$$

3.4.2 Deriving thermodynamic terms

Internal energy

Using the relation $U = kT^2 \frac{\partial}{\partial T}(\ln Z)$ along with Stirling's approximation $\ln(N!) \approx N\ln(N) - N$, the internal energy can be obtained from the partition function (Eq. 3.22):

$$U = N\left(\underbrace{kT}_{\text{kinetic}} + \underbrace{\frac{\alpha\Gamma}{2}}_{\text{vdW}} + \underbrace{\frac{\delta_{\text{gap}} e^2 \Gamma}{\varepsilon_{\text{gap}}\varepsilon_0}}_{\text{Stern EDL}} + \underbrace{\frac{ekT\Gamma}{\sqrt{e^2\Gamma^2 + 8n_\infty \varepsilon\varepsilon_0 kT}}}_{\text{diffuse EDL}} + \underbrace{g_{\text{mon}} - T\frac{dg_{\text{mon}}}{dT}}_{\text{potential}}\right). \quad (3.24)$$

From inspection, it is apparent that internal energy consists of a 2D kinetic gas internal energy (NkT), vdW interaction energy, EDL contributions, and the adsorption potential energy, g_{mon}. Remarkably, the whole electrostatic potential, ϕ_{mon}, from Eq. 3.18 does not appear here (no logarithmic $\sinh^{-1}$ term). Instead, we have a square-root term, which represents a derivative of $\phi_{\text{dif},0}$ with respect to T. Note that we have assumed the temperature dependencies of the bulk concentration, the dielectric constant, and the vdW interaction parameter are negligible.

Entropy

The entropy can also be explicitly derived by evaluating $S = \frac{\partial}{\partial T}(kT\ln Z)$ to obtain

$$\frac{S}{Nk} = \underbrace{2 + \ln\left(\frac{1-\Gamma a_{\text{exc}}}{\Gamma\Lambda^2}\right)}_{\text{kinetic}} + \underbrace{\frac{1}{\Gamma a_{\text{exc}}}\ln\left(\frac{1}{1-\Gamma a_{\text{exc}}}\right) + \ln\left(\frac{1-\Gamma a_{\text{exc}}}{\Gamma a_{\text{exc}}}\right)}_{\text{Langmuir}}$$
$$+ \underbrace{\frac{e\Gamma}{\sqrt{e^2\Gamma + 8n_\infty\varepsilon\varepsilon_0 kT}} - 2\sinh^{-1}\left(\frac{e\Gamma}{\sqrt{8n_\infty\varepsilon\varepsilon_0 kT}}\right)}_{\text{diffuse EDL}} - \underbrace{\frac{1}{k}\frac{dg_{\text{mon}}}{dT}}_{\text{potential}}. \quad (3.25)$$

The kinetic terms are a 2D version of the Sackur-Tetrode equation for hard sphere ideal gases. Similar to our treatment of internal energy, we have assumed that temperature dependencies on the bulk concentration, the dielectric constant, and the vdW interaction parameter are negligible. A temperature-dependent potential en-

ergy appears as it did in the internal energy.

Surface pressure

Conventional 3D pressure is obtained from the partition function by

$$P = kT\left(\frac{\partial \ln Z}{\partial V}\right)_{N,T}, \tag{3.26}$$

but in the case of the monolayer, it is constrained to a thickness δ_{mon}. Furthermore, from the pressure tensor, the pressure has the normal isotropic component, P, and an additional lateral surface pressure component, Π. Thus, instead of a volume derivative, an area derivative can be used:

$$P\delta_{\text{mon}} + \Pi = kT\left(\frac{\partial \ln Z}{\partial A}\right)_{N,T}. \tag{3.27}$$

A surface pressure equation of state can then be explicitly derived:

$$\Pi = \underbrace{\frac{\Gamma kT}{1-\Gamma a_{\text{exc}}}}_{\text{kinetic}} + \underbrace{\frac{\alpha}{2}\Gamma^2}_{\text{vdW}} + \underbrace{\frac{\delta_{\text{gap}} e^2}{\varepsilon_{\text{gap}}\varepsilon_0}\Gamma^2}_{\text{Stern EDL}} + \underbrace{\frac{2ekT\Gamma^2}{\sqrt{e^2\Gamma^2 + 8n_\infty \varepsilon\varepsilon_0 kT}}}_{\text{diffuse EDL}} + \underbrace{\frac{kT}{a_{\text{exc}}}\ln\left(\frac{1}{1-\Gamma a_{\text{exc}}}\right)}_{\text{Langmuir}} - P\delta_{\text{mon}}. \tag{3.28}$$

From inspection, the first two terms on the right-hand side are the same as the van der Waals equation of state. The third and fourth terms represent contributions from the Stern and diffuse EDL, respectively. The $\frac{kT}{a_{\text{exc}}}\ln\left(\frac{1}{1-\Gamma a_{\text{exc}}}\right)$ term is a non-kinetic force that keeps molecules from packing too densely and is the surface pressure of a Langmuir film. From Eq. 3.25, this term is embodied in the entropy and can be interpreted as an entropic force resulting from the maximization of the number of ways the monolayer can be organized. This term is fundamental as it is derived from the number of combinations to occupy adsorption sites in the partition function (Eq. 3.19). However, this term is absent from other surfactant equations of state in the literature as they are not derived from the partition function. This term can become very important at high surface concentrations. The final $P\delta_{\text{mon}}$ term is a negligible atmospheric pressure component.

Chemical potential

By the relation $\mu = \left(\frac{\partial F}{\partial N}\right)_{T,V} = -kT\frac{\partial \ln Z}{\partial N}$, a 2D chemical potential can also be explicitly derived:

$$\mu = kT\ln\left(\underbrace{\frac{\exp\left(\frac{\Gamma a_{\text{exc}}}{1-\Gamma a_{\text{exc}}} + \frac{\alpha\Gamma}{kT} + \frac{\delta_{\text{gap}}e^2\Gamma}{\varepsilon_{\text{gap}}\varepsilon_0 kT} + \frac{2e\Gamma}{\sqrt{e^2\Gamma^2+8n_\infty\varepsilon\varepsilon_0 kT}}\right)}{1-\Gamma a_{\text{exc}}}}_{\text{activity coefficient}}\Lambda^2\Gamma\right)$$
$$+\underbrace{\frac{\delta_{\text{gap}}e^2\Gamma}{\varepsilon_{\text{gap}}\varepsilon_0} + 2kT\sinh^{-1}\left(\frac{e\Gamma}{\sqrt{8n_\infty\varepsilon\varepsilon_0 kT}}\right)}_{\text{EDL }(e\phi_{\text{mon}})} + \underbrace{g_{\text{mon}}}_{\text{potential}} + \underbrace{kT\ln\frac{\Gamma a_{\text{exc}}}{1-\Gamma a_{\text{exc}}}}_{\text{Langmuir}} \quad (3.29)$$

where we have placed the activity coefficient inside the logarithm and other potentials outside. When the activity coefficient is unity, the system behaves like an ideal 2D gas. The full monolayer potential is recovered here as we would expect since the generic form of the electrochemical potential is $\mu = \mu^\circ + kT\ln X + ze\phi$. The potential energy, g_{mon}, appears by itself; thus, it is apparent that g_{mon} is usually absorbed by the standard state chemical potential in other descriptions. The final term, $kT\ln\frac{\Gamma a_{\text{exc}}}{1-\Gamma a_{\text{exc}}}$, can be interpreted as being an additional entropic potential (this term appears in the entropy in Eq. 3.25) that becomes extremely negative when there are few molecules at the surface, thereby favoring adsorption. On the other hand, it becomes extremely positive when the surface concentration of surfactants is near its capacity, thereby discouraging further adsorption

Normally, chemical potential in 3D systems is based on the Gibbs energy (chemical potential is the partial molar Gibbs energy). However, for this 2D system, evaluating the partial molar Gibbs energy results in a dependency on the extensive variable A, which is unphysical since chemical potential should only be a function of *intensive* variables. However, it turns out that combining Eqs. 3.24, 3.28, and 3.25 reveals that Eq. 3.29 is the partial molar quantity of a generalized Gibbs potential defined as $\tilde{G} \equiv U + PV + \Pi A - TS$ (a Legendre transformation; see Appendix B.3 for more discussion on this generalized Gibbs potential). And remarkably, the differential form of this generalized Gibbs potential, $d\tilde{G} = -SdT + VdP + \mu dN + Ad\Pi$,

depends only on the intensive variables T, P, and Π.[2] Thus, the statistical mechanical potentials derived from the partition function show thermodynamic consistency.

Furthermore, it can be shown from simple mathematical and thermodynamic arguments that the surface pressure of a monolayer should be (Appendix B.4)

$$\Pi = kT\Gamma + kT\int_{n_\infty}^{n(x)} \frac{n}{f}\frac{\partial f}{\partial n}dn + \int_{\psi_\infty}^{\psi(x)} n_i d\psi. \tag{3.30}$$

where f is the activity coefficient and ψ is all the terms trailing the logarithm of Eq. 3.29 (potential energies). Plugging in our chemical potential derived from statistical mechanics (Eq. 3.29) into our general thermodynamic formula for surface tension (Eq. 3.30) also recovers the same surface pressure equation of state derived from statistical mechanics (Eq. 3.28). Thus, this is further indication of the thermodynamic consistency in our approach.

3.4.3 Adsorption isotherm

Equating the monolayer chemical potential (Eq. 3.29) to the an idealized bulk concentration ($\bar{\mu}_{\text{bulk}} = kT\ln\left(\Lambda^3 n_\infty\right)$),[3] we obtain the adsorption in the form of a Boltzmann equation relating the bulk concentration to the monolayer concentration:

$$n_\infty = \frac{\exp\left(\frac{\Gamma a_{\text{exc}}}{1-\Gamma a_{\text{exc}}} + \frac{a\Gamma}{kT} + \frac{2\delta_{\text{gap}}e^2\Gamma}{\varepsilon_{\text{gap}}\varepsilon_0 kT} + \frac{2e\Gamma}{\sqrt{e^2\Gamma^2+8n_\infty\varepsilon\varepsilon_0 kT}} + 2\sinh^{-1}\left(\frac{e\Gamma}{\sqrt{8n_\infty\varepsilon\varepsilon_0 kT}}\right) + \frac{g_{\text{mon}}}{kT}\right)}{\Lambda(1-\Gamma b)^2}\Gamma^2 a_{\text{exc}}. \tag{3.31}$$

In terms of thermodynamic variables, this works out to

$$n_\infty = \frac{1}{\Lambda^3}\exp\left(\frac{U/N + (P+\Pi)/\Gamma - TS/N}{kT}\right). \tag{3.32}$$

[2] N is not considered here since evaluating partial molar properties sets $dN = 0$.

[3] In actuality, even dilute solutions do not behave perfectly ideal; however, assuming $\mu \propto \ln\left(\Lambda^3 n_\infty\right)$, any deviation from ideal should be absorbed by g_{mon} which will be determined later.

This adsorption isotherm can also be expressed in the form of a Frumkin isotherm.

$$n_\infty = \frac{1}{K_L}\left(\frac{\Gamma a_{exc}}{1-\Gamma a_{exc}}\right)e^{-A_F \Gamma a_{exc}} \tag{3.33}$$

where

$$K_L = \Lambda^3 \exp\left(-\frac{\Gamma a_{exc}}{1-\Gamma a_{exc}} - \frac{\alpha\Gamma}{2kT} \underbrace{-\frac{\delta_{gap} e^2 \Gamma}{\varepsilon_{gap}\varepsilon_0 kT} - 2\sinh^{-1}\left(\frac{e\Gamma}{\sqrt{8n_\infty \varepsilon\varepsilon_0 kT}}\right)}_{\frac{-\psi}{kT}} - \frac{g_{mon}}{kT} + \ln\left(\frac{1-\Gamma a_{exc}}{\Gamma\Lambda^2}\right)\right), \tag{3.34}$$

$$A_F = -\frac{\alpha}{2a_{exc}kT} - \frac{\delta_{gap}e^2}{b\varepsilon_{gap}\varepsilon_0 kT} - \frac{2e}{a_{exc}\sqrt{e^2\Gamma^2 + 8n_\infty \varepsilon\varepsilon_0 kT}}. \tag{3.35}$$

In terms of thermodynamic variables, this works out to

$$K_L = \Lambda^3 \exp\left(\frac{-(U-TS)/N}{kT} - \frac{\left(\frac{\Gamma kT}{1-\Gamma a_{exc}} + \frac{kT}{a_{exc}}\ln\left(\frac{1}{1-\Gamma a_{exc}}\right)\right)/\Gamma}{kT} + \ln\left(\frac{\Gamma a_{exc}}{1-\Gamma a_{exc}}\right)\right), \tag{3.36}$$

$$A_F = -\frac{1}{\Gamma a_{exc}}\left(\underbrace{\frac{(P+\Pi)/\Gamma}{kT} - \frac{\left(\frac{\Gamma kT}{1-\Gamma a_{exc}} + \frac{kT}{a_{exc}}\ln\left(\frac{1}{1-\Gamma a_{exc}}\right)\right)/\Gamma}{kT}}_{\text{non-kinetic, non-entropic surface interactions}}\right). \tag{3.37}$$

From here, the limiting behavior of this isotherm can be analyzed. The K_L term resembles the Langmuir constant (not actually a constant in this case) and represents the potential energy and entropic change (Helmholtz energy) between bulk and surface. The A_F term is like the Frumkin constant (again, not actually a constant) and represents the interactions between adsorbed molecules and, in the non-interactive case, this term becomes zero resolving the Langmuir equation. The terms can be slightly modified if the adsorbates can be modeled as stationary (not kinetic). Then, there would not be any kinetic term; therefore, terms like $\frac{\Gamma kT}{1-\Gamma a_{exc}}$ would be dropped wherever it appears. Furthermore, the electric potential terms would be dropped if the species is nonionic. Thus, in the limit that there are no interactions and the

fraction of occupied sites, Γa_{exc}, is small, then one would simply obtain Henry's law.

3.4.4 Additional contribution of the EDL

For ionic surfactants, evaluating the equation of state derived from statistical mechanics (Eq. 3.28) only recovers the surface tension contribution of the monolayer itself. To get the full surface pressure, the contribution from the electric double layer must also be incorporated. First, we use the formula (Appendix B.4)

$$\Pi_{dif} = \sum_i kT\Gamma_i + \sum_i kT \int_{s_{dif}}^{\infty} \int_{n_{i,\infty}}^{n_i(x)} \frac{n_i}{f_i}\frac{\partial f_i}{\partial n_i} dn_i dx + \sum_i \int_{s_{dif}}^{\infty} \int_0^{\phi(x)} z_i e n_i d\phi dx \quad (3.38)$$

evaluated across the diffuse EDL using the Poisson-Boltzmann solution for the surfactant and the counterion species to obtain a surface pressure associated with the diffuse layer, Π_{dif}. We assume the surfactant and counterion species behave ideally so the middle term is dropped. This yields an energy per adsorbed surfactant, Π_{dif}/Γ, of

$$kT + \frac{1}{\Gamma}\frac{2kT\sqrt{8n_\infty kT\varepsilon\varepsilon_0}\sinh\left(\frac{1}{2}\sinh^{-1}\left(\frac{e\Gamma}{2\sqrt{2n_\infty kT\varepsilon\varepsilon_0}}\right)\right)^2}{e}. \quad (3.39)$$

This is input into the partition function and the surface pressure, chemical potential, and adsorption isotherm are re-derived resulting in slightly modified equations. The new surface pressure is now

$$\Pi = \underbrace{\frac{\Gamma kT}{1-\Gamma a_{exc}} + \frac{\alpha}{2}\Gamma^2 + \frac{\delta_{gap}e^2}{\varepsilon_{gap}\varepsilon_0}\Gamma^2 + \frac{2ekT\Gamma^2}{\sqrt{e^2\Gamma^2 + 8n_\infty\varepsilon\varepsilon_0 kT}} + \frac{kT}{a_{exc}}\ln\left(\frac{1}{1-\Gamma a_{exc}}\right) - P\delta_{mon}}_{\text{Eq. 3.28}}$$
$$+ \underbrace{\frac{ekT\Gamma^2}{\sqrt{e^2\Gamma^2 + 8n_\infty\varepsilon\varepsilon_0 kT}} - \frac{2kT\sqrt{8n_\infty kT\varepsilon\varepsilon_0}\sinh\left(\frac{1}{2}\sinh^{-1}\left(\frac{e\Gamma}{\sqrt{8n_\infty kT\varepsilon\varepsilon_0}}\right)\right)^2}{e}}_{\text{new diffuse EDL contribution}} \quad (3.40)$$

and the new chemical potential is now

$$\mu = kT \ln \left(\frac{\exp\left(\frac{\Gamma a_{\text{exc}}}{1-\Gamma a_{\text{exc}}} + \frac{a\Gamma}{kT} + \frac{\delta_{\text{gap}} e^2 \Gamma}{\varepsilon_{\text{gap}} \varepsilon_0 kT} + \frac{3e\Gamma}{\sqrt{e^2\Gamma^2 + 8n_\infty \varepsilon \varepsilon_0 kT}} \right)}{1-\Gamma a_{\text{exc}}} \Lambda^2 \Gamma \right)$$
$$+ \frac{\delta_{\text{gap}} e^2 \Gamma}{\varepsilon_{\text{gap}} \varepsilon_0} + 2kT \sinh^{-1}\left(\frac{e\Gamma}{\sqrt{8n_\infty \varepsilon \varepsilon_0 kT}} \right) + g_{\text{mon}} + kT \ln \frac{\Gamma a_{\text{exc}}}{1-\Gamma a_{\text{exc}}}. \quad (3.41)$$

where the only difference is the additional $\frac{e\Gamma}{\sqrt{e^2\Gamma^2+8n_\infty \varepsilon \varepsilon_0 kT}}$ in the activity coefficient. The new adsorption isotherm also has the same modification since it is derived from the chemical potential:

$$n_\infty = \frac{\exp\left(\frac{\Gamma a_{\text{exc}}}{1-\Gamma a_{\text{exc}}} + \frac{a\Gamma}{kT} + \frac{2\delta_{\text{gap}} e^2 \Gamma}{\varepsilon_{\text{gap}} \varepsilon_0 kT} + \frac{3e\Gamma}{\sqrt{e^2\Gamma^2 + 8n_\infty \varepsilon \varepsilon_0 kT}} + 2\sinh^{-1}\left(\frac{e\Gamma}{\sqrt{8n_\infty \varepsilon \varepsilon_0 kT}} \right) + \frac{g_{\text{mon}}}{kT} \right)}{\Lambda (1-\Gamma b)^2} \Gamma^2 a_{\text{exc}}. \quad (3.42)$$

From here, whenever the equation of state (Eq. 3.28), chemical potential (Eq. 3.29), or adsorption isotherm (Eq. 3.31) is mentioned, note that the aforementioned additional EDL modifications have been made when the surfactant is ionic.

3.5 Evaluation and validation

3.5.1 Numerical evaluation

The evaluation of the equation of state (Eq. 3.28) and the adsorption isotherm (Eq. 3.31) to obtain the surface tension equation of state is non-trivial and the numerical procedure is described here. This is mainly due to the fact that Eq. 3.31 is a transcendental equation involving the bulk concentration, n_∞, and surface adsorption, Γ_{mon}. To solve the system, a table of values Γ_{mon} ranging from $\frac{1}{a_{\text{exc}}}$ to an arbitrarily small value (logarithmically spaced) is generated. For each value in this table, a root-solving algorithm is performed for Eq. 3.31 to obtain values for n_∞, which are subsequently input into Eq. 3.28 to obtain surface tension values. Plotting the equation of state as a function of Γ_{mon} reveals a phase change instability similar to

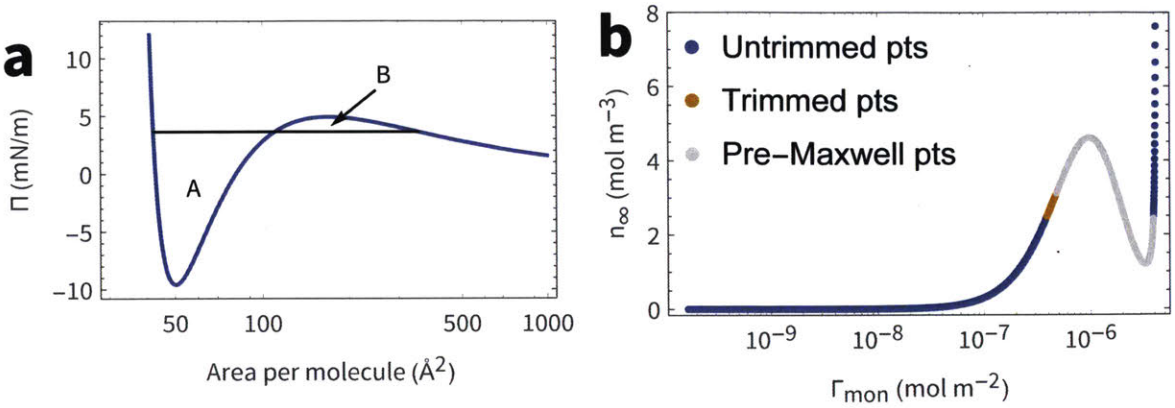

Figure 3-4: **2D EOS instability and Maxwell construction.** (a) The black line is the Maxwell construction which divides the curve (blue) such that the area below (A) and above (B) it are equal. (b) Performing a Maxwell construction removes the points in grey on a plot of n_∞ versus Γ_{mon}. Further trimming (orange points) is needed to obtain monotonicity.

that of the van der Waals equation of state. An example of this instability is shown in Figure 3-4.

The presence of this instability implies that a change of phase is occurring. Surfactants with longer tails and stronger attraction are more prone to having this behavior and collapsing into a condensed phase, and this behavior has been observed experimentally [80]. If the equation of state is left as is, then this creates non-monotonic behavior and the surface tension isotherm can yield multiple values for a single concentration. To correct this, a Maxwell construction is applied such that the net ΠA work between two states is equal to zero (black line in Figure 3-4a). Even after performing the Maxwell construction (which removes the gray points in Figure 3-4b) though, the adsorption isotherm can still show non-monotonic behavior (Figure 3-4b). Therefore, the orange points in Figure 3-4b are trimmed, which leaves both the equation of state and adsorption isotherm monotonic. Choosing the points to the left of instability in Figure 3-4b rather than the right ensures continuity in the surface tension isotherm.

3.5.2 Molecular parameters

The potential energy, g_{mon}, still remains the primary unknown in the model. However, given that this term constitutes the change in standard state chemical potential between the monolayer and bulk phases, it should resemble the other forms of $\Delta\mu^{\circ}$. Since adsorption is primarily dictated by the hydrophobic effect[4] of the alkyl tails, $\Delta\mu^{\circ}$ should resemble that of alkane gas solubility in water. Henry's law constant, K_{H}, is a parameter that is directly proportional to $\Delta\mu^{\circ}$ and is well documented for a variety of systems. In particular, Abraham and Matteoli determined Henry's law constants as functions of temperatures for several alkanes in water and found that they obey the following functional form [81]:

$$\ln K_{\text{H}} = L \ln \frac{T}{1\,\text{K}} + \frac{B}{T} + C. \tag{3.43}$$

Since $K_{\text{H}} \propto n_{\text{c}}$, this necessitates that $L \propto n_{\text{c}}$, $B \propto n_{\text{c}}$, and $C \propto n_{\text{c}}$. In the context of surfactants, tails do not fully determine the hydrophobic effect; there should also be an effect of heads. Thus, we assume g_{mon} takes the form

$$\frac{g_{\text{mon}}}{kT} = -(L \ln \frac{T}{1\,\text{K}} + \frac{B}{T} + C) + \frac{g_{\text{head}}}{kT} \tag{3.44}$$

where g_{head} is the deviation from pure tail behavior and should only depend on the head. Therefore, an entire family of surfactants with the same head, should have the same g_{head} parameter. The following expressions for L, B, and C were determined to be suitable for various alkyl terminated surfactants.

$$L = -40.0000 - 2.50000 n_{\text{c}} \tag{3.45}$$

$$B = (-11000.0 - 1000.00 n_{\text{c}})\,\text{K} \tag{3.46}$$

$$C = 264.855 + 18.3843 n_{\text{c}} \tag{3.47}$$

[4]This is the tendency of hydrocarbons to be desolvated from water.

Table 3.1: Molecular head parameters for several families of alkyl-terminated surfactants

Surfactant family	$\frac{g_{head}}{kT}$	a_{exc} (Å^2)	δ_{gap} (Å)
MEGA	-3.8	38.4	N/A
SS	-11.9	35.2	0.8
TAB	-10.5	35.2	0.8
E4	-8.50	48.0	N/A
E5	-8.88	52.0	N/A
E6	-9.25	56.0	N/A
E8	-10.0	64.0	N/A

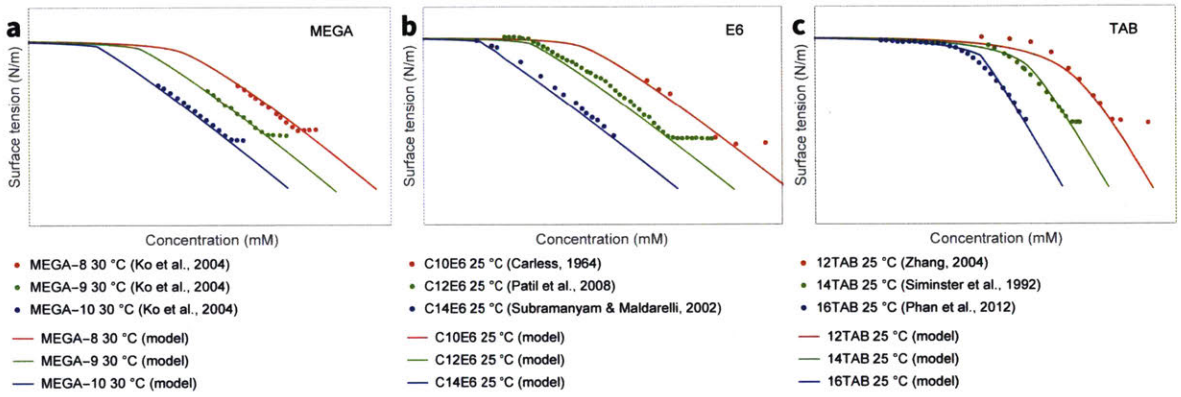

Figure 3-5: **Surface tension model validated with literature data.** Data and model for (a) MEGA-8 [82], MEGA-9 [82], MEGA-10 [82], (b) C10E6 [83], C12E6 [84], C14E6 [80], and (c) 12TAB [85], 14TAB [86], and 16TAB [87] show good agreement.

Furthermore, g_{head} was determined for several families of surfactants based on literature data as shown in Table 3.1.

3.6 Equilibrium surface tension validation

The results of this equilibrium surface tension model agree well with literature data of surface tension isotherms as shown in Figure 3-6. Here, three families of surfactants are used but only one fitting parameter, g_{head}, per family has been applied. Furthermore, Figure 3-6 (own data) shows good agreement with temperature dependence in addition to concentration dependence for MEGA-10.

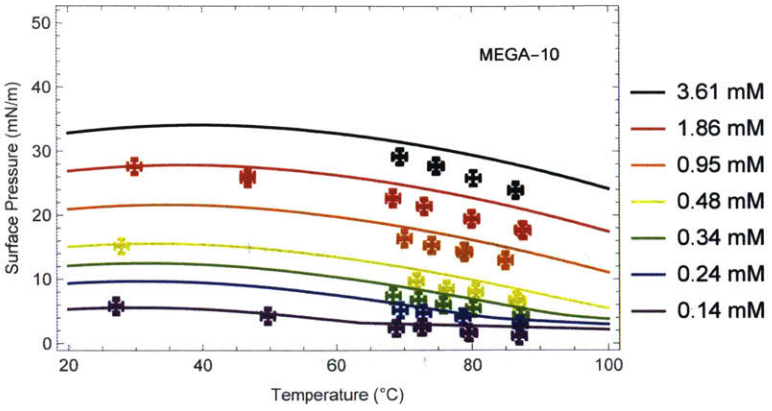

Figure 3-6: **Surface tension model validated with MEGA-10 for temperature and concentration dependence.**

3.7 Dynamic surface tension

In this Section, we will describe how to obtain dynamic surface tension from equilibrium surface tension using a dynamic surface tension model. Depending on surfactant concentration and type, equilibration timescales can span milliseconds to hours. One key parameter that must be known before applying the dynamic surface tension model is the diffusion constant.

3.7.1 Diffusion constant calculation

A simple method for calculating the diffusion constant, a key property in dynamic surface tension, was developed and is presented here. The well-known Stokes-Einstein equation is usually used when calculating diffusion constant, D:

$$D = \frac{kT}{n\pi\eta r_{\text{eff}}} \tag{3.48}$$

where n is a constant (6 for large spherical particles), η is the dynamic viscosity of water, and r_{eff} is the effective spherical particle radius of the molecule. Based on MD simulations of alkanes over a wide range of temperatures and pressures [88], $n = 5$ provides reasonably accurate results. As for r_{eff}, Tee et al. evaluated r_{eff} for a variety of alkanes [89]. Based on this data, the following equation provides a correlation

for r_{eff} of alkanes:

$$r_{\text{eff}} = \left(1.660\,84 \times 10^{-10} + 2.737\,93 \times 10^{-11} n_{\text{c}}\right) \text{m} \tag{3.49}$$

Therefore, to find the diffusion constant of a surfactant, the diffusion constant of an alkane with the same n_{c} is first calculated using Eqs. 3.48 and 3.49. Then, the alkane diffusion constant is scaled by the molecular weight to the power of $-1/3$. That is,

$$D_{\text{surfactant}} = D_{\text{alkane}} \frac{M_{\text{alkane}}^{1/3}}{M_{\text{surfactant}}^{1/3}}. \tag{3.50}$$

where $M_{\text{surfactant}}$ is the molecular weight of the surfactant without its counterion.[5] The $M^{-1/3}$ dependency is a general scaling assuming similar density and is reasonable to apply here due to the the small differences in M between a surfactant and its associated alkane.

3.7.2 Dynamic surface tension model

Most models for dynamic surface tension are either completely empirical and have several fitting parameters [90] or require the assumption of a particular isotherm [91]. Established theory based on the work of Ward and Tordai [45] that assumes diffusion-limiting behavior can be used to extract dynamic behavior from equilibrium behavior. The basics of this theory starts with the governing 1D-diffusion equation:

$$\frac{\partial n(x)}{\partial t} = D \frac{\partial^2 n(x)}{\partial x^2}. \tag{3.51}$$

Using conservation of mass, the following boundary condition is applied

$$\frac{\partial \Gamma_{\text{mon}}}{\partial t} = D \left(\frac{\partial n(x)}{\partial x} \right)_{x=0}. \tag{3.52}$$

[5] The counterion is not considered since full dissociation is assumed and transport would be limited by the much heavier and larger surfactant.

Solving Eq. 3.51 gives the Ward-Tordai equation.

$$\Gamma_{\text{mon}}(t) = \sqrt{\frac{D}{\pi}}\left(\underbrace{2n_\infty\sqrt{t}}_{\text{"forward"}} - \underbrace{\int_0^t \frac{n_s(\tau)}{\sqrt{t-\tau}}d\tau}_{\text{"backward"}}\right) \tag{3.53}$$

where τ is a dummy variable, n_∞ is the bulk concentration ($x \to \infty$), and n_s is the subsurface concentration (concentration at $x = 0$). This equation is often interpreted as having a "forward" diffusion component (diffusion from bulk to an empty subsurface) and a "backward" history-dependent term (slows down diffusion due to the existence of a finite concentration at the subsurface). If fast equilibration is to be assumed, then $n_s(\tau) = n_s(\Gamma_{\text{mon}}(\tau))$ where $n_s(\Gamma_{\text{mon}})$ is the equilibrium adsorption isotherm (Eq. 3.31; infinitely fast kinetics assumption).

However, an issue with the Ward-Tordai equation is the assumption of an infinitesimally thin monolayer, which can lead to unphysically high diffusion. Thus, a modified Ward-Tordai equation developed by Diamant and Andelman that accounts for the thickness of the monolayer [92] is used:

$$\Gamma_{\text{mon}}(t) = \frac{V_m}{N_A a_{\text{exc}}\left(\delta_{\text{mon}} + \frac{1}{\kappa}\right)}\sqrt{\frac{D}{\pi}}\left(\underbrace{2c_\infty\sqrt{t}}_{\text{"forward"}} - \underbrace{\int_0^t \frac{n_s(\Gamma_{\text{mon}}(\tau))}{\sqrt{t-\tau}}d\tau}_{\text{"backward"}}\right) + \underbrace{\frac{V_m}{N_A a_{\text{exc}}}(2c_\infty - c_0(\Gamma(\tau)))}_{\text{finite monolayer thickness correction}}. \tag{3.54}$$

Here, V_m is the molar volume (calculated from alkane molar volume and a_{exc} of the heads), δ_{mon} is the length of the monolayer (taken to be the length of the alkane tail plus twice the head diameter), $\frac{1}{\kappa}$ is the Debye length, and N_A is the Avogadro constant. In Diamant and Andelman's original expression, this equation was derived for nonionic surfactants and, therefore, the Debye length was not included. In this work, we have found that including the Debye length is an acceptable approximation for the ionic surfactants studied. Using a numerical algorithm devised by Li et al.

[91], Eq. 3.54 with the adsorption isotherm (Eq. 3.31) applied can be integrated. From there, plugging in $\Gamma_{\text{mon}}(t)$ into the equation of state (Eq. 3.28) yields the dynamic surface tension.

3.7.3 Validation of the dynamic surface tension model

Ultra low-CMC nonionic surfactant

For the very low-CMC nonionic surfactant C14E6 (CMC $\approx$ 0.01 mM), the model provides reasonable agreement with data provided by Subramanyan and Maldarelli [80] despite the extremely long timescales involved (several hours) (see Figure 3-7). In fact, the predicted phase change behavior coincides with the observed phase change behavior. Some deviation may be due to non-first-order phase-change behavior observed in actual surfactant systems, whereas the Maxwell construction provides first-order behavior.

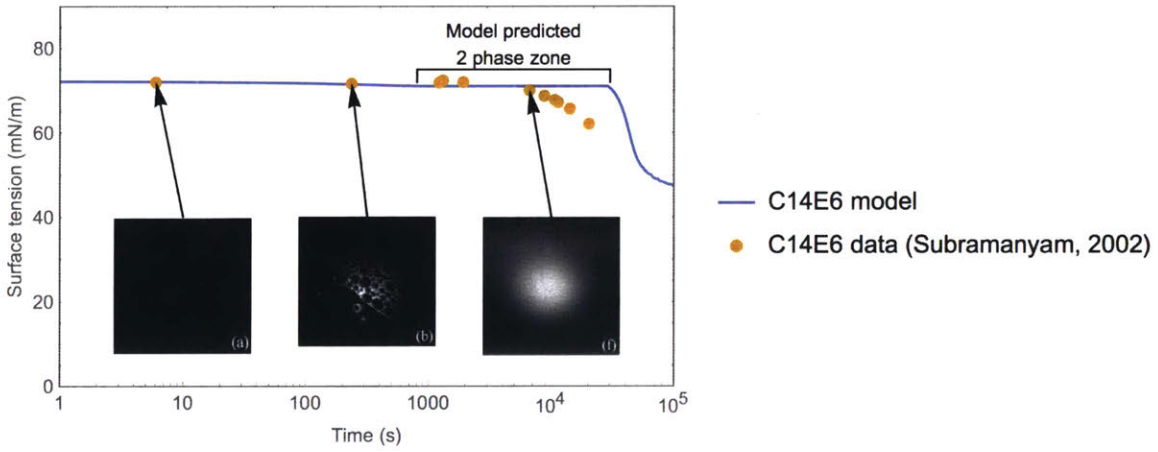

Figure 3-7: **Dynamic surface tension validation for C14E6.** Data taken from Subramanyan and Maldarelli [80].

Medium-CMC nonionic surfactant

For the medium-CMC surfactant MEGA-10 (CMC $\approx$ 4 mM), the model provides reasonable agreement at different concentrations and temperatures (see Figure 3-8). The largest deviation on the order of a few mN m^{-1} (which could be in the range of

experimental uncertainty) occurs when the model predicts phase change (flat surface tension profile). This could be due to the aforementioned non-first-ordrer behavior of actual surfactants. In addition, the model assumes perfect 1D-diffusion to a flat interface, whereas as in the tensiometer experiment, convection and Marangoni effects could be affecting the dynamic surface tension.

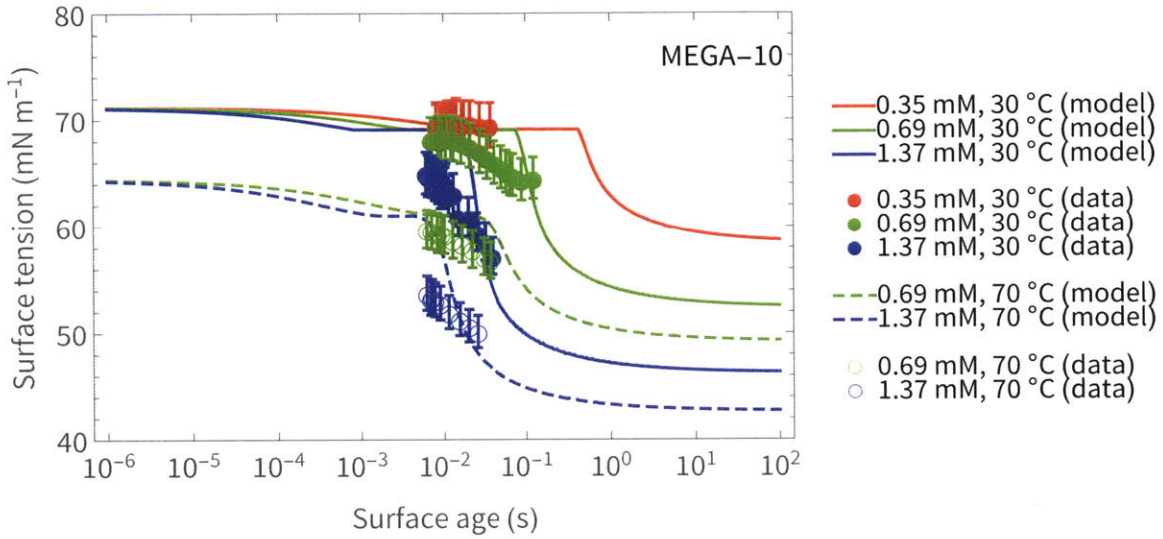

Figure 3-8: **Dynamic surface tension validation for MEGA-10.** Dynamic surface tension model (Eqs. 3.28 and 3.54) compared with own data obtained as described in Section 2.3.3.

Low-CMC ionic surfactant

For the low-CMC ionic surfactant 16TAB (CMC $\approx$ 1 mM), the model provides reasonable agreement with accuracy within a few mN m^{-1} across different concentrations and temperatures (see Figure 3-9). There is a slight tendency to under-predict the surface tension drop. This could be due to the fact that the Debye length becomes very large (on the order of tens of nm) at these concentrations and could be overestimating the effective monolayer thickness in Eq. 3.54.

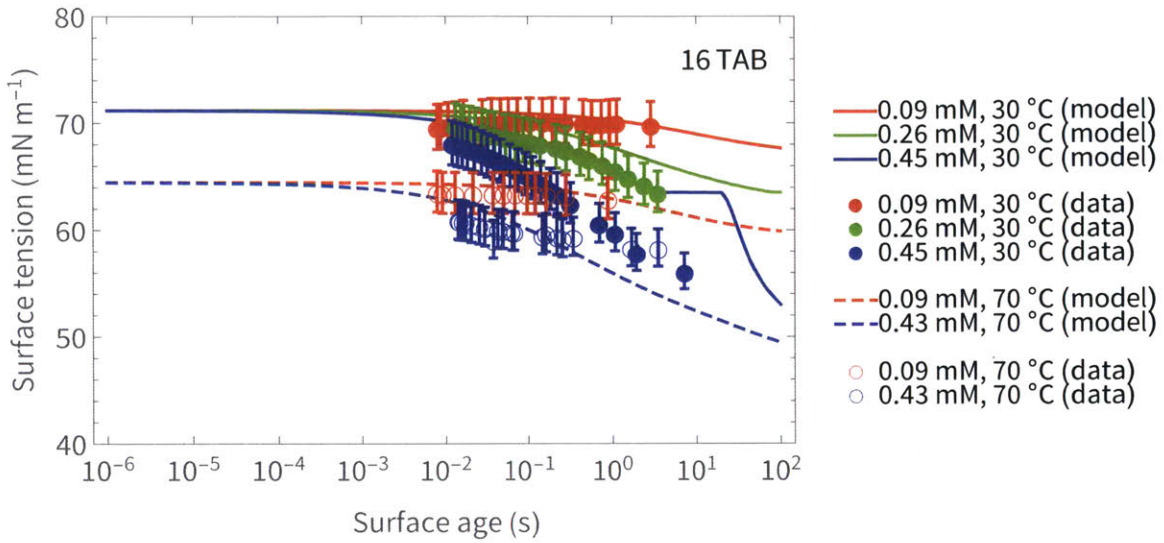

Figure 3-9: **Dynamic surface tension validation for 16TAB.** Data obtained as described in Section 2.3.3.

Medium-CMC ionic surfactant

For the medium-CMC ionic surfactant S12S (CMC $\approx$ 10 mM), the model provides remarkable accuracy for the very short timescale data provided by Owens (see Figure 3-10). Owens obtained measurements using the oscillating jet method [93] at two different temperatures.

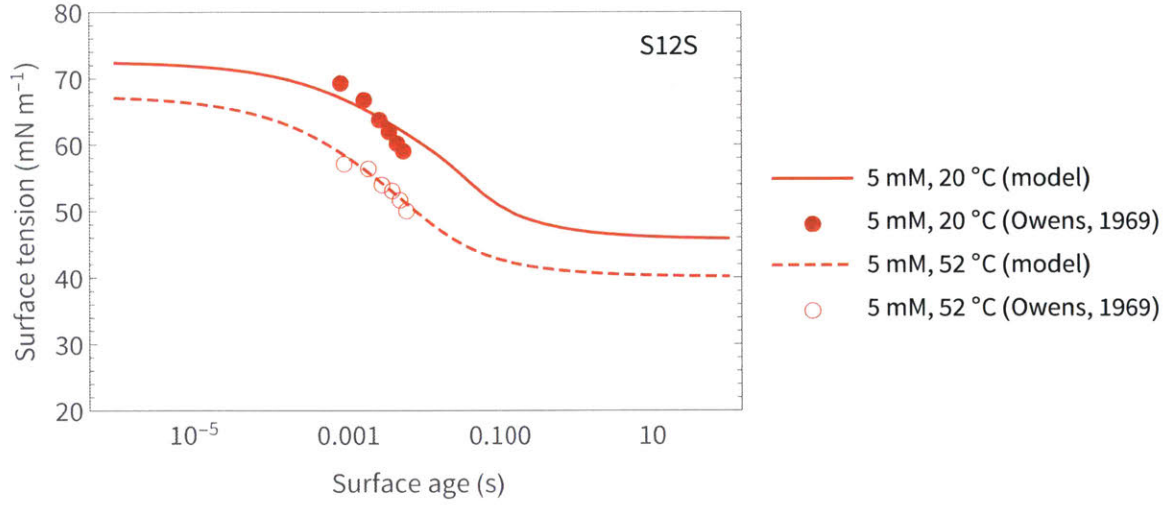

Figure 3-10: **Dynamic surface tension validation for S12S.** Data taken from Owens [93].

High-CMC ionic surfactant

For the high-CMC ionic surfactant 10TAB (CMC $\approx$ 50 mM), the model tends to overestimate the drop in surface tension up to approximately 10 mN m^{-1} (see Figure 3-11). This could due to the Debye length underestimating the effective monolayer length at these higher concentrations.

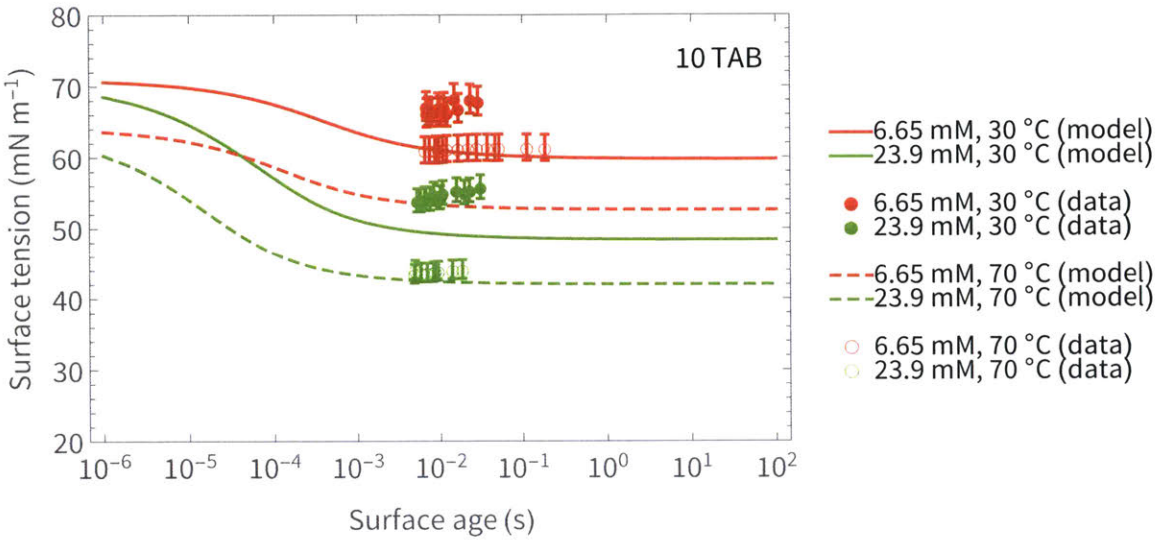

Figure 3-11: **Surface tension model validated with MEGA-10 for temperature and concentration dependence.** Data obtained as described in Section 2.3.3.

Summary of dynamic surface tension validation

Overall, the dynamic surface tension model has reasonable success at predicting dynamic surface tension. Better accuracy was found for non-ionic surfactants since the effective monolayer length does not have to be corrected with a Debye length. For ionic surfactants, better accuracy seems to occur at CMCs near 10 mM. Some of the difficulty in validating the model, which assumes perfect 1-D diffusion, is due to limitations of the bubble tensiometer measurement technique where flows around a growing bubble are involved.

3.8 Summary

In this Chapter, we present a model to predict equilibrium surface tension from molecular parameters that leverages progress made from previous studies. This model is based off a statistical mechanical partition function, from which the equation of state, adsorption isotherm, and suface tension isotherm can be obtained. The model has shown agreement with literature and our own experimental data. This equilibrium model was extended to a dynamic surface tension description using a modified Ward-Tordai equation. The results from the dynamic surface tension model, which is still ultimately based off of molecular parameters, has also shown agreement with literature and our own experimental data. The results from this Chapter will be used to determine bubble behavior and boiling performance in the following Chapter.

CHAPTER 4

BOILING ENHANCEMENT WITH SURFACTANTS

Bubble behavior dictates the heat transfer performance of boiling. Bubble behavior will be discussed in two parts: (1) nucleation which tends to affect superheat; (2) growth and departure which tend to affect heat flux. Accordingly, our analysis of heat transfer enhancement will be focused on horizontal (superheat) and vertical (heat flux) movement of the boiling curve. As mentioned previously, wetting properties (contact angle and surface tension) depend on surfactant type and concentration and alter bubble behavior. From Chapter 3, we are able to calculate equilibrium and dynamic liquid-vapor surface tension from molecular parameters. From Chapter 2, we are able to relate equilibrium liquid-vapor surface tension to solid-liquid surface tension and, subsequently, contact angle, using a generally observed experimental result. This gives us all the properties to calculate heat transfer performance as we will show in this Chapter. We will also provide recommendations on ideal surfactants for boiling.

4.1 Bubble nucleation

Our treatment of bubble nucleation will be based on entrapped vapor theory, which is not true heterogeneous nucleation where the initial surface is fully wetted as these would require exceptionally high superheats [94]. Instead, we treat bubbles as growing from vapor regions trapped in cavities, which we assume to be distributed at various sizes on the surface and with similar conical geometries [95]. Although this is an imperfect representation of the true cavity distribution on real surfaces, this approach has been used in the past with reasonable success [96].

4.1.1 Entrapped vapor theory

As mentioned in Chapter 1, a bubble that is entrapped within a cavity has a radius of curvature, R_b, which determines the pressure inside the bubble by the Young-Laplace equation (Eq. 1.4):

$$\Delta P = \frac{2\gamma_{lv}}{R_b}.$$

The radius of curvature, and subsequently the bubble pressure, will depend on the contact angle, cavity geometry, and the manner in which the bubble is entrapped. As such, there are several cavity nucleation models that will be discussed in this Section. Since the radius of curvature is usually positive, the pressure in the bubble should be higher than the surrounding liquid pressure, P_0.[1] This leads to the requirement of a superheat to nucleate the bubble. The amount of superheat required to activate evaporation can be approximated by the Clausius-Clapeyron relation (Eq. 1.5):

$$\frac{\Delta P}{\Delta T} \approx \left(\frac{dP}{dT}\right)_{sat} = \frac{h_{fg}}{T_{sat} v_{fg}}.$$

[1] Creating cavities that can sustain negative radii of curvature would theoretically allow for boiling below the boiling temperature.

Knowing that activation occurs when $P_b = P_{sat}$, and incorporating the Young-Laplace equation, the radius of curvature is related to the superheat by Eq. 1.6:

$$\Delta T = \frac{2\gamma_{lv} T_{sat} v_{fg}}{h_{fg} R_b}.$$

We will now discuss how to relate the radius of curvature to information about the cavity itself.

4.1.2 Cavity model

Hsu modeled a bubble sitting on a cavity mouth. The cavity mouth has a cavity radius, R_{cav} and a cavity angle, γ, which is the angle of the tangent to the mouth with respect to the horizontal [97]. In this treatment, the shape of the bubble can then be considered to be a spherical cap with an effective contact angle of $\gamma + \theta$; thus, the radius of curvature is

$$R_b = \csc(\gamma + \theta) R_{cav}. \tag{4.1}$$

Here, γ hypothetically can range from 0° (no cavity) to 90° (vertical cavity) to > 90° if the the cavity is re-entrant. However, since we are analyzing relatively plain, smooth surfaces, we can assume no reentrant cavities exist, which limits us to the $0° < \gamma < 90°$ range. For $\gamma = 70°$, Figure 4-1 illustrates how cavities of different cavity radii, R_{cav}, lead to different R_b. If contact angle were to increase for a given cavity, R_b increases and subsequently the required ΔT_{wall} to activate the site decreases. The required superheat to open a cavity can be determined by combining Eq. 4.1 with the Clausius-Clapeyron relation (Eq. 1.6):

$$\Delta T = \frac{2\gamma_{lv} T_{sat} v_{fg}}{h_{fg} R_{cav}} \sin(\gamma + \theta). \tag{4.2}$$

The Hsu cavity model, however, can lead to unphysical results. If we assume that cavities are roughly conical in geometry, which is a typical assumption [98], then

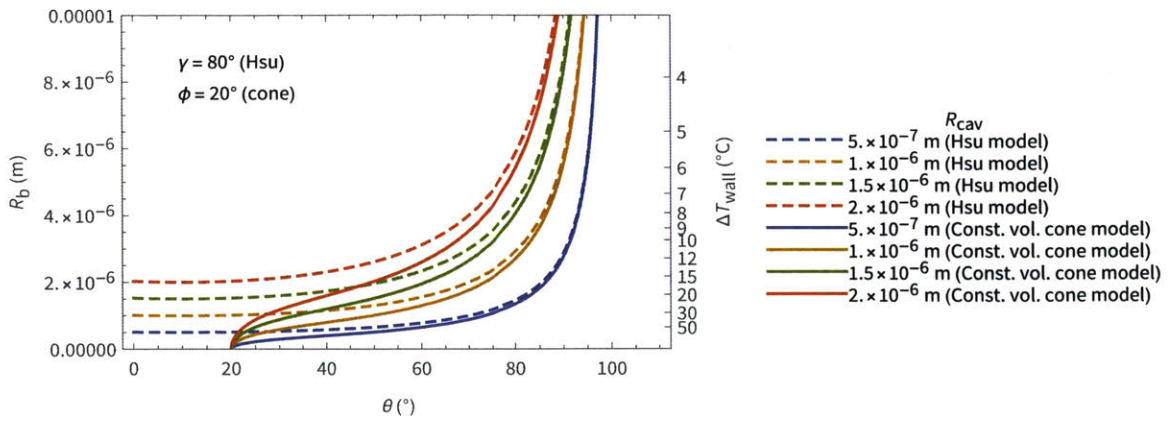

Figure 4-1: **Bubble radius of curvature, contact angle, and superheat for two different cavity models.**

geometric arguments can be made (Appendix C.1) that limit the minimum contact angle,

$$\theta_{\min} = \pi - 2\gamma \tag{4.3}$$

This is because, if the contact angle were below $\pi - 2\gamma$, liquid would completely wet the conical cavity. With this limitation, R_b monotonically increases with contact angle ($\theta_{\min} = 20°$ in Figure 4-1). However, bubbles can still exist below this limit with the Hsu cavity model as Figure 4-1 shows. To rectify this, we have developed a cavity model inspired by Lorenz [99] in which the volume inside a conical cavity is determined by the advancing liquid-vapor front (see Figure 1-3). In Lorenz' treatment, he assumed the volume at the moment the liquid-vapor interface was closed off by the opposite cone lip is constant. However, simplifications were made to obtain an approximate equation for R_b. In our treatment, we have found an exact mathematical expression for R_b without simplification. This was found by setting the volume of a sliced cone (Eq. C.10 in Appendix C.1), setting it equal to the volume of a cone with a spherical cap, and solving for R_b with the aid of Mathematica, a computer algebra system. The result is that

$$R_b = \frac{2^{2/3}\sqrt[3]{\cot\left(\frac{\phi}{2}\right)}\sqrt{\csc(\theta)\sin(\theta-\phi)}}{\sqrt[3]{\csc\left(\frac{\phi}{2}\right)(-3\cos(\theta-\phi)+\cos(3\theta-\phi)+6\cos(\theta))+8}}R_{cav} \tag{4.4}$$

where ϕ is the cone angle (the opening angle at the bottom of the cone). Lorenz' more approximate result, in comparison, tends to underpredict R_b at low contact angles and overpredict R_b at high contact angles. Plugging in Eq. 4.4 into the Clausius-Clapeyron relation gives

$$\Delta T = \frac{\sqrt[3]{2} v_{fg} \gamma_{lv} T_{sat} \sqrt[3]{\csc\left(\frac{\phi}{2}\right)(-3\cos(\theta-\phi)+\cos(3\theta-\phi)+6\cos(\theta))+8}}{R_{cav} h_{fg} \sqrt[3]{\cot\left(\frac{\phi}{2}\right)} \sqrt{\csc(\theta)\sin(\theta-\phi)}}. \quad (4.5)$$

Both the Hsu and constant volume cone model have the the upper bound on contact angle:

$$\theta_{max} = \pi - \gamma \quad (4.6)$$

as both approach infinite R_b at this point. Physically this can be interpreted as the point at which the bubble is no longer attached to the cavity wall, but pinned at the lip, allowing for large radii of curvature. While, in reality, a pinned bubble cannot attain an infinitely large radius since at some point gravity becomes important, the contact angles required for this condition are $> 90°$, which is not typical in boiling systems.

4.1.3 Cavity distribution

The cavity model described above only pertains to a single cavity that is axisymmetric. In reality, we should expect a variety of different types of cavity geometries and a distribution of size and mouth angles. However, mapping the micro-geometry of an entire surface would be challenging to accurately perform. But coupled with the fact that nucleation is most sensitive to R_{cav} and that there can be a distribution of cavity sizes that correlate with nucleation [100], it is reasonable to treat the surface as having self-similar cavities but with a range of sizes. Brown found that the number active nucleation sites, n, follows a power law distribution [100] with the smallest active cavity radius at a given wall superheat, which we know from Eq. 4.5.

Hence,

$$n(\Delta T_{\text{wall}}) \propto \left(\frac{1}{R_{\text{cav}}}\right)^m \tag{4.7}$$

where m is a parameter that describes how steep the distribution in cavity size is and depends on the surface (typically can range from 2 to 7). Assuming $R_{\text{cav}} \propto R_{\text{b}}$ (true for the cavity model as shown by Eq. 4.4), then applying the Clauius-Clapeyron model it is apparent that

$$n \propto T_{\text{wall}}^m \tag{4.8}$$

as Mikic and Rohsenow have shown [96].

4.2 Bubble growth

4.2.1 Original growth model

Once a bubble has nucleated, heat transfer will be dictated by how a bubble grows. The bubble growth model described here is based on the model (an analytical equation) first presented by Plesset and Zwick [101]. Our modifications to the model incorporate the effects of a non-spherical bubble and a thermal boundary layer. While several studies involving CFD simulation of a single bubble incorporating these effects have been performed in the past [102, 103, 104, 51, 105], an analytical expression describing bubble growth has not been presented. First, we must establish some bubble geometry terminology. R_{equiv} and D_{equiv} are the equivalent radius and diameter, respectively, if the bubble were to be treated as a perfect sphere so

$$R_{\text{equiv}} = D_{\text{equiv}}/2 = \left(\frac{3}{4\pi}V\right)^{1/3}; \tag{4.9}$$

hence, R_{equiv} and D_{equiv} will be used to describe the *volume* of the bubble. R_{b}, like before, is the radius of curvature of the bubble. In the context of a spherical bubble, we will simply use R since in this case $R = R_{\text{b}} = R_{\text{equiv}}$. Finally, R_{base} is the base radius of a bubble on a surface, i.e. the radius of the circle inscribed by the three-phase contact line.

As Mikic et al. have found [106], bubble growth can be described by two regimes. At short timescales, there is inertially dominated growth in which

$$R_{\text{equiv}} \propto t \tag{4.10}$$

and is described by the Rayleigh equation. At longer timescales, growth is heat diffusion dominated growth in which

$$R_{\text{equiv}} \propto \sqrt{t} \tag{4.11}$$

and is described by the Plesset-Zwick equation [101]. However, since the timescale at which this transition occurs is on the order of tens of μs whereas bubble departure times are typically two to three orders of magnitude higher, our model will use the Plesset and Zwick heat diffusion dominated growth approach.

Plesset and Zwick stated that the conductive heat transfer into and around a growing spherical bubble is equivalent to the latent heat times the mass change rate of the bubble. Thus, the following scaling relationship holds:

$$4\pi R^2 \frac{k_l \Delta T}{\sqrt{\alpha_l t}} \sim \rho_v h_{fg} \frac{dV}{dt} \tag{4.12}$$

where k_l is the thermal conductivity of the liquid and α_l is the thermal diffusivity of the liquid. For a sphere, $\frac{dV}{dt} = 4\pi R^2 \frac{dR}{dt}$; hence,

$$\frac{dR}{dt} \sim \frac{k_l \Delta T}{\rho_v h_{fg} \sqrt{\alpha_l t}} \tag{4.13}$$

and after integrating,

$$R(t) \sim 2\frac{k_l \Delta T}{\rho_v h_{fg} \sqrt{\alpha_l}} \sqrt{t}. \tag{4.14}$$

4.2.2 Modified growth model

Now let us consider an axisymmetric bubble but with an arbitrary profile. Also, as shown in Figure 4-2, we will consider a simple thermal boundary layer where the

liquid temperature linearly decreases from $T = T_{\text{wall}}$ at $z = 0$ (at the solid-liquid interface) to $T = T_{\text{sat}}$ at $z = \delta_T$ so

$$\Delta T = \Delta T_{\text{wall}}\left(1 - \frac{z}{\delta_T}\right) \tag{4.15}$$

where δ_T is the thermal boundary length. We will also assume that the temperature of the vapor bubble is at T_{sat} which is reasonable since the temperature gradient required to change phase would be very high. Much of the temperature variation occurs on the liquid side outside the bubble over a very thin layer with thickness $\sqrt{\alpha_l t}$ [101]. We can therefore come up with the scaling

$$\int_{A_q} \frac{k_l (T(z) - T_{\text{sat}})}{\sqrt{\alpha_l t}} dA \sim \frac{\pi}{2} D_{\text{equiv}}^2 \rho_v h_{fg} \frac{dD_{\text{equiv}}}{dt} \tag{4.16}$$

where dA is a differential bubble surface area at a height z and A_q is the surface area where heat transfer occurs (any bubble surface that is within the thermal boundary layer). Knowing the surface area of the bubble as a function of the distance from the wall will allow for calculation of the integral term. We will come back to this equation once we determine an expression for the surface area, which will depend on contact area and the thermal boundary layer thickness.

Evaluating the Young-Laplace equation for a pendant bubble (Eqs. 2.2–2.4) allows for numerical calculation of a static bubble profile in the presence of gravity. Though not perfectly representative of the situation in boiling since convection is involved, bubble geometry in boiling is more qualitatively similar to pendant geometries as opposed to spherical cap geometries due to the importance of gravity. From analysis of numerical studies on bubble growth [102, 103, 104, 51, 105], we have found that using the Young-Laplace numerical solution to calculate D_{base} closely follows the actual D_{base} for much of the growth period as shown in Figure 4-3. Thus, based on quantitative and qualitative resemblance, and for the purpose of simpler analysis, the static pendant geometry is considered.

For a numerically solved pendant bubble, the total surface area, A_{tot}, was found

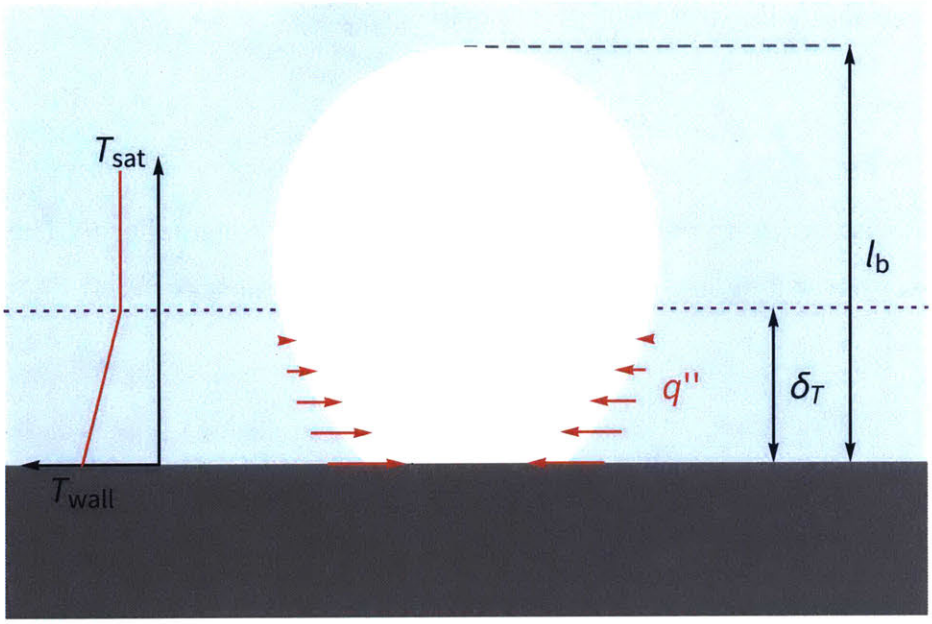

Figure 4-2: **Heat transfer around a growing bubble within a thermal boundary layer.** A bubble with height l_b having a pendant shape grows as a result of lateral heat conduction, q'', at its bottom. The heat flux is larger near the surface and decreases to zero at the thermal boundary layer height, δ_T. The temperature profile in the thermal boundary layer is linear.

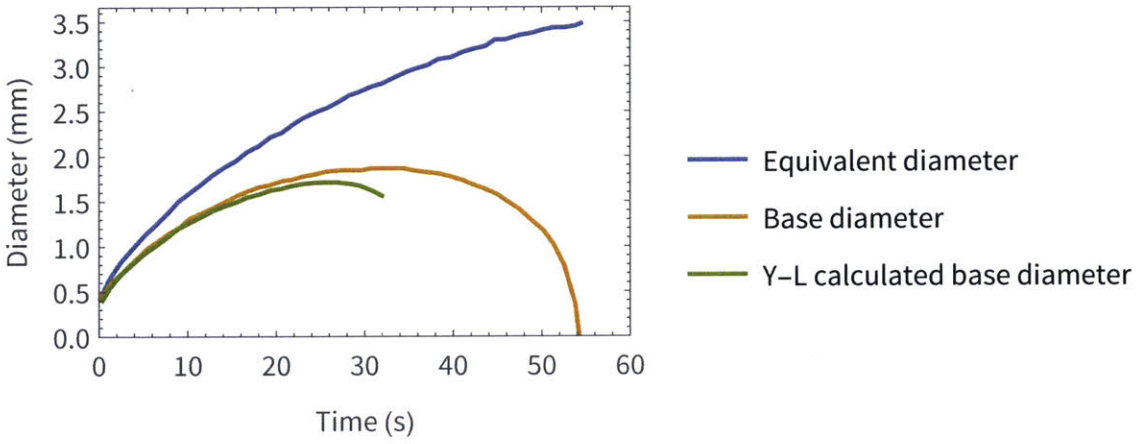

Figure 4-3: **Comparison of Young-Laplace calculated base diameter to actual base diameter.** Data of bubble growth with $\Delta T_{wall} = 10\,°C$ and $\theta = 54°$ from a numerical simulation by Mukherjee and Dhir [104]. The orange line shows the actual base diameter while the green line shows a calculated base diameter based off the actual equivalent diameter in blue. This was calculated using a numerical solution to the Young-Laplace equation for a static pendant bubble.

to be approximately linear with R^2_{equiv}. Specifically,

$$A_{\text{tot}} = ((\pi - 2.4)\cos\theta + 2.4)\left(2R_{\text{equiv}}\right)^2 \tag{4.17}$$

to within 5 % accuracy up to $\theta = 90°$ with better accuracy for smaller θ. The partial surface area up to a height z, $A(z)$ was also found to be almost perfectly linear. That is,

$$A(z) \propto z \tag{4.18}$$

To approximate the height of the bubble, l_{b}, the approximation

$$l_{\text{b}} = 2R_{\text{equiv}}\cos\frac{\theta}{2} \tag{4.19}$$

was found to be accurate within 4 % of the numerically determined height. With Eq. 4.19 and 4.17, it is possible to compute the integral in Eq. 4.16. First, we change the differential element dA to $\frac{dA}{dz}dz$. From Eq. 4.18, $\frac{dA}{dz}$ = constant; therefore, taking into account Eq. 4.19 and 4.17,

$$\frac{dA}{dz} = \text{constant} = \frac{\Delta A}{\Delta z} = \frac{((\pi - 2.4)\cos\theta + 2.4)}{\cos\frac{\theta}{2}}\left(2R_{\text{equiv}}\right). \tag{4.20}$$

Now, Eq. 4.16 can be expressed as

$$\int_0^h \frac{k_{\text{l}}(T(z) - T_{\text{sat}})}{\sqrt{\alpha_{\text{l}} t}} \frac{(\pi - 2.4)\cos\theta + 2.4}{\cos\frac{\theta}{2}}\left(2R_{\text{equiv}}\right)dz \sim 4\pi R^2_{\text{equiv}}\rho_{\text{v}}h_{\text{fg}}\frac{dR_{\text{equiv}}}{dt} \tag{4.21}$$

where h is the maximum height we integrate up to ($h = \delta_T$ if $l_{\text{b}} > \delta_T$ and $h = l_{\text{b}}$ if $l_{\text{b}} < \delta_T$). We further simplify this to

$$C_b \int_0^h b\frac{R_{\text{equiv}}\Delta T(z)}{t^{1/2}}dz = R^2_{\text{equiv}}\frac{dR_{\text{equiv}}}{dt} \tag{4.22}$$

by introducing a growth rate scaling factor C_b and using the substitution

$$b = \frac{k_l((\pi - 2.4)\cos\theta + 2.4)\sec\frac{\theta}{2}}{2\pi h_{fg}\rho_v \alpha_l^{1/2}}. \tag{4.23}$$

For the thermal boundary layer, using a natural convection boundary layer correlation [107] leads to

$$\delta_T = C_\delta \left(\frac{\nu_l \alpha_l}{g\beta_l \Delta T_{wall}}\right)^{1/3} \tag{4.24}$$

where C_δ is a boundary length scaling factor, ν_l is kinematic viscosity, and β_l is the liquid thermal expansion coefficient [K^{-1}]. If contact angle is constant with time,[2] then combining Eqs. 4.15, 4.23, and 4.24 into Eq. 4.22 allows for solving the bubble growth over time. The result is

$$R_{equiv}(t) = \begin{cases} \frac{2\delta_T}{c}\left(1 - \exp\left(-\frac{C_b b c^2 \Delta T_{wall}\sqrt{t}}{\delta_T}\right)\right) & 0 \le t < t_\delta \\ \sqrt{2}\sqrt{C_b b \delta_T \Delta T_{wall}\sqrt{t} - \frac{\delta^2(\ln 4 - 1)}{2c^2}} & t \ge t_\delta \end{cases} \tag{4.25}$$

where

$$c = 2\cos\frac{\theta}{2}, \tag{4.26}$$

$$t_\delta = \left(\frac{\delta_T \ln 2}{C_b b c^2 \Delta T_{wall}}\right)^2. \tag{4.27}$$

When $t < t_\delta$, the height of the bubble, l_b is less than the thermal boundary thickness, δ_T, and when $t > t_\delta$, $l_b > \delta_T$. Here, Eq. 4.25 has the behavior of $t^{1/2}$ growth when the bubble is much smaller than the boundary length (same result as Plesset and Zwick where a uniform superheating is assumed) and $t^{1/4}$ growth when the bubble is larger than the boundary length (which agrees with a simple scaling analysis).

Using data from several studies [102, 104, 105], we have found that the follow-

[2]Small changes in contact angle during growth do not significantly alter growth behavior as Mukherjee and Kandlikar have shown [104]. Thus, a constant θ approximation is reasonable.

ing values for the scaling factors are appropriate.

$$C_b = 0.5 \tag{4.28}$$

$$C_\delta = 35.7 \tag{4.29}$$

Validation with this data can be found in Section 4.3.3.

4.2.3 Growth model with time-dependent contact angle

The previous result, though useful for validation with previous studies, is not applicable in the presence of surfactants since dynamic, time-dependent effects would occur. Thus, we will extend the model to conditions where the contact angle is also a function of time. Using the Young equation,

$$\theta(t) = \arccos\left(\frac{\gamma_{\mathrm{lv},0}\cos\theta_{\mathrm{init}}}{\gamma_{\mathrm{lv}}(t)}\right) \tag{4.30}$$

where $\gamma_{\mathrm{lv},0}\cos\theta_{\mathrm{i}}$ is $\gamma_{\mathrm{sv}} - \gamma_{\mathrm{sl}}$ for a fully equilibrated solid-liquid interface, θ_{init} is the initial ($t = 0$) contact angle of bubble on a fully equilibrated solid-liquid interface (which we introduced in Eq. 2.8), and $\gamma_{\mathrm{lv}}(t)$ is the dynamic surface tension. Thus, evaluating Eq. 3.54 and plugging into the equation of state (Eq. 3.28) using the method described in Chapter 3 allows for the calculation of contact angle over time.

Solving Eq. 4.22 when θ is a function of time yields

$$R_{\mathrm{equiv}}(t) = \exp\left(-\int_0^t \frac{C_b b(\tau_1)(c(\tau_1))^2 \Delta T_{\mathrm{wall}}}{2\delta_T\sqrt{\tau_1}} d\tau_1\right) \times \left(\int_0^t \frac{\exp\left(\int_0^{\tau_2} \frac{C_b b(\tau_1)(c(\tau_1))^2 \Delta T_{\mathrm{wall}}}{2\delta_T\sqrt{\tau_1}} d\tau_1\right) C_b b(\tau_2) c(\tau_2) \Delta T_{\mathrm{wall}}}{\sqrt{\tau_2}} d\tau_2\right) \tag{4.31}$$

for $0 \leq t < t_\delta$ and

$$R_{\mathrm{equiv}}(t) = \sqrt{2}\sqrt{\int_0^t \frac{\delta_T C_b b(\tau_1)\Delta T_{\mathrm{wall}}}{2\sqrt{\tau_1}} d\tau_1 + K_\delta} \tag{4.32}$$

for $t \geq t_\delta$. Here, K_δ is a constant that ensures continuity between Eqs. 4.31 and 4.32:

$$K_\delta = \frac{\left(R_{\text{equiv}}(t_\delta)\right)^2}{2} - \int_0^t \frac{\delta_T C_b b(\tau_1)\Delta T_{\text{wall}}}{2\sqrt{\tau_1}} d\tau_1 \tag{4.33}$$

To evaluate these equations, Eq. 4.31 is calculated by numerical integration. A root solving algorithm finds when Eq. 4.31 is equal to $\frac{\delta_T}{c}$ (when the height of the bubble is equal to the thermal boundary layer thickness), setting a value for t_δ. Then, 4.32 can be calculated numerically via integration.

4.3 Bubble departure

4.3.1 Background

In the previous Section, we discussed bubble growth; however, in order to calculate the heat transfer on a single nucleation site, the departure conditions must be known. For a single nucleation site, the heat transfer [W] is

$$q_{\text{single}} = \frac{\frac{4}{3}\pi R^3_{\text{equiv,depart}} \rho_v h_{fg}}{t_{\text{depart}}}. \tag{4.34}$$

Multiplying this by the nucleation density, n [m^{-2}], should give the heat flux, q'' [W m^{-2}]:

$$q'' = n q_{\text{single}}. \tag{4.35}$$

This general statement (Eq. 4.35) is often referred to as the Mikic-Rohsenow model, although Mikic and Rohsenow used a semi-infinite conduction term to define q_{single} [96] whereas we are defining q_{single} from an energy balance. The assumption here is that bubbles behave as if they are isolated from each other, hence the proportionality to nucleation density. In reality, when nucleation densities are very high, the proximity or coalescence of bubbles should alter the heat transfer. That is, q_{single} itself becomes a function of nucleation density.

Many departure criteria exist in the literature and are often determined by cor-

relating relevant properties to observed departure diameters [108]. Fritz developed a simple expression based on a force balance of surface tension and buoyancy that depends on contact angle [109]. Later, Cole came up with an expression depends on both contact angle and wall superheat [108]. However, none of the existing departure criteria can deal with contact angle and surface tension that are changing with time. In our treatment of bubble departure, we have taken a fundamentally different approach: we track the movement of the three-phase contact line with time based on our growth model and make assumptions about momentum forces to determine the point at which bubble departure occurs.

4.3.2 Departure model description

First, we have come up with a simplified expression for the base diameter. Using the Young-Laplace numerical solution to the pendant bubble, the base diameter of a bubble, D_{base}, can be approximated by a cubic equation:

$$D_{\text{base}} = 0.795908\theta D_{\text{equiv}} - \frac{12\,034.8\,/\text{m}^2 D_{\text{equiv}}^3 (\cos(2\theta)-1)}{\theta^3} \tag{4.36}$$

where θ is radians. A comparison between this model and the exact Young-Laplace solution is shown in Figure 4-4.

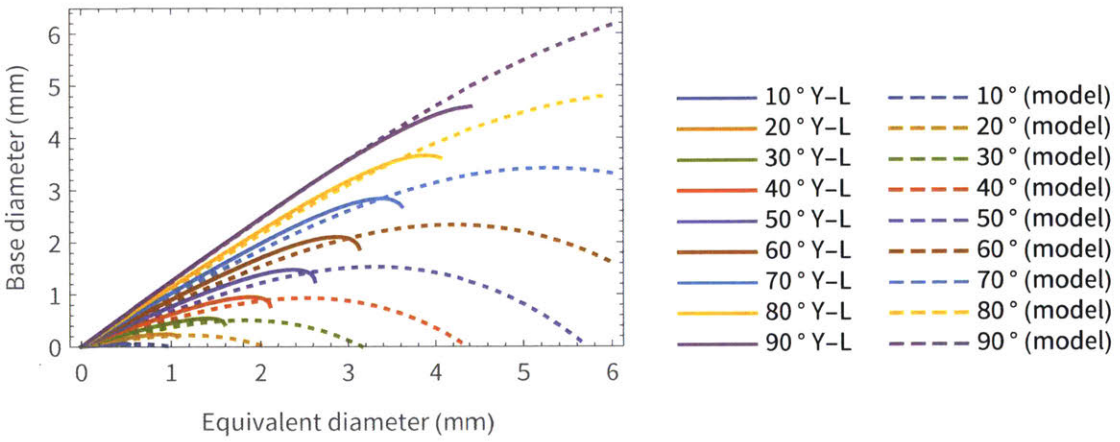

Figure 4-4: **Base diameter versus equivalent diameter for pendant bubbles of different contact angles.** Solid lines represent exact solutions to the Young-Laplace equation calculated numerically. Dashed lines are from Eq. 4.36

Then, from observations we have made from numerical simulations of bubble growth and departure, we have found that departure can be described as a constant momentum force closing in at the base of the bubble. This constant momentum force is related to natural convection as we will show later. To illustrate this idea, we can observe the base diameter velocity as a function of time for a bubble simulated by Mukherjee and Kandlikar [104] as shown in Figure 4-5. Initially, the base diameter velocity is high and positive as the bubble grows rapidly. However, the rate at which this radial velocity changes is changing (inward radial acceleration decreases). At some point, the radial velocity of the contact line decreases linearly with time (constant inward radial acceleration). This suggests that some constant departure momentum force is responsible for the closing of the base.

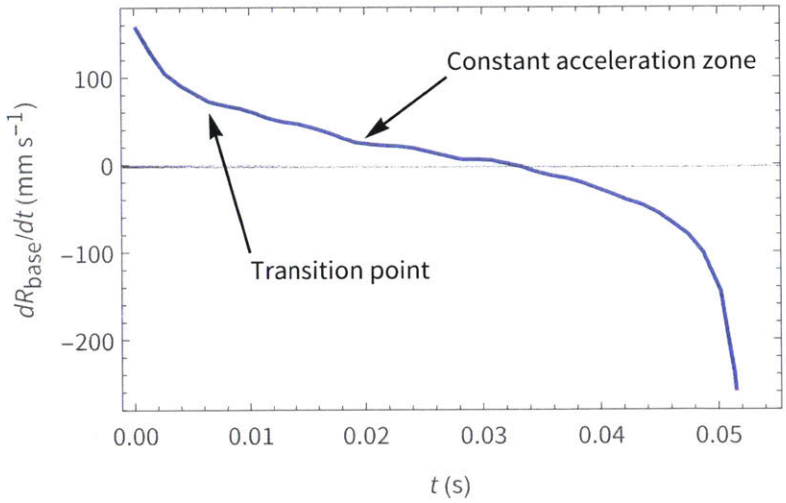

Figure 4-5: **Base diameter velocity shows a transition to a constant acceleration zone.** Data of bubble growth and departure with $\Delta T_{wall} = 10\,°C$ and $\theta = 54°$ from a numerical simulation by Mukherjee and Dhir [104] shows the base diameter velocity transitioning to a constant acceleration zone.

However, in the presence of surfactants where contact angle and surface tension is not constant, constant acceleration may not be observed even if there is a constant departure momentum force. To estimate how acceleration would scale as a function of contact angle and surface tension, let us consider a force balance of a fluid element on the contact line. Although fluid momentum above the contact line is ultimately driving the movement, Newton's second law must still be satisfied in terms of surface

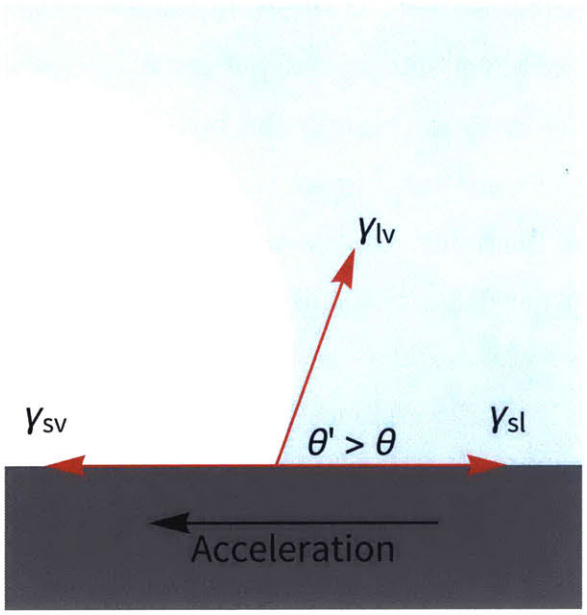

Figure 4-6: **Line-force acceleration where θ' is the dynamic contact angle.** When $\theta' > \theta$, horizontal surface tension forces are not balanced and there is a resultant acceleration inward due to Newton's second law.

forces at the contact line (Figure 4-6). We should expect that the acceleration at the contact line, a, should scale with the difference in surface tensions:

$$a \sim \underbrace{(\gamma_{sv} - \gamma_{sl})}_{\gamma_{lv}\cos\theta} - \gamma_{lv}\cos\theta' \tag{4.37}$$

where θ is the *equilibrium* contact angle, and θ' is the *dynamic* contact angle (Figure 4-6), which must be different from the equilibrium value otherwise movement does not occur. Using the substitution $\theta' = \theta + \delta\theta$ where $\delta\theta$ is assumed to take a small value,

$$\begin{aligned} a &\sim \gamma_{lv}[\cos\theta - \cos(\theta + \delta\theta)], \\ &\sim \gamma_{lv}[\cos\theta - (\cos\theta\cos\delta\theta - \sin\theta\sin\delta\theta)], \\ &\sim \gamma_{lv}\left[\cos\theta\underbrace{(1-\cos\delta\theta)}_{\text{small}} + \sin\theta\sin\delta\theta\right]. \end{aligned}$$

Hence,

$$a \sim \gamma_{lv} \sin\theta. \tag{4.38}$$

Therefore, once it is known when the bubble response transitions to a constant momentum force regime, the acceleration can be scaled according to contact angle and surface tension.

To determine when a transition, $D_{equiv,trans}$, to a constant momentum force regime occurs, let us first consider a "natural" departure diameter. Given a Young-Laplace pendant bubble profile (see Figure 4-7a), there is a minimum in tangent angle[3] (see Figure 4-7a) which corresponds to an inflection point in the bubble profile. It is convenient to use the bubble truncated at this point as its departure volume since there can be multiple contact angles for a single bubble shape profile beyond it. We will refer to a bubble truncated at this inflection point as having an equivalent diameter of $D_{equiv,inflect}$. An accurate approximation for $D_{equiv,inflect}$ is given by

$$D_{equiv,inflect} = \left(3.015\,49 \times 10^{-3}\,\mathrm{m}\right)\theta \tag{4.39}$$

where θ is in radians.

Physically, it works out that a bubble at $D_{equiv,inflect}$ has a buoyancy force that is equivalent to half the surface tension retaining force ($\pi D_{base}\gamma_{lv}\sin\theta$). Remarkably, using the Young-Laplace inflection point criterion has extremely good agreement with the Fritz correlation [109] as shown in Figure 4-8. In comparison, using a spherical cap force balance geometry can significantly overestimate the the departure diameter.[4] Thus, there is a physical basis for using $D_{equiv,inflect}$ and can be used as a first approximation for $D_{equiv,trans}$

However, there is a significant limitation with the above criteria in that the dependency on superheat is not captured. As we showed before, the closing of the bubble base can be explained by a momentum force. Thus, we postulate that $D_{equiv,trans}$ should scale with an effective "bulk" natural convection velocity in addition to the

[3]For a bubble truncated at a plane z, the tangent angle is equivalent to the contact angle.

[4]Nam, however, has shown that spherical cap based criterion could be reasonable for very low contact angles [105].

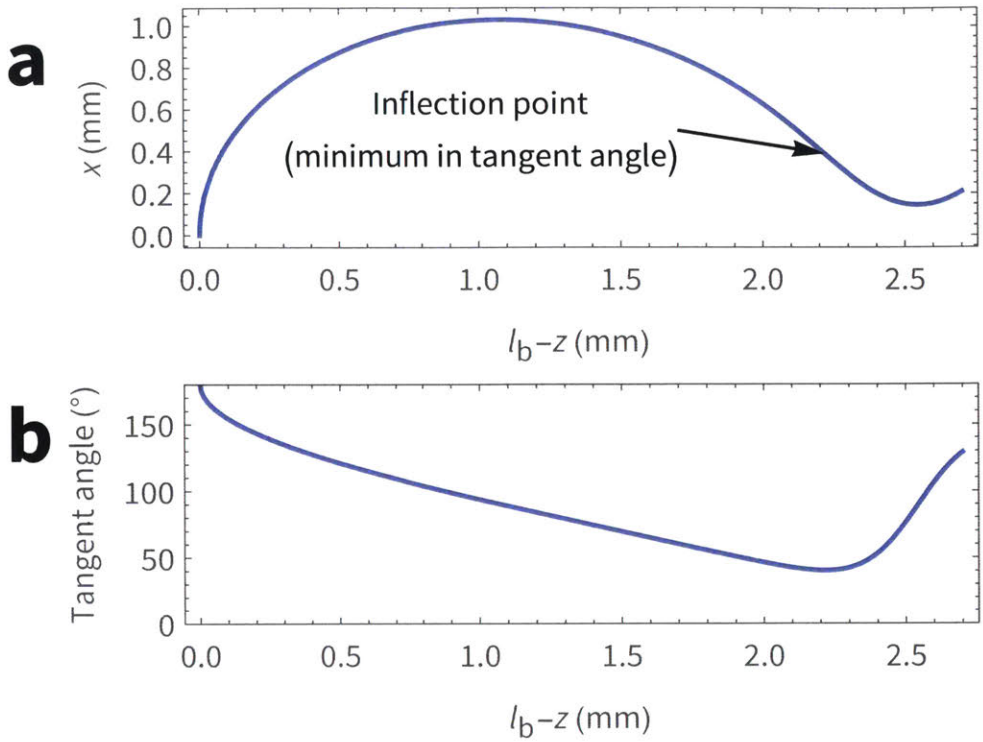

Figure 4-7: **Pendant bubble profile and its inflection point.** (a) A numerically resolved pendant bubble profile showing its inflection point, which is a minimum in the (b) tangent angle.

inflection equivalent diameter:

$$D_{\text{equiv,trans}} \propto v_{\text{bulk}} D_{\text{equiv,inflect}}. \tag{4.40}$$

This velocity is the basis for an inward force from the bulk liquid that ultimately causes the bubble to pinch off at the base (Figure 4-9). Velocity can be related to the bulk momentum boundary layer by

$$\delta_T = \text{Pr}^{-1/3} \delta_v \tag{4.41}$$

where Pr is the Prandtl number. The bulk momentum boundary layer can then be related to velocity by using laminar boundary layer theory where

$$\delta_v \propto \frac{L_c}{\sqrt{\text{Re}}} \tag{4.42}$$

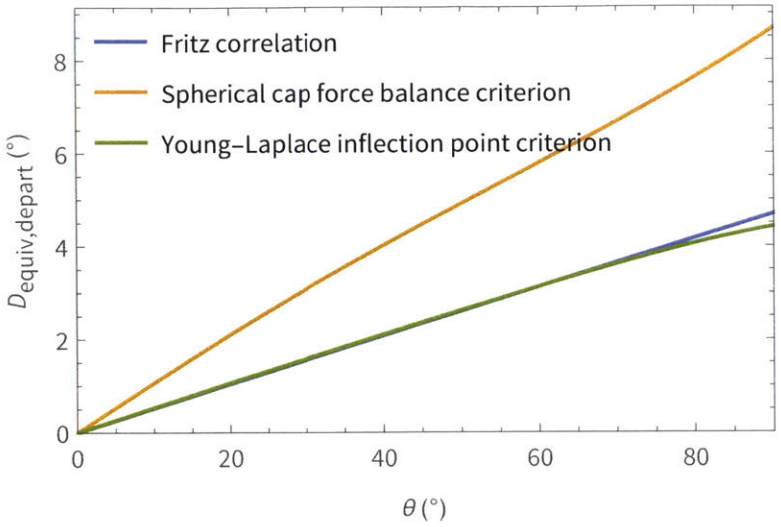

Figure 4-8: **Similarity of using Y-L inflection point equivalent diameter to the Fritz departure correlation.** A static force balance criterion based on a spherical bubble overpredicts the departure size compared to the Fritz correlation [109] while using the equivalent diameter of a static pendant bubble truncated at the inflection point is in close agreement.

where L_c is a natural convection lengthscale and Re is the Reynolds number. Thus,

$$v_{\text{bulk}} \propto \frac{1}{\delta_T^2} \tag{4.43}$$

and plugging in Eq. 4.24 reveals that

$$v_{\text{bulk}} \propto \Delta T_{\text{wall}}^{2/3}. \tag{4.44}$$

Using the above relations offers good agreement with numerical studies for contact angles above $\sim 25°$ but underestimates departure at low contact angles. At low contact angles the size of the bubble can be smaller than the bulk momentum boundary layer, which would minimize the importance of bulk momentum flow and emphasize the importance of surface tension driven flow. To account for this, we postulate that two components of the momentum departure force exist: v_{bulk} and v_γ (surface tension and evaporation driven velocity as shown in Figure 4-9). We assume the surface tension driven flow should scale with the ratio of the momentum boundary to the bubble height (we use the height at the inflection point as a

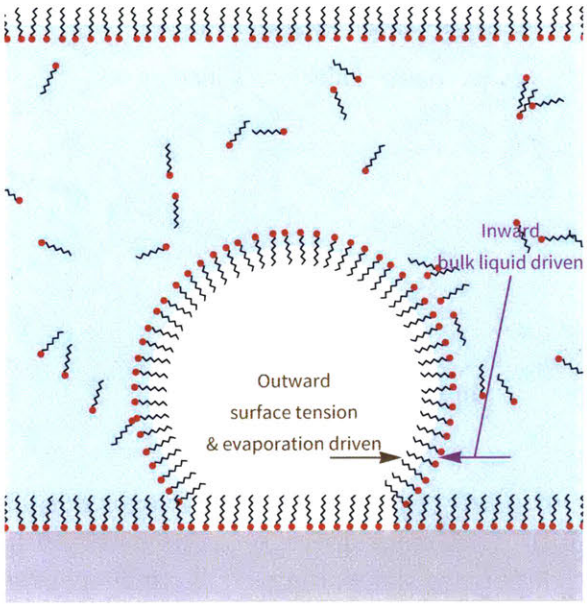

Figure 4-9: **Inward and outward forces at the base of a bubble.** Inward forces are caused by currents in the bulk liquid (natural convection) while outward forces are caused by suface tension and evaporation.

characteristic value for given contact angle):

$$v_\gamma \propto \frac{\delta_v}{l_{\text{b,inflect}}} v_{\text{bulk}}. \tag{4.45}$$

So, combining surface tension and bulk flow momentum forces, we come up with a correlation for the transition equivalent diameter as

$$\begin{aligned} D_{\text{equiv,trans}} &\propto \left(v_{\text{bulk}} + v_\gamma\right) D_{\text{equiv,inflect}} \\ &\propto \left(1 + C_\gamma \frac{\delta_v}{l_{\text{b,inflect}}}\right) v_{\text{bulk}} D_{\text{equiv,inflect}} \\ D_{\text{equiv,trans}} &= C_v \left(1 + C_\gamma \frac{\text{Pr}^{-1/3} C_\delta \left(\frac{\nu_l \alpha_l}{g \beta_l \Delta T_{\text{wall}}}\right)^{1/3}}{D_{\text{equiv,inflect}} \cos\frac{\theta}{2}}\right) \frac{D_{\text{equiv,inflect}}}{\Delta T_{\text{wall}}^{2/3}} \end{aligned} \tag{4.46}$$

where the scaling factor values of of $C_v = 0.116\,504\,\text{m}\,\text{K}^{-2/3}$ and $C_\gamma = 0.261684$ offer good agreement with literature data as will be shown in the 4.3.3.

4.3.3 Numerical evaluation and validation

To evaluate departure behavior, development of D_{base} over time is calculate using Eq. 4.36 and D_{equiv} solved from Eq. 4.22. This continues until $D_{equiv} = D_{equiv,trans}$ defined by Eq. 4.46. At this point (the moment of transition when the departure momentum force becomes important) the acceleration, a, is calculated by differentiating D_{base} with time. After transition, a is continuously scaled according to Eq. 4.38 by taking into account dynamic surface tension and time-dependent contact angle. By integrating a with time, the post-transition D_{base} is calculated. When $D_{base} = 0$, the bubble is considered departed and the $D_{equiv,depart}$ and t_{depart} are recorded. Some results of this numerical procedure are shown and validated with literature data in Figure 4-10. In addition, the modeled departure diameter and time as functions of superheat at different contact angles are presented in Figure 4-11.

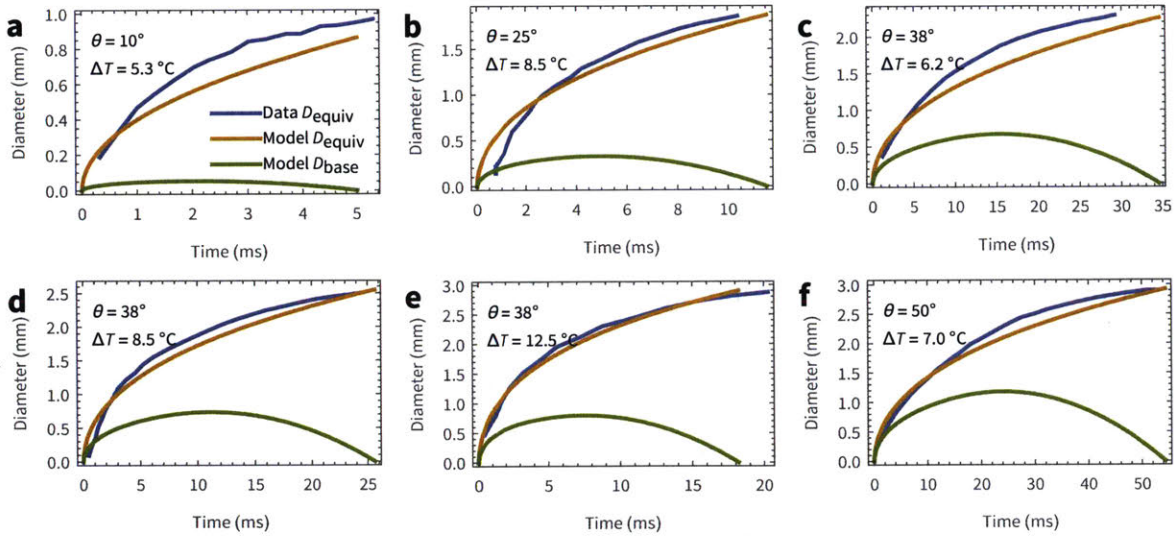

Figure 4-10: **Validation of bubble growth and departure.** Good agreement between model and data are shown for (a) ($\theta = 10°, \Delta T = 5.3\,°C$) [105], (b) ($\theta = 25°, \Delta T = 8.5\,°C$) [102], (c) ($\theta = 38°, \Delta T = 6.2\,°C$) [102], (d) ($\theta = 38°, \Delta T = 8.5\,°C$) [102], (e) ($\theta = 38°, \Delta T = 12.5\,°C$) [102], and (f) ($\theta = 50°, \Delta T = 7.0\,°C$) [102].

There is very good agreement in growth profiles as well as departure points across a range of contact angles and and superheats (Figure 4-11). Using the Plesset and Zwick $t^{1/2}$ dependency model rather than our growth model would have resulted in an overestimation of the departure volume. The exact functional depen-

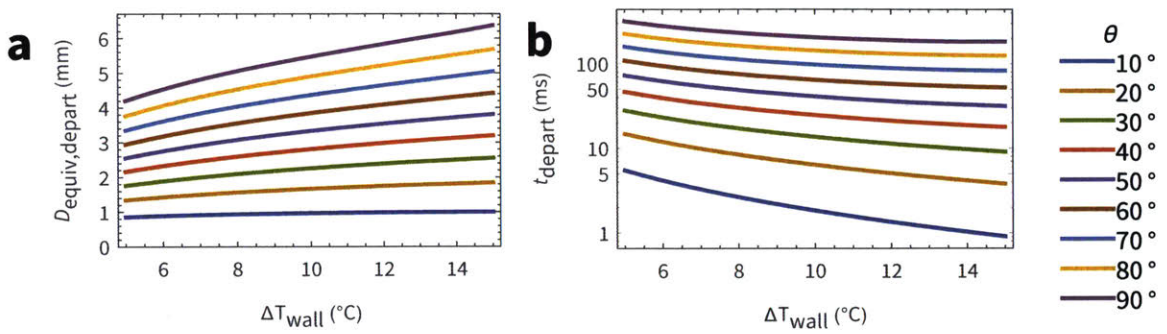

Figure 4-11: **Bubble departure model results.** (a) Departure size is shown as a function of superheat and contact angle. (b) Departure time is also shown as a function of superheat and contact angle.

dence of departure size and time is shown in Figure 4-11.

4.4 Shifting the boiling curve

Using the methodology to calculate $D_{\text{equiv,depart}}$ and t_{depart} for time varying contact angle and surface tension described in the previous Section, the thermodynamic surface tension model from Chapter 3, along with the Clausius-Clapeyron relation and the cavity model (Eq. 4.5), it is possible to calculate the shift in a boiling curve as a function of molecular parameters. The following procedure is taken to do so.

1. A reference DI water boiling curve is assumed. From this reference boiling curve, the inverse of Eq. 4.5,

$$R_{\text{cav}} = \frac{\sqrt[3]{2} v_{\text{fg}} \gamma_{\text{lv}} T_{\text{sat}} \sqrt[3]{\csc\left(\frac{\phi}{2}\right)(-3\cos(\theta-\phi)+\cos(3\theta-\phi)+6\cos(\theta))+8}}{\Delta T h_{\text{fg}} \sqrt[3]{\cot\left(\frac{\phi}{2}\right)} \sqrt{\csc(\theta)\sin(\theta-\phi)}}, \tag{4.47}$$

is applied to each data point (assuming pure water properties) such that a mapping of q''_{ref} to R_{cav} is created. The contact angle is assumed to be that of pure water on a surface with no surfactants. Physically, this represents the total heat flux as a function of the smallest cavity diameter opened. When surfactants are added, we assume the distribution of nucleation sites does not change. Instead, only the superheat at which each nucleation site opens changes.

2. The superheat for the surfactant boiling curve is calculated by taking the R_{cav} values from step 1 and inputting it into Eq. 4.5,

$$\Delta T = \frac{\sqrt[3]{2}\nu_{fg}\gamma_{lv}T_{sat}\sqrt[3]{\csc\left(\frac{\phi}{2}\right)(-3\cos(\theta-\phi)+\cos(3\theta-\phi)+6\cos(\theta))+8}}{R_{cav}h_{fg}\sqrt[3]{\cot\left(\frac{\phi}{2}\right)}\sqrt{\csc(\theta)\sin(\theta-\phi)}},$$

where properties of the surfactant are applied here. The contact angle used here is the time-dependent contact angle (Eq. 4.30) evaluated at some nucleation timescale (taken to be 1 ms). This gives an "effective, nucleation-timescale θ_{init}" since in reality a bubble does not start growing instantaneously at $t = 0$. This gives a mapping of q''_{ref} to $\Delta T_{wall,surf}$, i.e. a horizontal shift in the boiling curve as shown in Figure 4-12.

3. Finally, using the single-site heat transfer principle (Eq. 4.34), the heat transfer for surfactants can be calculated:

$$q''_{surf} = \frac{\frac{D^3_{equiv,depart,surf}}{t_{depart,surf}}}{\frac{D^3_{equiv,depart,ref}}{t_{depart,ref}}} q''_{ref} \tag{4.48}$$

which shifts the boiling curve vertically as shown in Figure 4-12.

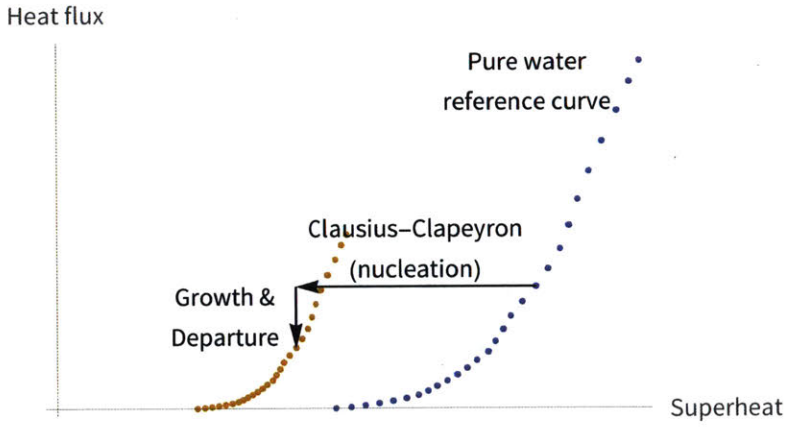

Figure 4-12: **Boiling curve shift procedure.** A horizontal shift is applied due to changes in nucleation behavior and the Clausius-Clapeyron relation. A vertical shift occurs due to changes in bubble growth and departure behavior.

4.5 Experimental validation

In this Section we will refer to Figure 4-13, Figure 4-14, and Figure 4-15. In these figures, the left most plot is actual experimental boiling curves for the surfactant of interest at several chosen concentrations. The middle plot shows the modeled boiling curves based on the pure water curve using the procedure from the previous Section and at the same concentrations. The right most plot shows the superheat as a function of concentration at a $20\,\mathrm{W\,cm^{-2}}$ (green lines in boiling curve plots). For all tests, the contact angle was assumed to be 30° and the cone angle was assumed to be 20°. For the modeled boiling curves, there is a tendency for the boiling curve to shorten as it shifts left. This is a natural consequence of rescaling (Eq. 4.48) where the heat transfer is vertically shifted due to different departure behavior with surfactants. It does not mean that we expect nucleate boiling to end and hit CHF at the top of the shortened boiling curves; it is a result of using only part of the entire boiling curve for water. If the entire water boiling curve were known, then the entire surfactant boiling curve could potentially be modeled. Thus, even though boiling curves may seem to end before the green line of $20\,\mathrm{W\,cm^{-2}}$, we have extrapolated the curve to obtain the expected superheat.

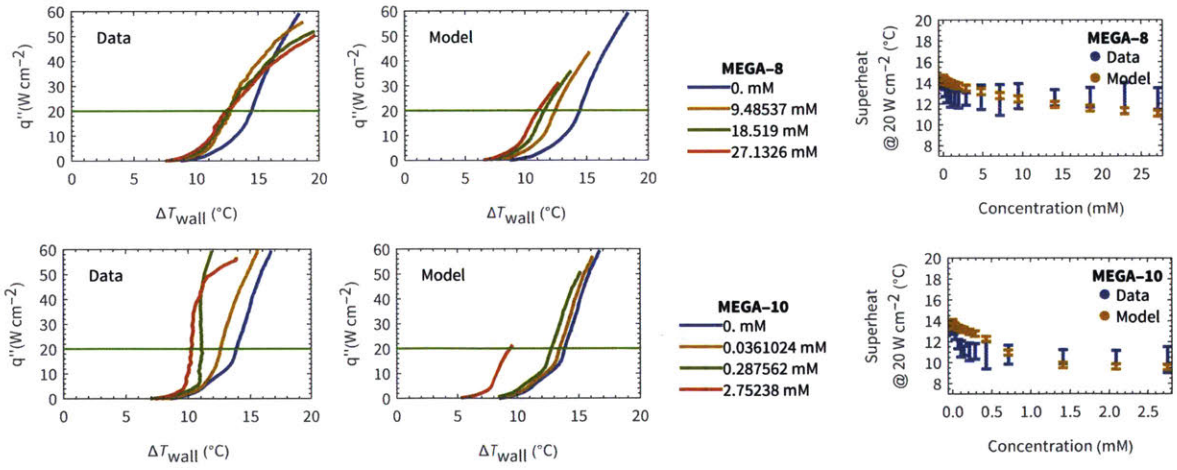

Figure 4-13: **Experimental validation of boiling curve model for MEGA surfactants.**

Applying the model for nonionic MEGA surfactants shows general agreement

with our experimental results as shown in Figure 4-13. There is a tendency to underpredict superheat drop at low concentrations, and a very slight overprediction at larger concentrations. This could be due to limitations in our assumption that solid-liquid adsorption is proportional to liquid-vapor surface tension (Eq. 2.7).

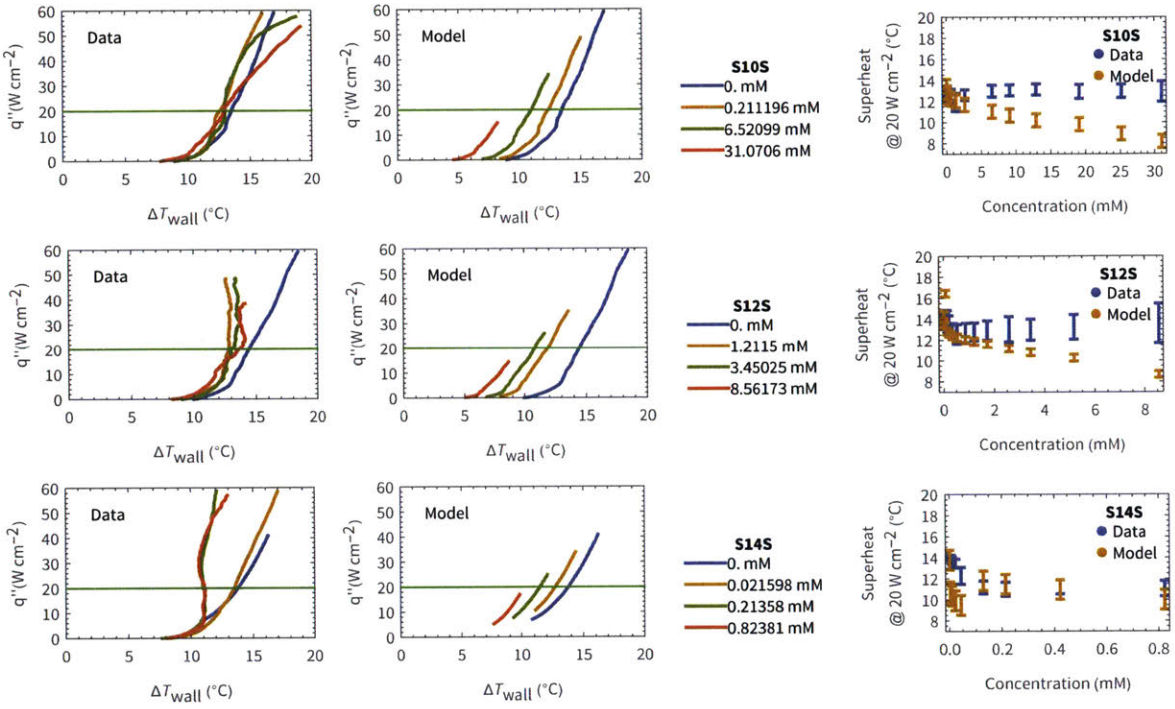

Figure 4-14: **Experimental validation of boiling curve model for SS surfactants.**

For anionic SS surfactants, the model tends to overpredict the drop in superheat as shown in Figure 4-13. Horizontal shifts in boiling curves tend to be overpredicted, indicating that nucleation enhancement seems to be slightly suppressed in reality. This can be explained by gold having a negative zeta potential. Thus, negatively charged SS surfactants should be somewhat repelled away from the surface, thereby reducing the hydrophobic surface effect diminishing the the enhancement of nucleation.

For cationic TAB surfactants, the model tends to underpredict superheat drop at low concentrations. This can be explained by positively charged TAB surfactants being attracted to the negative zeta potential gold. For lower CMC surfactants (14TAB and 16TAB), the experimental data shows a flattening (slope decrease) with in-

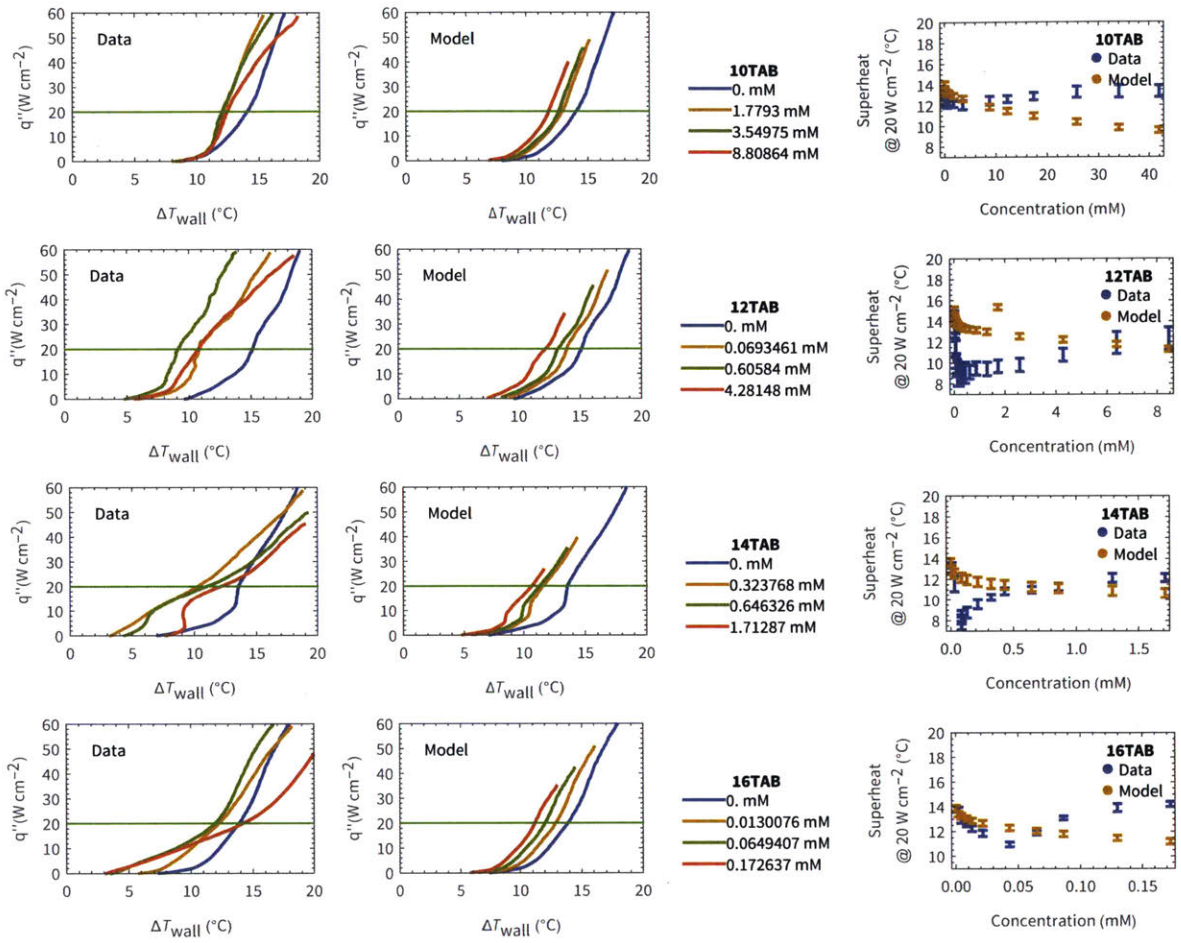

Figure 4-15: **Experimental validation of boiling curve model for TAB surfactants.**

creasing concentration as was mentioned in Chapter 2. This could be explained by a bubble-crowding effect due to non-coalescence of bubbles, which will be discussed next.

4.5.1 Bubble-crowding effects

When surfactants adsorb to the liquid-vapor interface, they can serve as a barrier against bubble coalescence. This effect can be used to prevent film boiling and increase CHF in low-gravity environments [110]. However, in the presence of appreciable gravity, non-coalescing behavior could have a detrimental effect. In snapshots of 16TAB solutions boiling shown in Figure 4-16, the low concentration solution (Figure 4-16b) has coalesced bubbles that are larger and more buoyant, leading

to greater liquid motion and higher convective heat transfer. On the other hand, the larger concentration solution (Figure 4-16c) has non-coalesced bubbles that are smaller and less buoyant leading to slower liquid motion and less effective convective heat transfer. Hence, the boiling curve of the higher concentration solution is flatter than that of the lower concentration (Figure 4-16a). Furthermore, the large surface-area-to-volume ratio of non-coalesced bubbles is likely to be more resistive to fluid flow, preventing effective convective heat transfer. It should be noted that the boiling model is only truly applicable in the limit of isolated bubbles since multi-bubble effects were not considered in the bubble growth and departure models. Despite this, reasonable predictions of basic trends have been captured.

4.6 Importance of solid-liquid adsorption over liquid-vapor adsorption

From boiling theory developed thus far, it is possible to evaluate the relative importance of solid-liquid adsorption to liquid-vapor adsorption. Contrary to previous literature where liquid-vapor surface tension effects were primarily deemed responsible for boiling enhancement [47, 50, 44], our modeling shows that lowering liquid-vapor surface tension can have a detrimental effect on heat transfer.[5] In Figure 4-17, relative single-bubble heat transfer (Eq. 4.34 but normalized over the maximum value of the pure water curve) is plotted as a function of contact angle. Conventional wisdom states that lower contact angles results in earlier departure, higher bubble frequencies, and, thus, higher heat transfer per bubble cycle. However, growth rate is primarily dependent on superheat and applying classical $D_{\text{equiv}} \sim t^{1/2}$ growth results in much smaller bubble departure sizes that effectively lowers the single-bubble heat transfer for decreasing contact angle as shown in the $t^{1/2}$ gray dashed curve in Figure 4-17. However, $D_{\text{equiv}} \sim t^{1/4}$ growth predicted by our growth model when the bubble is much larger than the thermal boundary layer does agree with conventional

[5]This is in addition to bubble-crowding effects described in the previous Section.

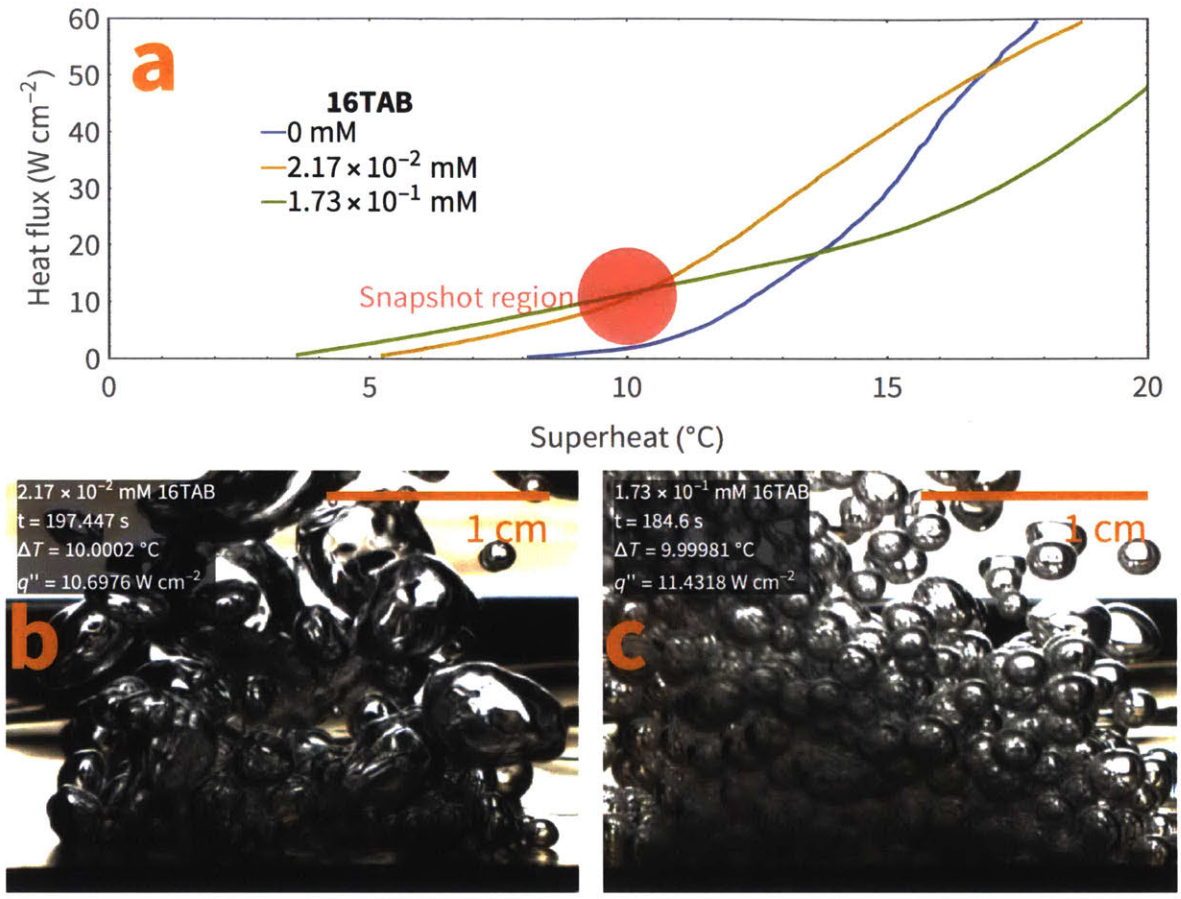

Figure 4-16: **Bubble-crowding effect with 16TAB.** (a) Boiling curves for 16TAB at 0 mM, 2.17×10^{-2} mM, and 1.73×10^{-1} mM with snapshot region highlighted where snapshots (b) and (c) are taken. (b) At a lower concentration (2.17×10^{-2} mM), there is less liquid-vapor adsorption and coalescence of bubbles. (c) At a higher concentration (1.73×10^{-1} mM), there is more liquid-vapor adsorption and non-coalescence of bubbles.

wisdom where single-bubble heat transfer increases with lower contact angles ($t^{1/4}$ gray dashed curve in Figure 4-17). Since there is a transition to $t^{1/4}$ growth in the model from $t^{1/2}$ growth, the single-bubble heat transfer is approximately invariant with contact angle after $\sim 40°$. Keeping contact angle constant, but lowering liquid-vapor surface tension, however, always results in slightly lower single-bubble heat transfer due to earlier departure and smaller bubble size as shown by the blue and orange curves in Figure 4-17. This is an effect that was not captured in previous studies since contact angle is coupled to the liquid-vapor surface tension. Thus, the link between lowering liquid-vapor surface tension and boiling enhancement is not

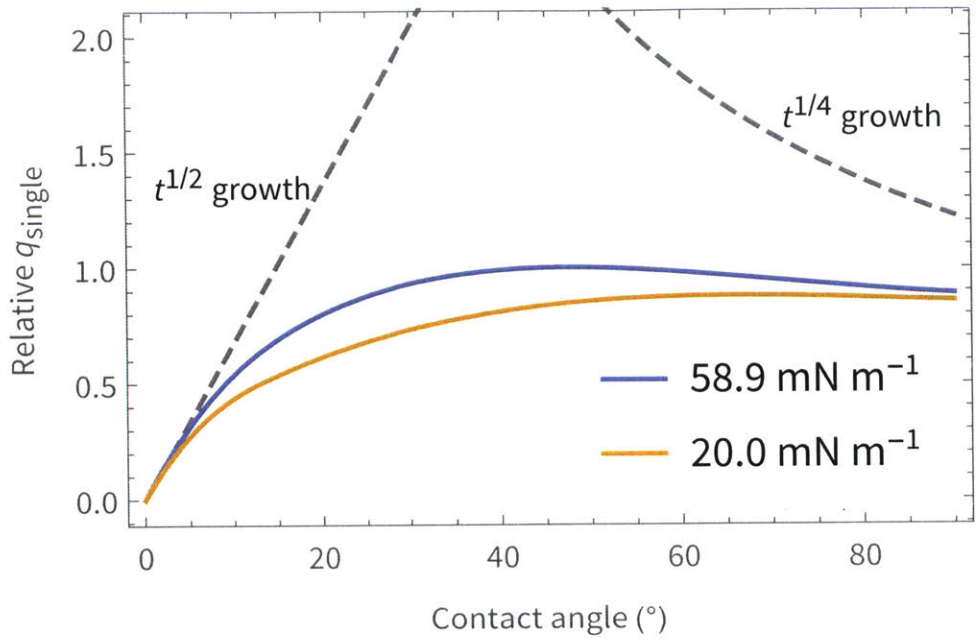

Figure 4-17: **Single-bubble heat transfer for two different liquid-vapor surface tensions.** Heat transfer is normalized by the maximum value of the 58.9 mN m^{-1} curve (0.635 W). The 58.9 mN m^{-1} curve corresponds to pure water at 100 °C. Lowering surface tension lowers single-bubble heat transfer due to smaller departure size. Values calculated for a superheat of 10 °C.

due to effects at the liquid-vapor interface, but rather the associated effects at the solid-liquid interface. If solid-liquid and liquid-vapor effects could be decoupled, then it would be desirable to have a high liquid-vapor surface tension and a high contact angle (high solid-liquid adsorption and low liquid-vapor adsorption).

A small change in solid-liquid adsorption can change the contact angle (Eq. 4.5) and shift the boiling curve horizontally a few degrees. Depending on the shape of the boiling curve, a few degrees shift left can increase the HTC by orders of magnitude (higher if the boiling curve is steep to begin with). While it was mentioned in Chapter 2 that solid-liquid adsorption is proportional to liquid-vapor adsorption, the two behaviors can be decoupled since liquid-vapor adsorption is dynamic (liquid-vapor adsorption repeats itself with each bubble cycle) while solid-liquid adsorption is static (equilibration happens before boiling).

4.7 Effect of molecular parameters

With the modeling framework validated, the effect of molecular parameters on boiling heat transfer performance can be evaluated. We primarily examined the effect of two parameters: head size and tail length since these vary widely between different types of surfactants.

4.7.1 Head size

To compare two surfactants of different head sizes, MEGA-10 (small head in this case) was compared against a hypothetical nonionic surfactant with a larger head. The molecular properties are listed in Table 4.1.

Table 4.1: Small- and large-head surfactants

	$\frac{g_{head}}{kT}$	a_{exc} (Å^2)	d_{head} (Å)	n_c	m (u)
Small	-3.8	38.4	4.9	10	349
Large	-7.5	76.8	7.0	10	988

The large-head surfactant had twice the excluded area of the small-head surfactant. The head geometries were assumed to be spherical and the same head density was assumed in order to calculate the mass. g_{head} was adjusted such that both surfactants would attain a surface pressure of 20 mN m^{-1} at 2.4 mM in order to isolate the effect of just changing head size.

In Figure 4-18, boiling curves of the small- and large-head surfactants are shown at two concentrations (0.24 mM and 2.4 mM). Both surfactants provide similar performance at 2.4 mM but the large-head surfactant has less degradation in performance at 0.24 mM compared to the small-head. Thus, large-head surfactant is less sensitive to changes in concentration. This can be attributed to the fact that the surface tension isotherm of the large-head is less steep than that of the small-head as shown in Figure 4-19a. That is, much greater changes in concentration are required to change surface tension of a large-head surfactant due to the added steric interaction between surfactants. The similarity in performance at 2.4 mM can be attributed

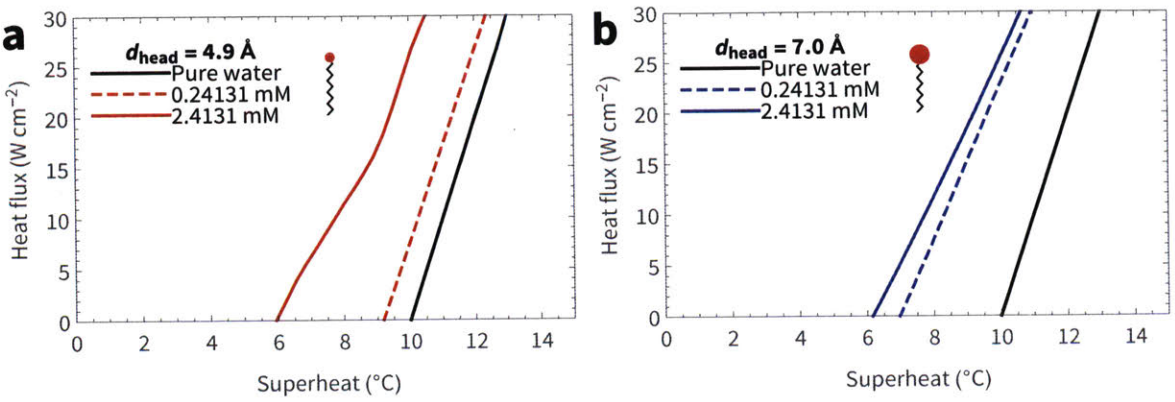

Figure 4-18: **Boiling curve comparison between small- and large-head surfactants.** The boiling curve of the (a) small-head surfactant solution is more sensitive to changes in concentration than that of the (b) large-head surfactant.

to the fact that both surfactants were designed such that they attain the same equilibrium surface tension at the same concentration, thus resulting in similar diffusion dynamics as shown in Figure 4-19b.

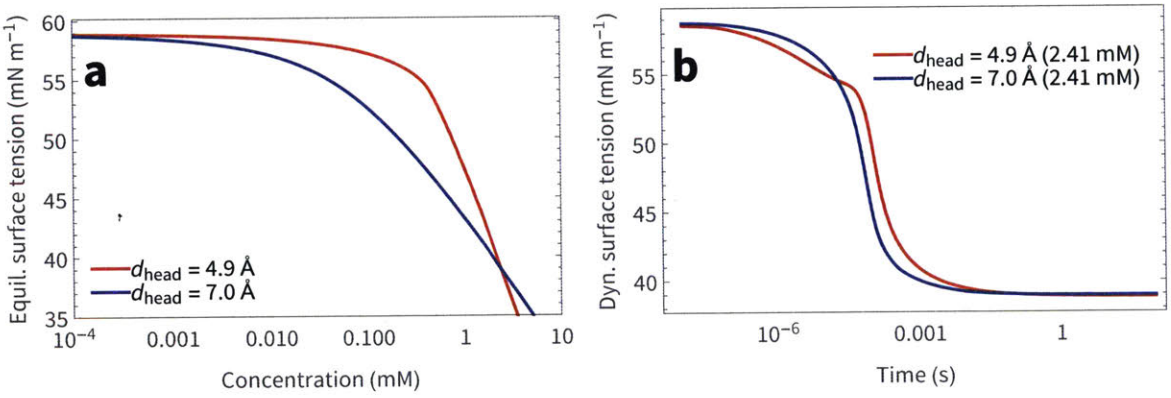

Figure 4-19: **Comparison in equilibrium and dynamic surface tensions between small- and large-head surfactants.** (a) The equilibrium surface tension isotherm of large-head surfactant is less steep than that of a small-head surfactant. (b) Both small- and large-head surfactants have similar dynamic surface tension behavior at 2.4 mM.

Thus, it can be concluded that larger head surfactants may be more desirable in applications where concentration cannot be easily controlled and consistent boiling performance is required.

4.7.2 Tail length

To investigate the effect of different tail lengths, MEGA-10 (short-tail surfactant in this comparison) was compared against a longer tail surfactant MEGA-14. The molecular properties are listed in Table 4.2.

Table 4.2: Short- and long-tail surfactants

	$\frac{g_{\text{head}}}{kT}$	a_{exc} (Å^2)	d_{head} (Å)	n_c	m (u)
Short	-3.8	38.4	4.9	10	349
Long	-3.8	38.4	4.9	14	406

The long-tail surfactant had a tail length of 14 carbons while the short-tail had a tail length of 10 carbons. All other properties remained the same except the expected mass increase associated with changing the tail. In contrast to the small- and large-head comparison, g_{head} was not modified since nothing about the head was changed. Hence, very different concentrations are required. To attain 20 mN m^{-1} in equilibrium liquid-vapor surface pressure, the short-tail required 2.4 mM while the long-tail required only 0.01 mM.

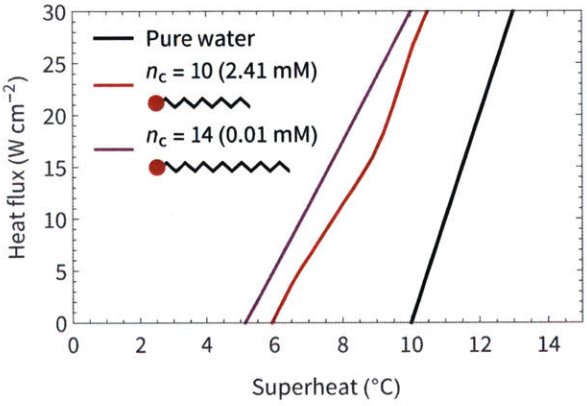

Figure 4-20: **Comparison of boiling curves between short- and long-tail surfactants.** The concentration of both surfactants is such that the equilibrium surface pressure of each solution is 20 mN m^{-1}.

As shown in Figure 4-20, despite having the same equilibrium surface pressure, the long-tail surfactant shows better performance. Due to the much smaller concentrations required for the long-tail surfactant as shown by the surface tension

isotherms in Figure 4-21a, diffusion to the liquid-vapor interface would be much slower as shown in Figure 4-21b. Hence, the long-tail surfactant is expected to have a higher liquid-vapor surface tension and subsequently larger single-bubble heat transfer as described in 4.6 (if compared at the same contact angle). But more importantly, nucleation is slightly higher for the long-tail surfactant since a nucleation timescale of 1 ms was taken into account as described in 4.4. That is, despite the short- and long-tail surfactants having the same θ_{init}, the "effective, nucleation-timescale θ_{init}" is higher for the long-tail surfactant since 1 ms has elapsed and less surfactants would have adsorbed to the liquid-vapor interface. Therefore, the nucleation density for the long-tail surfactant would be slightly higher.

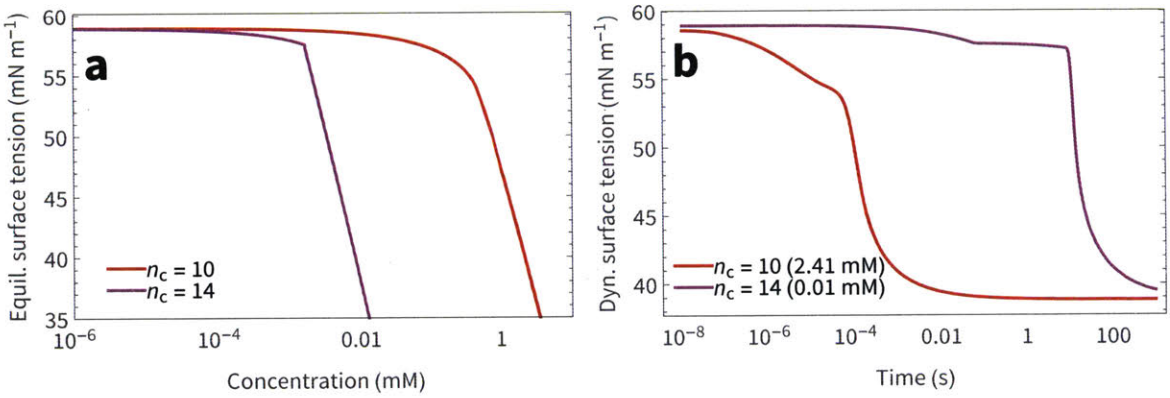

Figure 4-21: **Equilibrium and dynamic liquid-vapor surface tensions for short- and long-tail surfactants.** (a) Long-tail surfactants require smaller concentrations for comparable equilibrium surface tension. (b) Due to the lower concentrations, diffusion is much slower for long-tail surfactants.

Due to the orders-of-magnitude difference in required concentrations, it would be desirable to use long-tail surfactants (or low-CMC surfactants) from both a cost and performance perspective. Lower concentrations minimize liquid-vapor adsorption, which would minimize any detrimental drop in liquid-vapor surface tension and single-bubble heat transfer as described in Section 4.6. In addition, bubble-crowding effects (described in Section 4.5.1) could be avoided. However, in certain situations such as in micro-gravity environments or upside-down boilers where the lack of an effective departure force causes early bubble coalescence and CHF, non-coalescence and short-tail surfactants may be desired [110].

4.8 Summary

In this Chapter, we have detailed how using dynamic surface tension obtained from molecular parameters (Chapter 3) can be used to determine the enhancement in boiling. Solid-liquid adsorption is assumed to be proportional to liquid-vapor adsorption as was explained in Chapter 2 (Eq. 2.7). A cavity model is presented based on conical geometry, which allows for the calculation of a change in superheat (horizontal shift in boiling curve) as a function of contact angle based on the Clausius-Clapeyron relation (Eq. 4.5). Then, to determine the vertical shift in the boiling curve, we developed a bubble growth (Eq. 4.22) and departure model (Section 4.3.3) that takes into account time-dependent surface tension and contact angle. From there, a methodology is described in which the boiling curve can be shifted horizontally and vertically from a reference pure water curve (Section 4.4). General trends observed in experimental boiling curves are captured by the modeled boiling curves. Molecular insights have been gained as a result of developing this framework: larger heads are less sensitive to changes in concentration, and longer tails require smaller concentrations. Solid-liquid adsorption was found to be the primary reason for enhancement due to increased nucleation while liquid-vapor adsorption was found to be slightly detrimental as it lowers single-bubble heat transfer and causes non-coalescing, bubble-crowding effects. This is a key insight as previous studies have focused on the effects of liquid-vapor surface tension and incorrectly attributed enhancement to liquid-vapor interfacial effects when enhancement is actually due to solid-liquid effects that are *associated* with liquid-vapor effects. Thus, decoupling the effects by minimizing dynamic liquid-vapor adsorption using low-CMC surfactants is one strategy to maximize performance. In addition, we found that a slightly charged surface (from intrinsic zeta potentials) was likely altering solid-liquid adsorption and affecting nucleation behavior. In Chapter 5, we will explore this effect in further detail and offer a novel way to control boiling using *applied* electric fields.

CHAPTER 5

ACTIVE BOILING CONTROL WITH ELECTRIC FIELDS

Recognizing the importance that solid-liquid adsorption has on the shape of the boiling curve wherein even small zeta potentials can shift the boiling curve, we used applied electric fields and charged surfactants to realize an active control of the bubble nucleation process. Since controlling the solid-liquid adsorption changes the hydrophobicity of the surface, nucleation can be controlled by an applied electric field to the degree that boiling can be turned "on" and "off."

5.1 Previous work on active boiling control

Applying electric fields in a heat transfer context is not new. Electrohydrodynamic (EHD) convection and boiling enhancement uses large electric potentials ($\sim 10^3$ V) in a dielectric fluid to effect an increase in heat transfer coefficient [40, 111, 112]. The mechanism of EHD heat transfer enhancement is convection enhancement due to a body force in the thermal boundary layer, which stems from a temperature dependence of the dielectric constant. For more information, see Appendix D.

Another method of active control is to use the electrowetting (EW) effect. Electrowetting is the observed increase in wetting (decrease in contact angle) when an electric field is applied [113]. This can be explained by electromigration of ions in the solution decreasing the solid-liquid interfacial energy; hence, the solid-vapor surface tension is able to lower the contact angle. EW has been shown to suppress the Leidenfrost (film boiling) effect and enhance quench cooling [114]. EW typically requires voltages on the order of 10^2 V to 10^3 V, however, and an insulating coating must usually be applied on the surface to avoid redox reactions. For more information, see Appendix D.

5.2 General principles

In our method of enhancement, we use charged surfactants (anionic and cationic) and very low voltages (~ 1 V) to effect changes in boiling nucleation and heat transfer. The mechanism is fundamentally different from previous electric field active boiling methods. Here, we apply a potential between the boiling surface and a counter electrode in the bulk fluid to attract or repel charged surfactants, changing the solid-liquid adsorption according to electric double layer theory. In effect, the system acts as a capacitor where surfactants adsorbing are considered to be charging the surface. As such, we are changing the "initial" contact angle described in Chapter 2, which results in an increase in nucleation as described by entrapped vapor theory (see Chapters 1 and 4). While EW and EHD effects can certainly be present, due to the low electric fields in our system, their effects can be neglected in our system (Appendix D).

Controlling the solid-liquid adsorption with electric fields also offers the opportunity to decouple solid-liquid and liquid-vapor effects. This is important since, by default, these behaviors are highly coupled. In Chapter 2, we showed that solid surface tension was approximately proportional to liquid-vapor surface tension, which is likely due to similar thermodynamic behavior happening at solid and vapor interfaces. However, when a potential is applied between the surface and a counter

electrode, much of the potential drop exists across the EDL at the solid-liquid interfaces. Meanwhile, no electric field is applied at vapor interfaces, so no changes to liquid-vapor surface tension occur; hence, a decoupling of the two interfacial phenomena can be in effect.

5.2.1 Identifying suitable materials

One challenge with any electric field based work with liquids is corrosion and electrolysis. Both are redox chemical reactions that occur at the electrode surfaces. Corrosion refers to oxidation or reduction of the electrode itself, while electrolysis is the oxidation and reduction of water (water splitting into hydrogen and oxygen). Electrolysis of water can occur in *any* electrode system and will begin to occur at potential differences of 1.23 V at room temperature. However, potentials much higher than that are often needed to generate appreciable amounts of hydrogen and oxygen.

Since electrolysis cannot be avoided, any application involving water should be limited only to a few volts. To avoid corrosion, suitable materials for the boiling surface (working electrode) and counter electrode should be chosen. Electrochemical reactions are not completely avoidable; thus, we decided that the boiling surface should be very slightly reduced to maintain its purity during boiling and the counter electrode should be slightly oxidized since it can be considered a sacrificial material. Practical difficulties with sample mounting to the boiling apparatus limited us to using noble metal boiling surfaces; therefore, silver foil was used (active area of silver foil for electrochemical reactions was 58 mm × 58 mm). For the counter electrode, kinetics should be as slow as possible, which would provide a very large potential window for capacitive behavior as shown in Figure 5-1.

After cyclic voltammetry (CV) testing in which current is recorded while voltage between a sample electrode and a reference electrode (Ag/AgCl in this case) is swept, it was determined that titanium provided suitably slow kinetics for a counter electrode as shown by Figure 5-2. High surface area of the counter electrode in

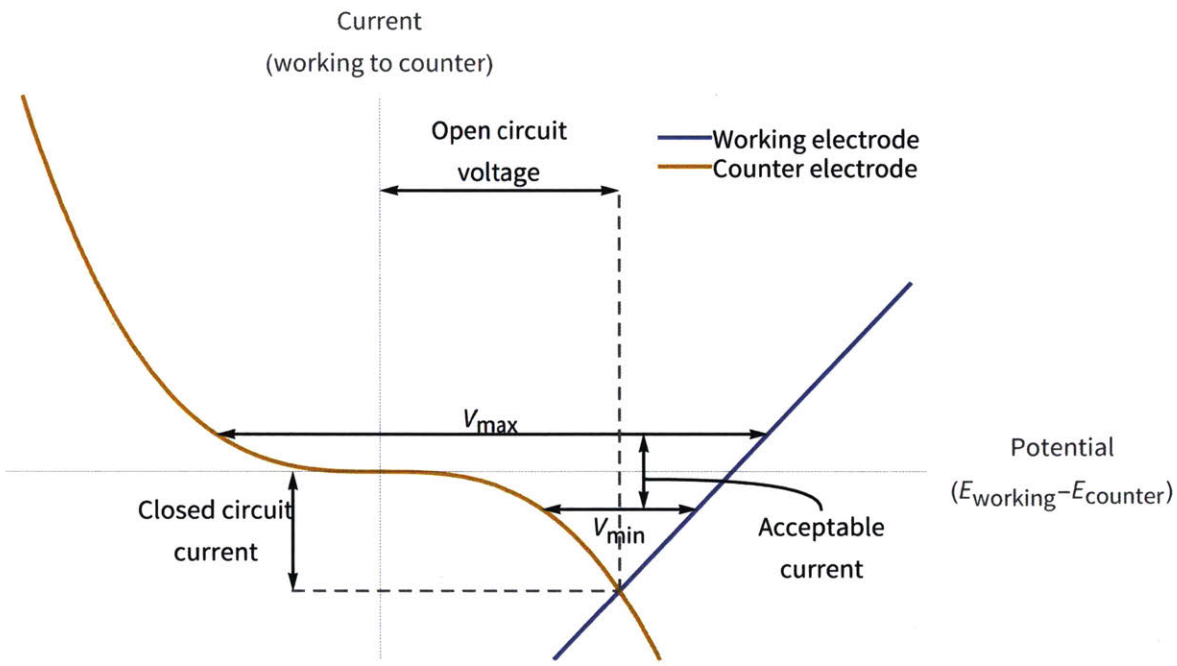

Figure 5-1: **Identifying a potential window from electrode behavior.** A working electrode with fast kinetics (large I-V curve slope) and a counter electrode with slow kinetics (small I-V curve slope) with different Nernst potentials have a finite open circuit potential (when current is zero). Having one electrode with slow kinetics (counter electrode in this case) allows for a wide potential window $V_{max} - V_{min}$ for an acceptable current range.

comparison to the working electrode is necessary to maximize adsorption; thus, the counter electrode consisted of a 40×40 (US standard) titanium mesh (for high surface area) around a 6.35 mm diameter titanium rod.

After identifying appropriate electrode materials (silver for the boiling surface, and titanium for the counter electrode), CV testing of the silver-titanium system in the presence of different surfactants at equal concentrations allowed for identification of a suitable potential window as shown in Figure 5-3. Surfactants used were SDS (S12S) and DTAB (12TAB). In addition, sodium bromide (NaBr)—which are the counterions of SDS and DTAB—and a nonionic surfactant MEGA-10 are used as controls. To ensure slight reduction of the boiling surface, the negative potential range of $-0.1\,\mathrm{V}$ to $-2.0\,\mathrm{V}$ ($E_{cell} = E_{surface} - E_{counter}$) was used. Cyclic voltammetry tests show that there is a purely capacitive region near $-0.1\,\mathrm{V}$ to $-0.8\,\mathrm{V}$ and electrolysis afterwards as shown in Figure 5-3. However, the rate of electrolysis does

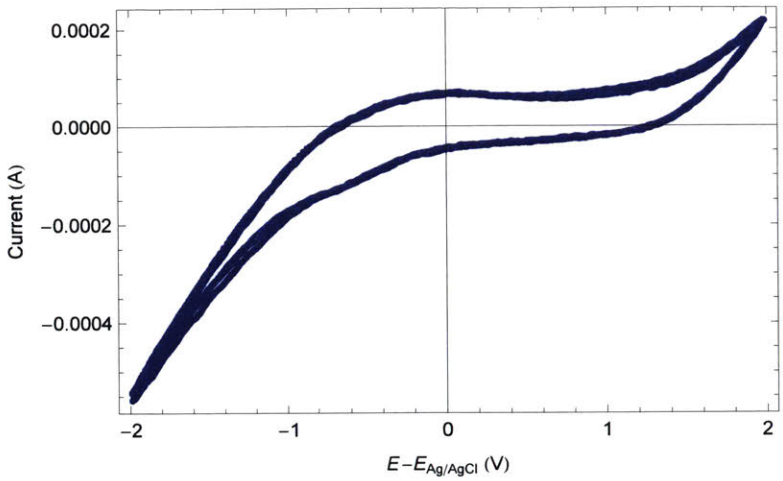

Figure 5-2: **Titanium I-V curve shows slow kinetics.**

not exceed $60\,\mu\mathrm{A\,cm^{-2}}$ (highest for NaBr, lower for surfactants). This corresponds to a power of $2 \times 10^{-4}\,\mathrm{W\,cm^{-2}}$, which is a negligible power consumption compared to typical boiling heat fluxes. If we assume all of this current contributes to hydrogen production (splitting of water), then the hydrogen generation rate at 100 °C and atmospheric pressure is $0.01\,\mu\mathrm{L\,cm^{-2}\,s^{-1}}$. This very low hydrogen generation rate is consistent with the lack of any observation of bubbles being generated at low heat fluxes despite a voltage of −2 V applied. Beyond −2 V, bubbles were observed to spontaneously form due to electrolysis.

5.3 Experimental results

5.3.1 Turning on and off nucleation

Several different types of experiments were performed to study and demonstrate the electric field enhanced boiling effect. First we sought to actively control bubble nucleation to the extent of turning bubble formation "on and off" (Figure 5-4). We applied a constant heat input of 60 W to boil deionized (DI) water with 2.6 mM of negatively charged surfactant SDS within a 2 cm × 2 cm area on a silver boiling surface (Figure 5-4a). The silver foil boiling surface itself had an area of 58 mm × 58 mm exposed to liquid, i.e. the area active to applied electric fields.

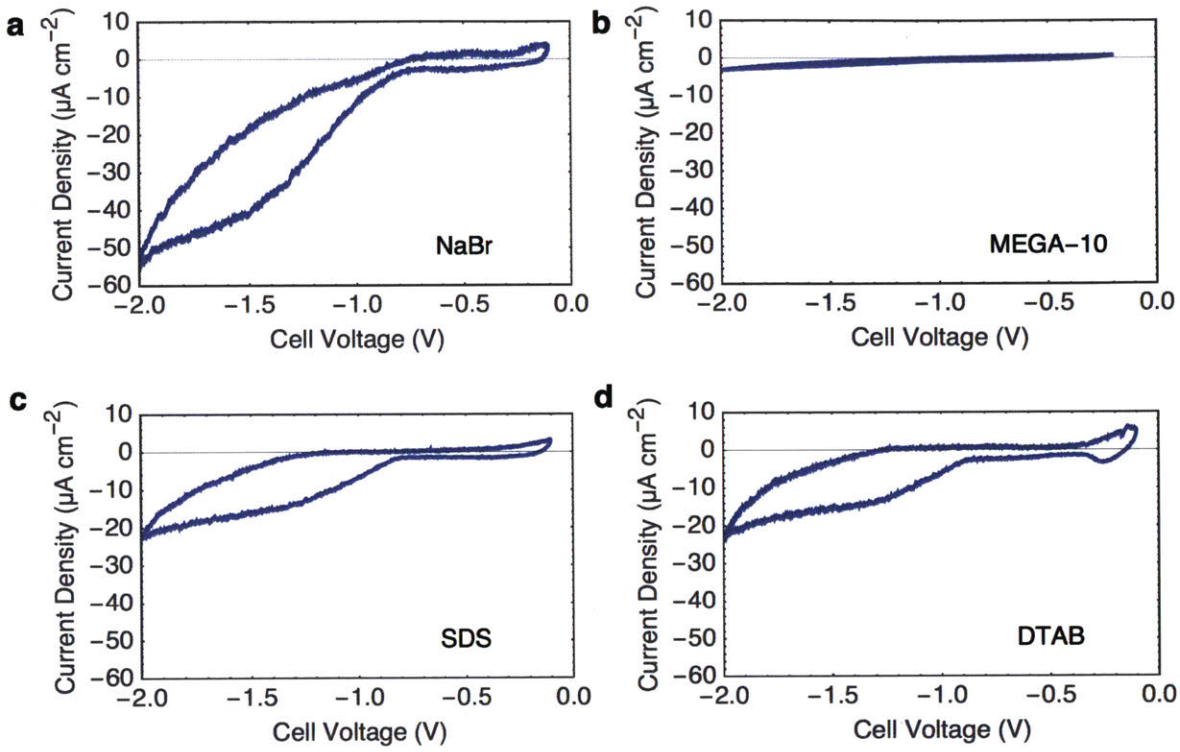

Figure 5-3: **CV scans demonstrate capacitive behavior and low electrolysis.** CV scans were obtained for 2.6 mM (a) NaBr, (b) MEGA-10, (c) SDS, and (d) DTAB at a voltage sweep rate of 10.6 mV s^{-1}. At this sweep rate, currents are at their steady-state values (lower sweep rates did not significantly change the current values). From −0.1 V to −0.8 V, all current responses were flat indicating purely capacitive behavior. Beyond −0.8 V, the current response was low ($< 60 \mu$A cm^{-2}) indicating that electrolysis is negligible.

During boiling, we changed the electric potential applied between the surface and a counter electrode immersed in the fluid from −0.1 V to −2.0 V, which resulted in bubble nucleation immediately subsiding (Figure 5-4b). The more negative potential electrostatically repelled the negatively charged SDS away from the surface, diminishing the hydrophobic "coating" on the surface, which increased wettability and suppressed nucleation. The weakening of the negative potential from −2.0 V to −0.1 V electrostatically attracted SDS to the surface, augmented the hydrophobic "coating" and increased nucleation (Figure 5-4c). Both nucleation suppression and promotion occurred rapidly (< 600 ms and < 300 ms, respectively). The difference in settling times can be attributed to nucleation hysteresis [115].

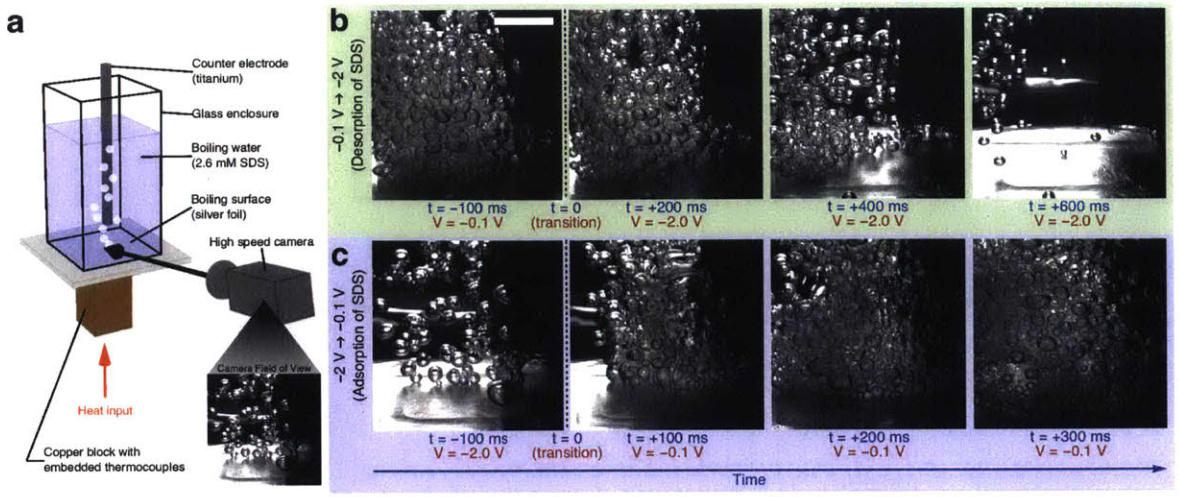

Figure 5-4: **Turning boiling on and off with a potential switch.** (a) Pool boiling of a solution of 2.6 mM SDS (negatively charged) in DI water at a constant heater power of 60 W with potential applied between the silver foil boiling surface and an immersed titanium counter electrode. A (b) −0.1 V to −2.0 V switch decreased bubble nucleation within 600 ms due to electrostatic desorption of SDS from boiling surface. A (c) −2.0 V to −0.1 V switch increased nucleation within 300 ms due to adsorption of SDS. The scale bar is 1 cm.

5.3.2 Square wave potential experiments

To investigate the adsorption/desorption mechanism in more detail, we quantified the electrical and thermal response of both the negatively charged surfactant SDS and the positively charged surfactant dodecyl trimethylammonium bromide (DTAB) to an applied square-wave potential (E_{cell} ranged between −0.1 V and −2.0 V; 60 s period) (Figure 5-5). The current response for SDS and DTAB (Figure 5-5) confirmed capacitive behavior with a steady state current not exceeding 60 μA cm^{-2}. The thermal response supported the adsorption/desorption mechanism. For negatively charged SDS, the temperature increased and the HTC decreased with more negative potential (repelling SDS) since more heat was dissipated through convection as opposed to vapor generation. Accordingly, the temperature was out-of-phase with potential while the HTC was in-phase with potential (Figure 5-5a). In contrast, with positively charged DTAB, the opposite temperature and HTC response was obtained (Figure 5-5b) as expected.

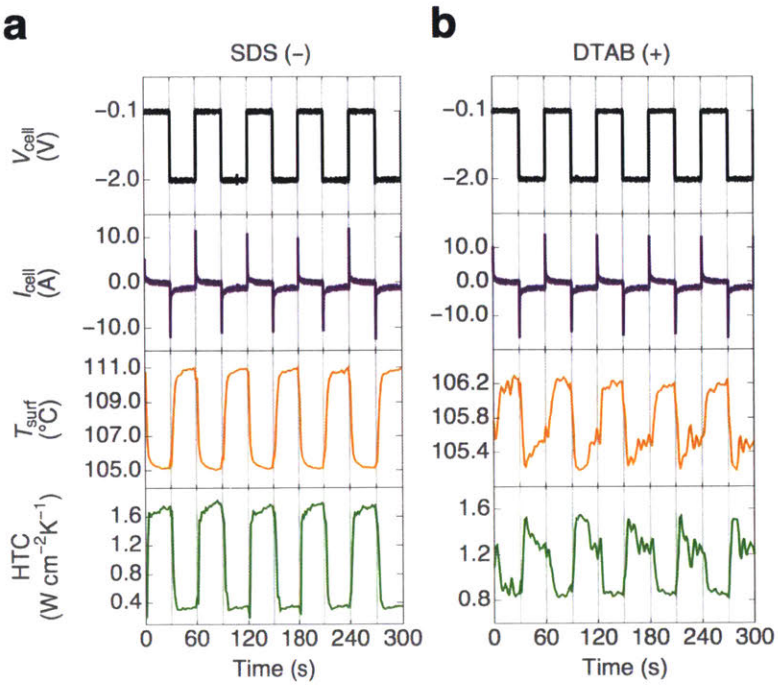

Figure 5-5: **Electrical and thermal responses to a square-wave potential.** (a) Positively charged DTAB had an in-phase temperature response and an out-of-phase HTC response compared with the voltage input. Conversely, (b) negatively charged SDS had an out-of-phase temperature response and an in-phase HTC response compared with the voltage input. For both surfactants at 2.6 mM, the input voltage switched between −0.1 V and −2.0 V with a period of 60 s and the current response was capacitive.

5.3.3 Additional experiments with control additives

Additional experiments where the potential input was a slow triangle-wave (quasi-static change in potential) corroborated the square-wave experiments (Figure 5-6). The oppositely charged surfactants had opposite thermal responses to the same voltage input. For control additives NaBr and MEGA-10, there was no change in nucleation, temperature, or HTC with potential for the negative controls (Figure 5-6 and Figure 5-7). Direct measurements of the advancing contact angles with NaBr, MEGA-10, SDS, and DTAB under boiling conditions with different potentials (Figure 5-8) were consistent with the observed changes in nucleation. In fact, the contact angle of DTAB increased with voltage magnitude as expected; this demonstrates a phenomenon that is completely different from electrowetting. Furthermore, the

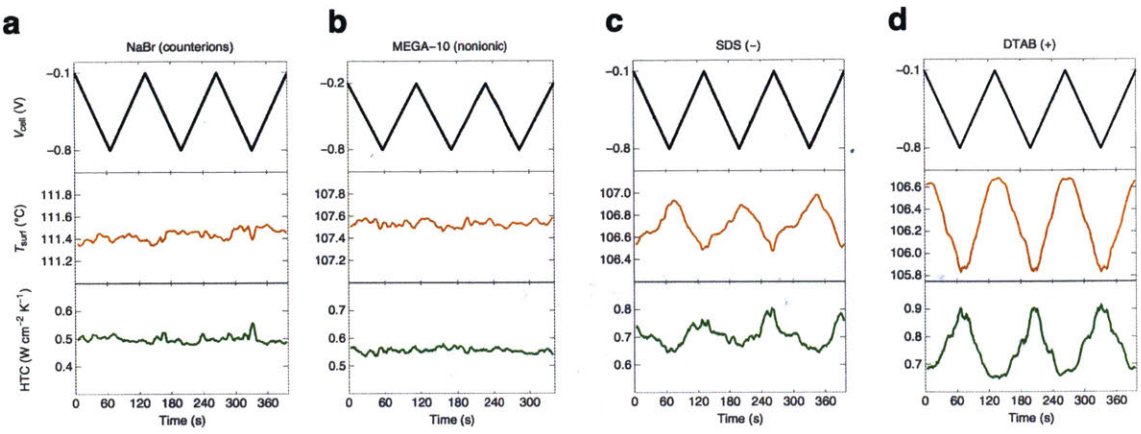

Figure 5-6: **Thermal responses to triangle-wave potentials show that only charged surfactants respond and do so according to their charge.** Temperature and HTC for (a) NaBr and (b) MEGA-10 did not respond to the potential input, while (c) SDS and (d) DTAB did respond in opposite directions from each other. The thermal response in SDS and DTAB was continuous within the voltage sweep range. The voltage ranged from −0.1 V to −0.8 V except for MEGA-10 which ranged from −0.2 V to −0.8 V due to limitations of experimental setup. The voltage sweep rate was 10.6 mV s^{-1}. This voltage range is in the purely capacitive region according to Figure 5-3.

contact angle measurements and triangle-wave experiments rule out other mechanisms for actively controlled boiling, i.e. EHD or electrolysis, both of which do not rely on charged surfactants. Since the system is capacitive, the number of adsorbed charged surfactant, alteration of boiling nucleation, temperature, and HTC (Figure 5-6) should gradually change with potential as was observed (i.e. there is no critical voltage at which these changes suddenly activate). These results indicate that charged surfactants electrostatically adsorb to the surface, decrease wettability, and increase nucleation.

5.3.4 Field-induced tunability of heat transfer performance

The performance and degree of field-induced tunability of boiling was quantified by obtaining and analyzing boiling curves (Figure 5-9). In these experiments, 2.6 mM of either NaBr, MEGA-10, SDS, or DTAB was added to DI water and an E_{cell} was applied while the heater power was varied in a quasi-static manner.

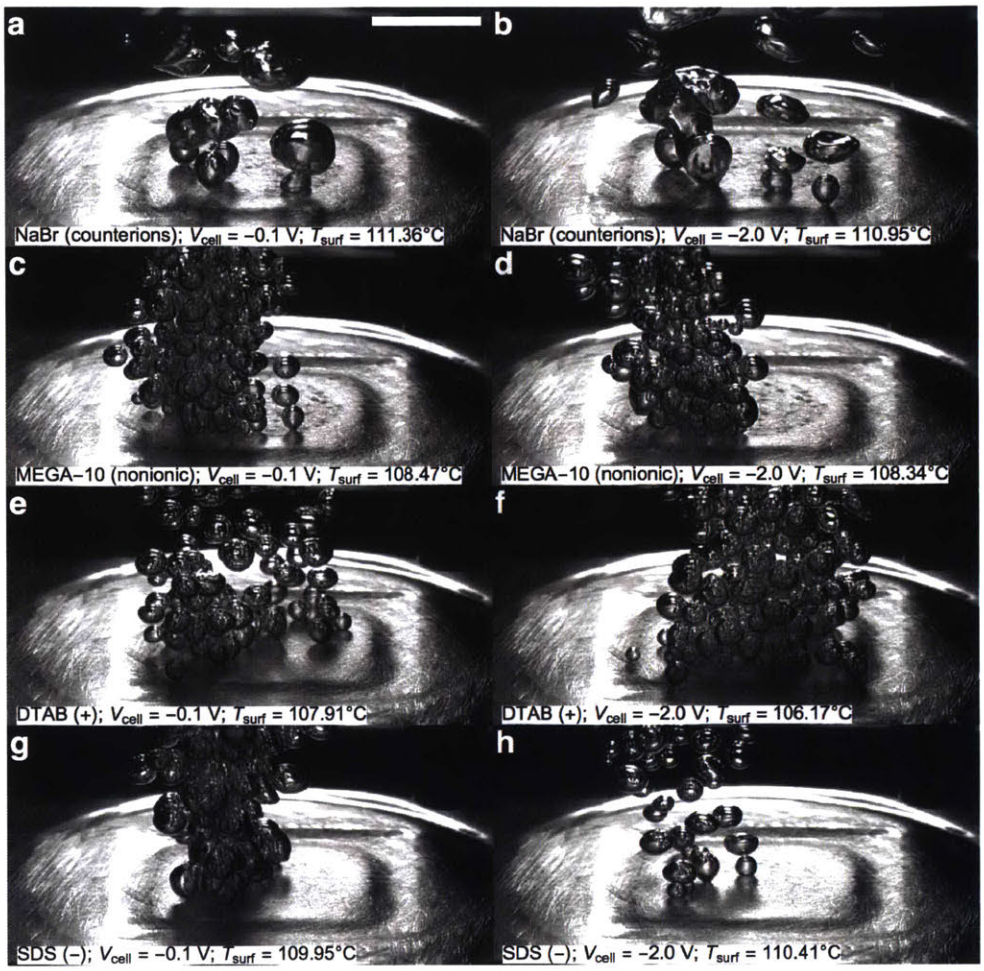

Figure 5-7: **Snapshots during boiling show nucleation changes for charged surfactants.** The heat flux was approximately 5 W cm^{-2}. NaBr at (a) −0.1 V and (b) −2.0 V had no significant change in nucleation density. MEGA-10 at (c) −0.1 V and (d) −2.0 V also had no significant change in nucleation density. For positively charged DTAB, less nucleation and more superheat were observed at (e) −0.1 V than (f) −2.0 V since less heat was being dissipated through phase change. For negatively charged SDS, more nucleation and less superheat were observed at (g) −0.1 V than −2.0 V. The scale bar is 1 cm.

The boiling curves of NaBr and MEGA-10 at −0.1 V and −2.0 V did not change with potential (Figure 5-9a,b), confirming the negative control results. Meanwhile, boiling curves at −0.1 V and −2.0 V for the ionic surfactants (SDS and DTAB) deviated from each other as expected. The boiling curve for SDS at −2 V was shifted right compared to the baseline −0.1 V curve due to increased wettability and decreased nucleation. The space between the −0.1 V and −2.0 V boiling curves represent the ability to actively control (tune) boiling where the HTC for SDS could be increased

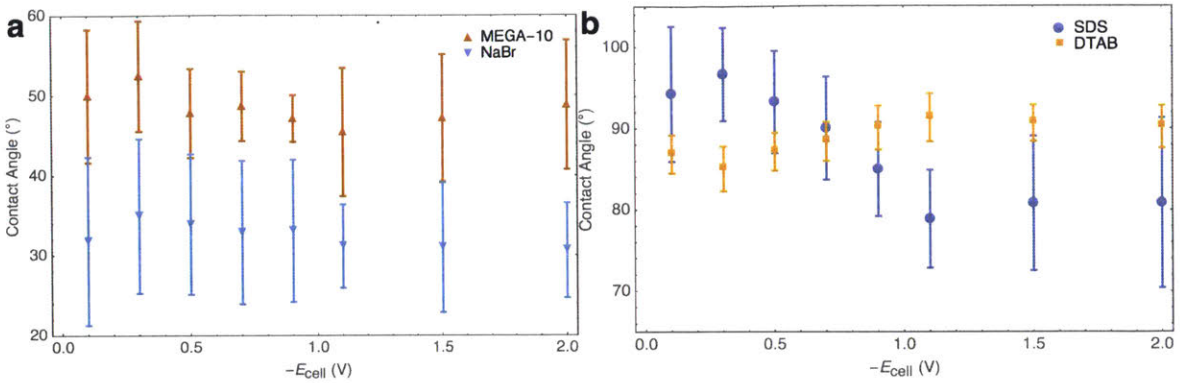

Figure 5-8: **Effect of electric potential on contact angle with controls and charged surfactants.** Advancing contact angle measurements were made at 100 °C. Uncertainty bars represent two standard deviations in contact angle measurement from different image frames and fitting. (a) Control additives have little effect on contact angle while (b) charged surfactants show changes in contact angle when the electric potential is changed. Positively charged DTAB is more attracted to the surface at more negative potentials; thus, the increased adsorption results in a higher advancing contact angle. SDS, on the other hand, is more repelled at more negative potentials; thus, the desorption results in a lower advancing contact angle.

up to approximately 1000 % over its minimum value at −2.0 V for a given superheat. This HTC increase can be seen in the vertical arrows at 8.7 °C superheat in Figure 5-9c, where the top arrow points to approximately 41 W cm^{-2} on the −0.1 V curve and the bottom arrow to approximately 3.7 W cm^{-2} on the −2.0 V curve. Furthermore, the temperature could be varied by more than 2 °C; the black horizontal arrows located at 17 W cm^{-2} in Figure 5-9c have a high superheat on the −2.0 V curve of 7.5 °C and a low superheat on the −0.1 V curve of 10 °C. The increase in CHF for SDS at more negative potential (not shown but inferred) is consistent with increased wettability due to surfactants leaving the surface. Conversely, applying a more negative potential to positively charged DTAB decreased wettability to shift the boiling curve left and increase CHF compared to the baseline −0.1 V (Figure 5-9d).

The HTC for DTAB could be increased from its value at −0.1 V up to 1100 % at a given superheat; the vertical arrows at 7 °C superheat in Figure 5-9d have a high heat flux on the −2.0 V curve of approximately 20 W cm^{-2} and a low heat flux on the −0.1 V curve of approximately 1.6 W cm^{-2}. The temperature for DTAB could be varied up to nearly 2 °C by voltage change; horizontal arrows at 3.8 W cm^{-2} in Fig-

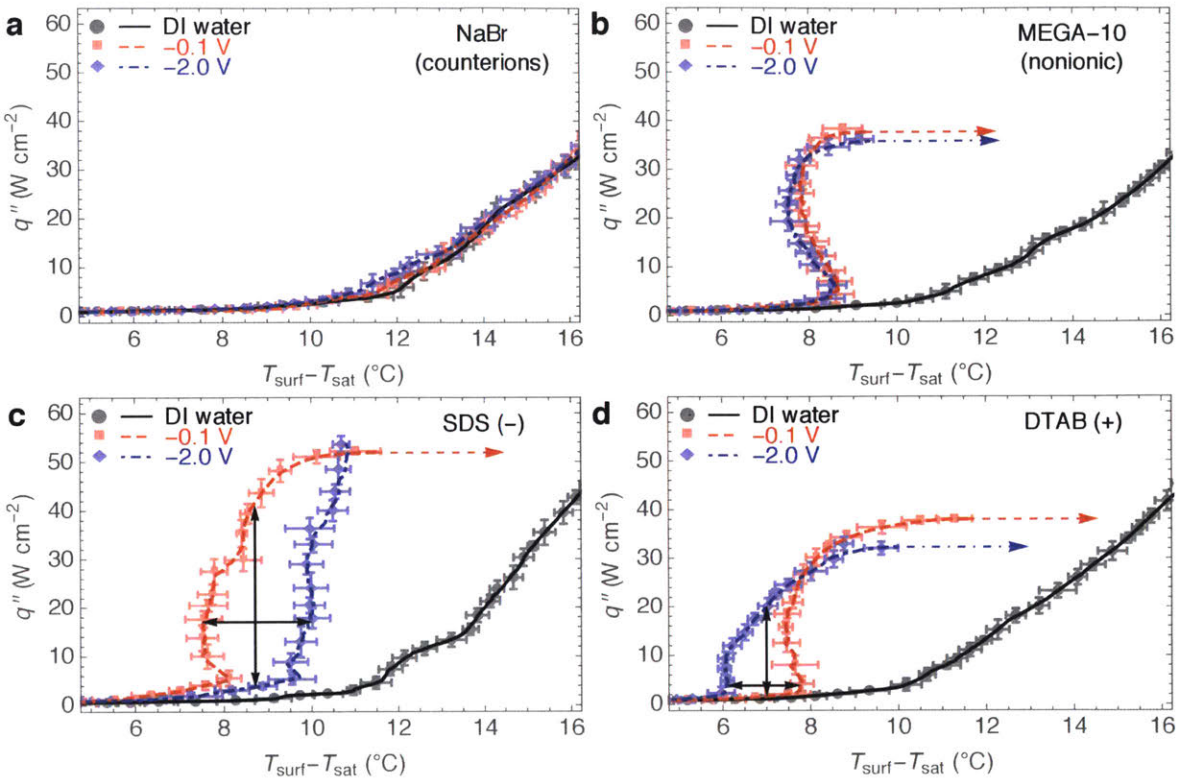

Figure 5-9: **Boiling curves showing tunability of charged surfactants.** Plain DI water (black), −0.1 V (red), and −2.0 V (blue) boiling curves for 2.6 mM (a) NaBr, (b) MEGA-10, (c) SDS, and (d) DTAB. Time-averaged data points from an individual boiling experiment with error bars (2 standard deviations in data spread from time averaging) and moving averages (lines) are shown. Boiling was not affected by voltage for (a) NaBr and (b) MEGA-10. For (c) negatively charged SDS, the boiling curve at −2.0 V was right-shifted with higher CHF compared to −0.1 V. For (d) positively charged DTAB, the boiling curve at −2.0 V was left-shifted with lower CHF compared to −0.1 V. The maximum change in HTC (tunability) at constant q'' (horizontal arrows) and constant superheat (vertical arrows) are shown for SDS and DTAB.

ure 5-9d show a high superheat on the −0.1 V curve of 7.8 °C and a low superheat on the −2.0 V curve of 6.1 °C. The ability to shift the boiling curve left and right as well as modify CHF enables modulation and optimization of performance for a variety of conditions. For instance in Figure 5-9d, the blue curve (−2.0 V) is more desirable at lower heat fluxes while the red curve (−0.1 V) is more desirable at higher heat fluxes (above the intersection of blue and red curves at 26 W cm^{-2}) owing to its higher CHF. This optimization scheme illustrates the opportunity to develop adaptable boiling devices.

5.3.5 Effects of concentration

Just as in surfactant boiling with no applied electric fields, concentration plays a large role with electric fields. The tuning effect was less pronounced at lower concentrations. This can be explained by the surface adsorption isotherm being monotonic where surface concentrations would be smaller at lower bulk concentrations [116, 117, 118], hence the change in initial contact angle would be minimal. In addition, lower concentration solutions are more electrically resistive, which would weaken the electric double layer effect (capacitive charging) due to an ohmic drop in the bulk. This ohmic drop may be quite significant as our testing has shown that tunability is dependent on counter electrode placement (more tunability was observed when the counter electrode was closer). The effect of concentration is also corroborated by superheat measurements of S10S at concentrations from 0 to 27 mM (see Figure 5-10), which show that the tunability effect becomes stronger with higher concentrations. As long as the concentration is below the CMC when the boiling

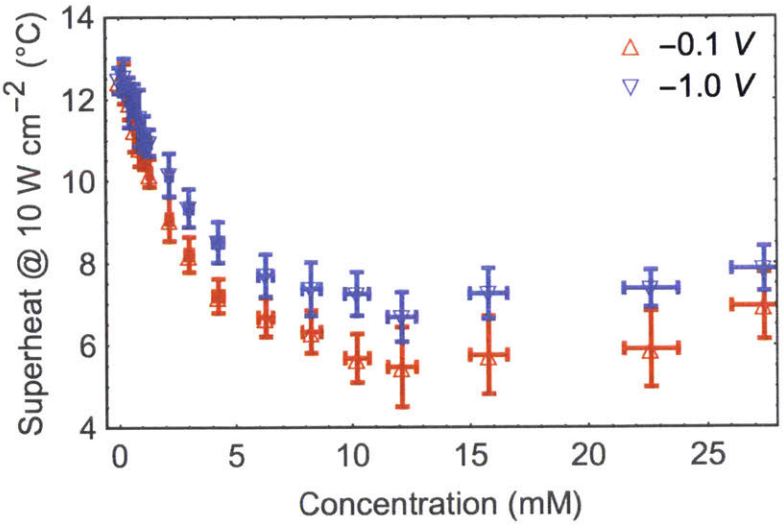

Figure 5-10: **Effect of concentration and electric potential on superheat (at 10 W cm^{-2}) for sodium decyl sulfate (S10S).** This was performed on the default silver boiling surface. The tunability effect (separation between −0.1 V and −2.0 V data points) is lower at low concentrations while plateauing at higher concentrations. This shows that the tunability effect is applicable for a wide range of concentrations as long as the concentration is below the CMC (38.1 mM for S10S). The uncertainty in concentration is ±5 % while the uncertainty in superheat is two standard deviations in variation due to time-averaging.

curve begins to shift right [41] (which is the case for all surfactants tested), we expect the field-induced tunability effect to occur.

5.3.6 Spatial control of boiling

Finally, we extended our approach to demonstrate both temporal and spatial control of boiling (Figure 5-11) based on our understanding of the mechanism. We fabricated a boiling surface with eight separately addressable gold electrodes[1] insulated from each other, which were heated by platinum resistive heaters underneath (Figure 5-11a). With 2.6 mM DTAB, potentials of these electrodes were switched between −0.1 V and −2.0 V. We considered −2.0 V the "on" state since positively charged DTAB would adsorb to the surface and increase nucleation compared to the −0.1 V "off" state. On the back side of each electrode, a relatively uniform heat flux (constant heater power) of approximately 1.5 W cm^{-2} was applied across the surface near the onset of bubble nucleation. Figure 5-11c-j shows our ability to selectively activate bubbles in the area limited to the "on" electrode and completely suppress bubbles at the "off" electrodes with sub-second precision.

5.4 Summary

The work in this Chapter demonstrates that accurate control of boiling is possible, spatially on the scale of a few millimeters and temporally in the sub-second range using charged surfactants with the application of an electric potential. Leveraging our knowledge about the importance of solid-liquid adsorption from the previous Chapters, we were able to recognize that electric fields could modulate and amplify the surfactant enhancement effect. First, we identified appropriate materials for the boiling surface and counter electrode given that chemical reactions and degradation of the system must be avoided. Then, we performed a series of experiments that verified and demonstrated the phenomenon. Our first tests showed that nucleation

[1] Gold was used over silver as it offered better adhesion during fabrication.

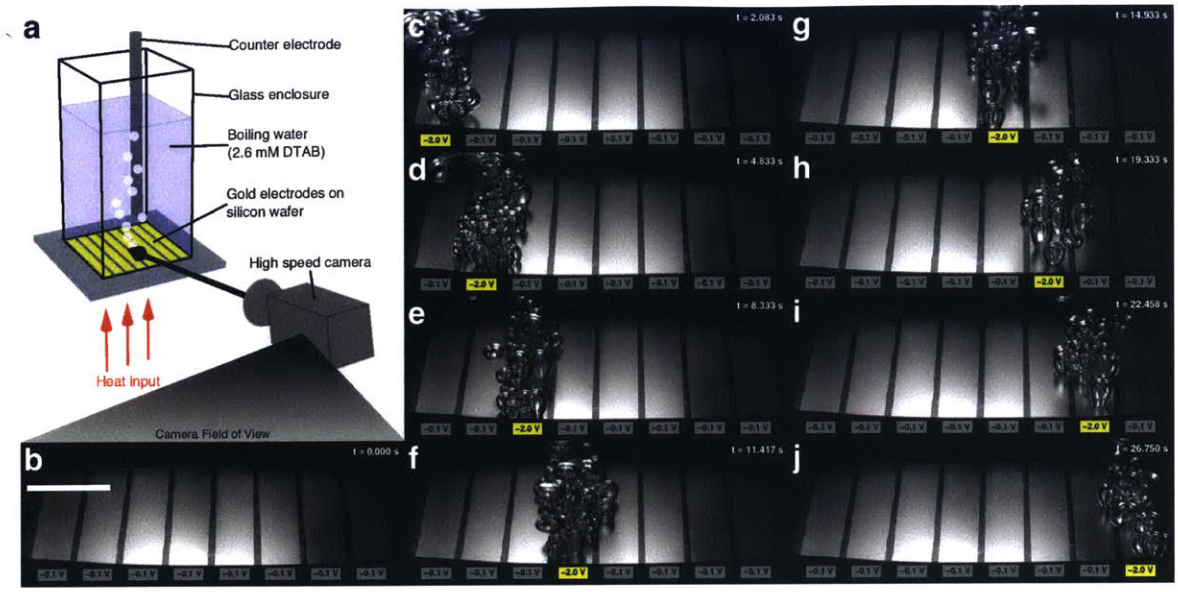

Figure 5-11: **Spatial and temporal control of boiling.** A solution of 2.6 mM DTAB (positively charged) in DI water was pool boiled in an experimental setup (a) where eight separate gold electrodes were switched between −2.0 V (yellow) and −0.1 V (gray) to turn on/off bubble nucleation. Images taken at different times with a high speed camera show (b) no nucleation of bubbles when no electrodes were activated, and (c-j) bubble nucleation only on the particular electrode that was activated. The scale bar is 1 cm.

could be turned on and off. Then, we performed square-wave and triangle-wave potential experiments verifying that capacitance (solid-liquid adsorption) was responsible for changes in temperature and HTC, with an ordinary salt and nonionic surfactant acting as controls. Measured boiling curves corroborated these findings and we demonstrated the ability to change the boiling curve with the applied potential for higher HTC or higher CHF. Surfactant concentration was also investigated and we found that tunability tends to increase at higher concentrations. Finally, we showed the ability to control nucleation in a spatial manner. The results of this particular study can have some significant implications on improving existing systems as well as ushering in novel applications as will be discussed in our concluding Chapter 6.

CHAPTER 6

CLOSING REMARKS

6.1 Thesis summary

The goal of this thesis is to uncover the mechanism of surfactant enhanced boiling, which is a phenomenon known since the early part of the 20th century [41, 42]. Despite decades of research in this area in the past, it was difficult to say how exactly surfactants are aiding in enhancement or what kinds of surfactants would be ideal. However, significant advances in our understanding of boiling physics and surfactant science in the past few decades have gotten us closer to a full understanding. In this thesis, we have tackled the problem from the ground up by first developing an understanding of molecular behavior, and then connecting that to macroscopic boiling behavior. In essence, we have built a framework of models, based on relevant physics and size scales, and verified those models via appropriate experiments detailed in Chapter 2.

At the molecular level, we developed a model to predict surface tension using molecular parameters as inputs. The latter part is key since this would help us to identify or design appropriate surfactants depending on the application. To do so, we leveraged previous undertakings of this problem by Nikas et al. [73] and

Mulqueen et al. [74, 75], and based the root of our modeling framework on statistical mechanics. From here, an equilibrium surface tension model was developed and verified. Then, that equilibrium surface tension model was input into existing theory of dynamic surface tension. The results of the dynamic surface tension model were also experimentally verified. This gave us the ability to predict how an arbitrary, alkyl-terminated surfactant would affect interfacial properties of water, as a function of time.

In boiling, which is a highly dynamic process, bubbles continuously nucleate, grow, and depart. Thus, surfactants can significantly complicate the problem because they introduce time dependencies of physical properties. But, with molecular models that describe these time-dependent properties, we could begin to dissect the details of boiling. We examined nucleation, working upon previous theories of how bubbles grow from cavities by Hsu [97] and Lorenz [99], we recognized the importance of using the Clausius-Clapeyron relation to account for nucleation enhancement. We looked at bubble growth, and modified existing growth descriptions by Plesset and Zwick and [101] and Mikic et al. [106] to account for effects of the thermal boundary layer, in addition to time-dependent interfacial properties. Then, we offered a new perspective and method of calculating bubble departure based on growth behavior and interfacial properties. This provides an analytical way to understand and summarize many valuable numerical simulation studies that investigated the behavior of single bubbles [102, 103, 104, 51, 105]. With this single-bubble model, we were then able to account for both horizontal and vertical shifts in the boiling curve in the presence of any arbitrary alkyl-terminated surfactant. Thus, we are able to predict a boiling curve for any surface and surfactant as long as a reference boiling curve is known. The results of our boiling curve prediction have general agreement with experimental results and allowed us to gain some additional insight. We found that solid-liquid adsorption is primarily responsible for any enhancement due to enhanced nucleation while liquid-vapor adsorption only reduces performances due to smaller bubble sizes (less heat transfer per bubble cycle) and bubble-crowding effects. We also found that large-head, low-CMC surfactants would

be ideal for most applications. Furthermore, we discovered that small potentials innate to a metal surface could affect the boiling performance of charged surfactants significantly and this directed us towards a unique method of boiling enhancement.

Recognizing that electric fields could alter the adsorption of surfactants to the solid surface, and that solid-liquid adsorption is primarily responsible for boiling enhancement, we discovered that applying electric fields with charged surfactants can significantly affect boiling behavior and performance. Applied potentials can modify the adsorption of surfactants on solid-liquid interfaces, which alters the hydrophobicity and nucleation behavior, thereby enabling *active control* of boiling. In essence, boiling could be turned "on" and "off" with a flick of a switch. We verified the phenomenon with a series of controlled experiments. Finally, we presented a boiling surface which can be actively controlled *spatially* in addition to temporally.

6.2 Contributions

In this work, we have made the following specific contributions to the research community.

- A methodology in which to perform clean contact angle measurements of a pendant bubble under a surface with minimal presence of contaminants. In particular, the role of contaminants on novel surfaces in recent years has been a subject of debate [53]. Thus, providing a simple way to perform cleaner wetting experiments would be valuable.

- A predictive equilibrium surface tension model for nonionic and ionic alkyl-terminated surfactants. Like other models [73, 74, 75], it is based on molecular parameters. In contrast to other models, this only requires a single parameter for an entire family of surfactants and many other thermodynamic potentials can be calculated. For the wide variety of applications where surfactants are used for their surface tension-lowering behavior, such as in oil and gas industries [119], food [120], and consumer products [121], a more

predictive model can better aid in design and selection of application-specific surfactants.

- A method in which to calculate the diffusion constant of alkyl-terminated surfactants. Suitable diffusion constants are often difficult to obtain. Thus, this method could be useful where modeling or understanding the transport of surfactants is required.

- A slightly modified equation of dynamic surface tension based on Diamant's [92] to account for EDL effects. With this equation, the dynamic surface tension of ionic surfactants can be calculated.

- A new cavity model description based on that of Hsu [97] and Lorenz [99] which provides more physical results. This could be valuable to boiling surface engineering endeavors.

- An expanded model of bubble growth based on the work of Plesset and Zwick and [101] and Mikic et al. [106] that takes into account the effect of a thin thermal boundary layer and the non-sphericity of the bubble. For pure liquids, a simple analytical equation is presented (Eq. 4.25). The lack of a model in this context relevant to boiling has been cited as one of the reasons researchers have undertaken computer simulation studies of single bubbles [51, 102]. Furthermore, this model is able to take into account time-dependent wetting properties, which we can calculate from molecular parameters.

- A new physical insight into bubble departure based on a constant momentum force and a method in which to calculate bubble departure from bubble growth behavior and molecular parameter-resolved, time-dependent interfacial properties. Bubble departure behavior dictates the heat transfer performance in boiling.

- A novel strategy to actively control boiling both temporally and spatially by using charged surfactants and low electric potentials. We have also provided guidelines to select appropriate materials to avoid corrosion.

6.3 Future work

While many future directions could be taken from this work, we will discuss four in particular that would be valuable for heat-transfer science and industry. First, our modeling of single-bubble behavior largely based on scaling and correlation was validated by numerical simulation studies in the absence of surfactants [102, 103, 104, 51, 105]. While CFD with interface-tracking in the presence of soluble surfactants and its associated Marangoni effects have been demonstrated before [122], no study has looked at bubble growth and departure behavior in the presence of surfactants and a thermal boundary layer. Furthermore, analysis of the relevant forces acting near the bubble base in a numerical simulation would provide additional insight into the departure mechanism. Numerical simulation results could also be compared with experiments on a single artificial cavity (fabricated using DRIE [105]) and heat transfer could be analyzed using the latest IR thermography techniques [123, 124] as single-bubble experimental studies in the presence of surfactants also have not been performed previously.

Second, the effects of bubbles in proximity and non-coalescence behavior could be investigated via simulation and experiment. The modeling framework presented in this thesis assumes that bubbles do not interact with each other; however, we should expect that a deviation from this ideality should occur as nucleation density and surfactant concentration increase due to bubble-crowding effects. These effects, if well controlled in simulation and experiment, could be correlated with nucleation density. For instance, it may be possible to modify the Mikic-Rohsenow (Eq. 4.35) model [96] such that

$$q'' = f_{\text{crowd}} n q_{\text{single}} \tag{6.1}$$

where f_{crowd} is a correction factor that depends on nucleation density, n, and surfactant concentration and type. It should be unity in the ideal, isolated bubble case and should diminish as bubble-crowding effects increase. Further understanding of bubble-crowding effects could also lead to a description of CHF with surfactants.

Third, utilizing the best of state-of-the-art boiling surfaces that offer extremely

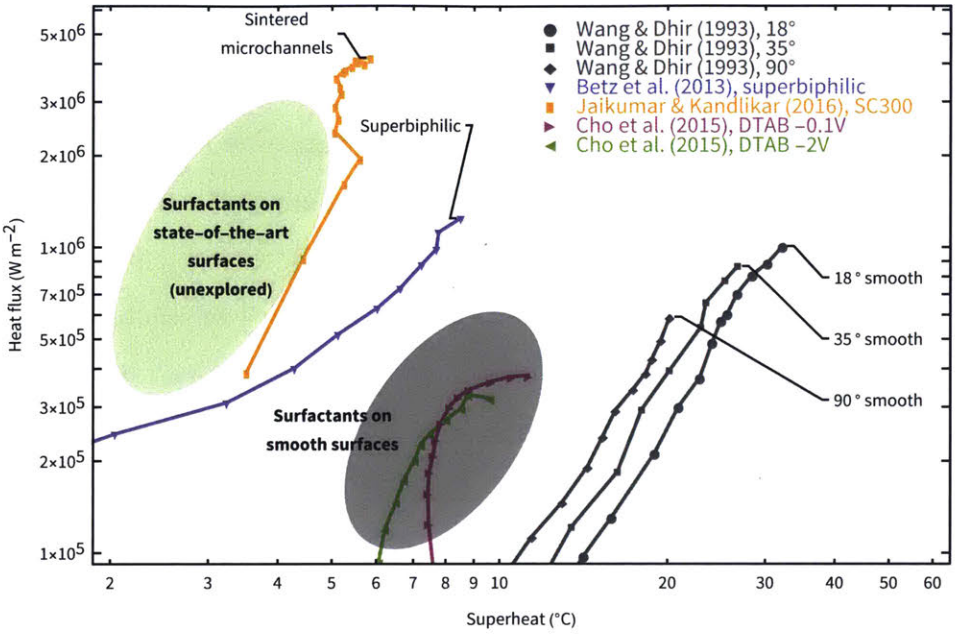

Figure 6-1: **Potential performance of state-of-the-art boiling surfaces with surfactants.** Boiling curves of smooth (gray points) [17] and state-of the-art (red, blue, orange points) surfaces [37, 38]. Surfactants applied to smooth surfaces have enhanced HTC (gray ellipse). Surfactants applied to state-of-the-art surfaces could potentially have even higher HTC and CHF (green ellipse) [39].

high HTC and CHF (often several hundred W cm^{-2} at a few degrees superheat [31]) with surfactants could push HTC even higher. Some of the latest surfaces [38, 35] have separate liquid and vapor pathways spaced millimeters apart. Since bubble nucleation under the vapor pathways is still dictated by conventional nucleation theory, surfactants could provide a further left-shift of the boiling curve as shown in Figure 6-1.

Finally, a study of long-term performance and robustness of surfactants under various boiling conditions should be taken. While all boiling experiments in this thesis were performed at ambient conditions (100 °C boiling point), many industrial boilers might operate at elevated conditions closer to the critical point of water (374 °C) where thermal degradation effects could occur. Thus, the use of fluorocarbon surfactants, which have shown temperature resistance up to 600 °C [125], could be promising.

6.4 Implications

With the framework presented in this thesis, it is now possible to make more informed decisions about which surfactants to use in boiling applications. Hopefully, this can lead to further consideration and adoption of surfactants in thermal systems as significant performance gains can be made with just a small amount of surfactant. In essence, the framework can be used as a design tool whereas none existed before. In other boiling applications where surfactants may naturally be present such as distillation and purification, this framework could lead to better understanding and control.

Further control is possible with charged surfactants and electric fields. Fundamentally, this could aid in the evolution of thermal devices from simple passive devices (as they are mostly used today) to actively controlled ones (Figure 6-2). Passive devices act analogously to an electrical resistor; the development of the transistor, which enabled control of current with an external voltage led to massive developments in electrical engineering and computing that ushered in the Information Age. Today, we live in a much more energy-conscious society given the ubiquity of high-energy-density electronics in daily life and the impact our devices and energy sources can have on Earth and its climate. As such, energy devices from large-scale power plants to portable electronics can benefit from smart control of heat.

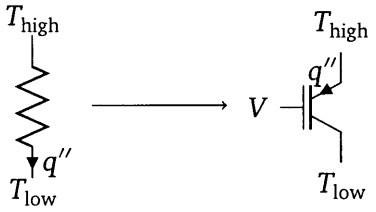

Figure 6-2: **Evolution of thermal devices from having passive resistor-like behavior to active transistor-like behavior.**

The increasing diversity of our energy sources and devices is necessitating the development or improvement of boiling processes that might operate in a non-steady manner or in changing conditions. In dispatchable power stations, which need to be

switched on and off rapidly in response to changing electricity demand, surfactants under electric fields could aid in startup times and efficiency by initiating nucleation earlier. New solar steam generation approaches often try to maximize evaporation with minimal heat fluxes [12]; thus, enhanced nucleation would be beneficial. In electronics cooling, the ability to dissipate more heat can offer significant gains in chip performance and reliability. Currently, phase-change processes have not gained broad adoption in electronics thermal management, which could be due to its difficulty of control and unpredictability [126]. Spatial and temporal control offered by a device similar to ours could provide the required control and predictability of heat transfer on targeted "hot spots" in electronics as well as improved stability in flow boiling which can be highly sensitive to the location of bubble nucleation [127].

Whether surfactant boiling can address the specific challenges described above or not, we emphasize the need to understand the phenomena from a molecular perspective. This is because much of the potential of developing or improving phase change technologies lies in how far we can harness the behavior of a vast array of chemicals and size scales. Hence, in this thesis, from tunable boiling surfaces, to boiling curves, to single bubbles, to interfacial properties, we have involved our intuition of molecular behavior at every step of the way.

APPENDIX A

ADDITIONAL DATA

A.1 Pool boiling data

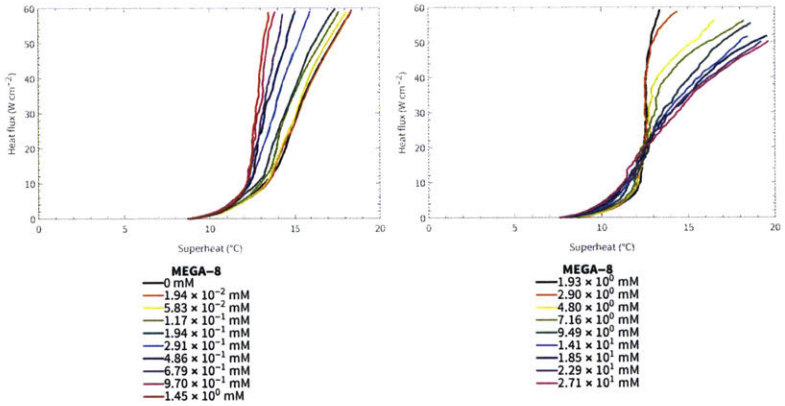

Figure A-1: **MEGA-8 pool boiling curves on a gold surface.** Experimental pool boiling curves were obtained as described in Section 2.2.

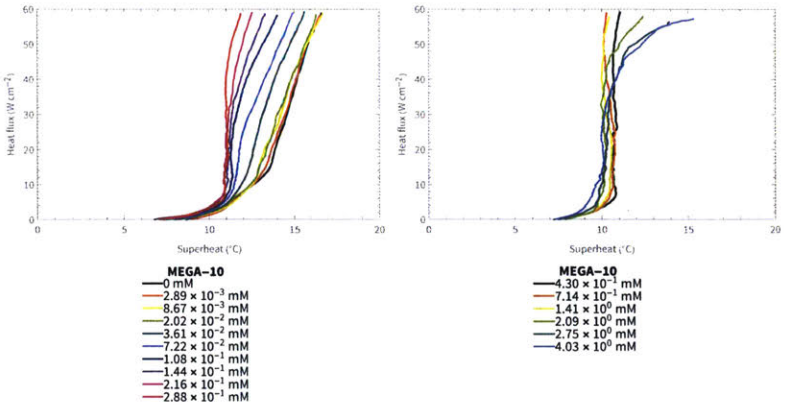

Figure A-2: **MEGA-10 pool boiling curves on a gold surface.** Experimental pool boiling curves were obtained as described in Section 2.2.

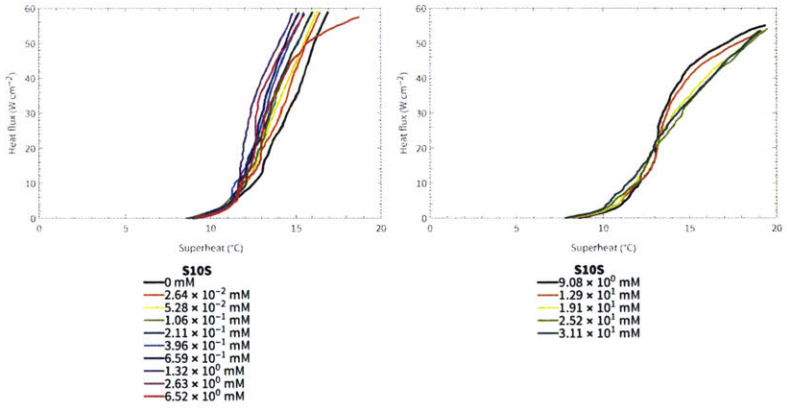

Figure A-3: **S10S pool boiling curves on a gold surface.** Experimental pool boiling curves were obtained as described in Section 2.2.

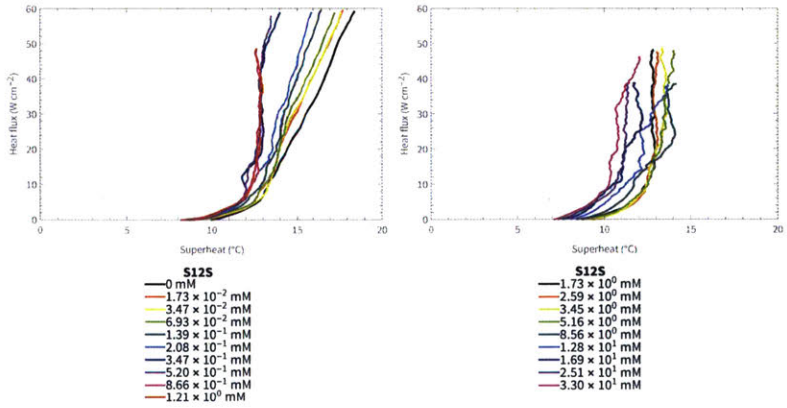

Figure A-4: **S12S pool boiling curves on a gold surface.** Experimental pool boiling curves were obtained as described in Section 2.2.

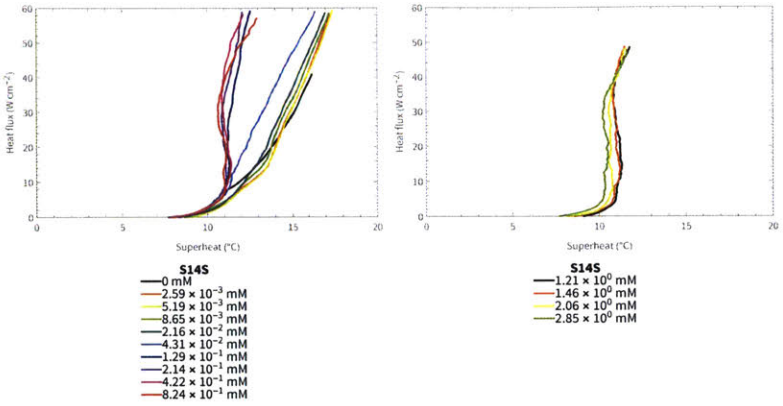

Figure A-5: **S14S pool boiling curves on a gold surface.** Experimental pool boiling curves were obtained as described in Section 2.2.

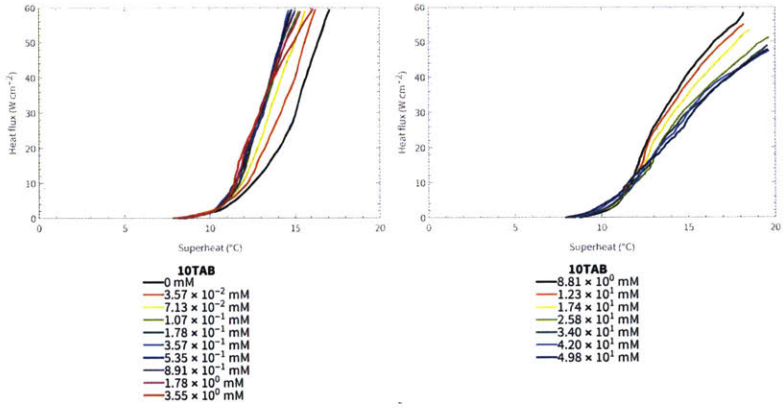

Figure A-6: **10TAB pool boiling curves on a gold surface.** Experimental pool boiling curves were obtained as described in Section 2.2.

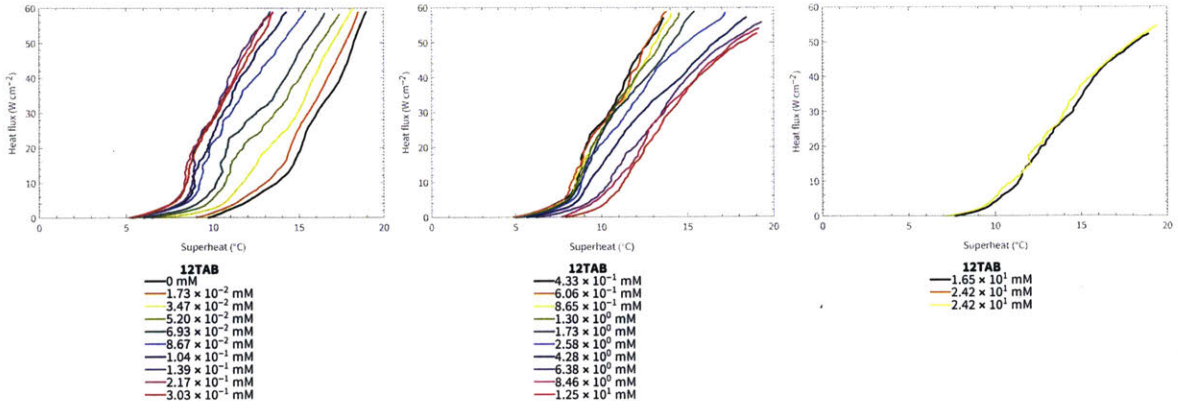

Figure A-7: **12TAB pool boiling curves on a gold surface.** Experimental pool boiling curves were obtained as described in Section 2.2.

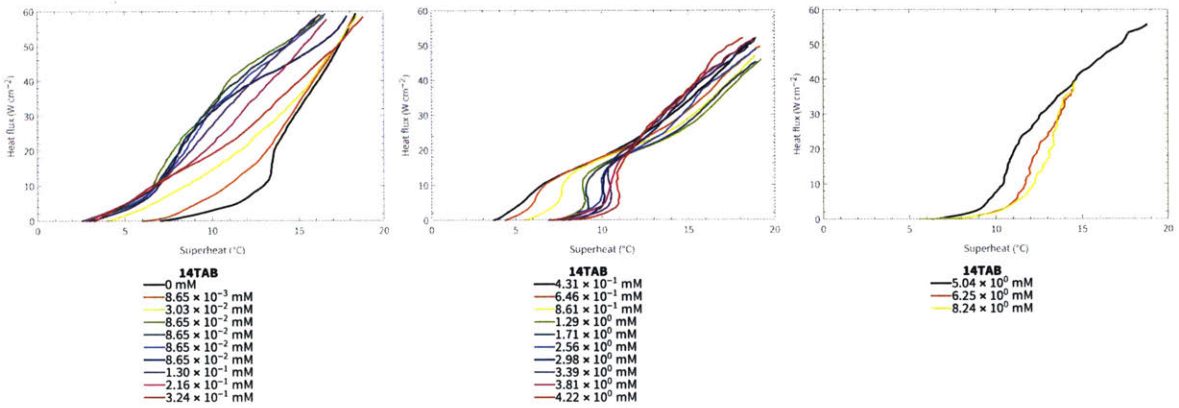

Figure A-8: **14TAB pool boiling curves on a gold surface.** Experimental pool boiling curves were obtained as described in Section 2.2.

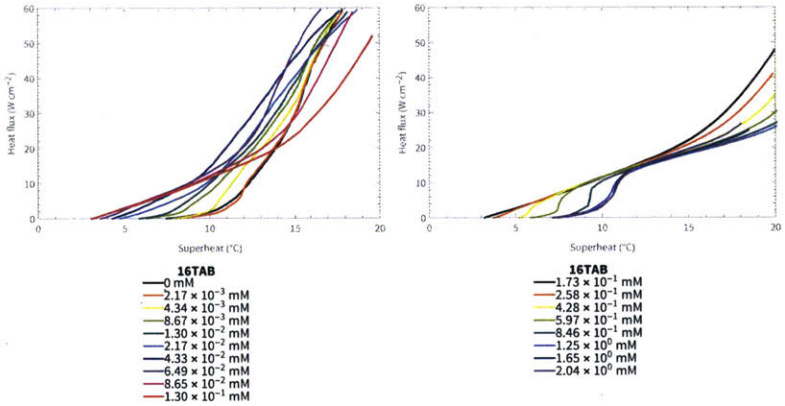

Figure A-9: **16TAB pool boiling curves on a gold surface.** Experimental pool boiling curves were obtained as described in Section 2.2.

A.2 Equilibrium wetting data

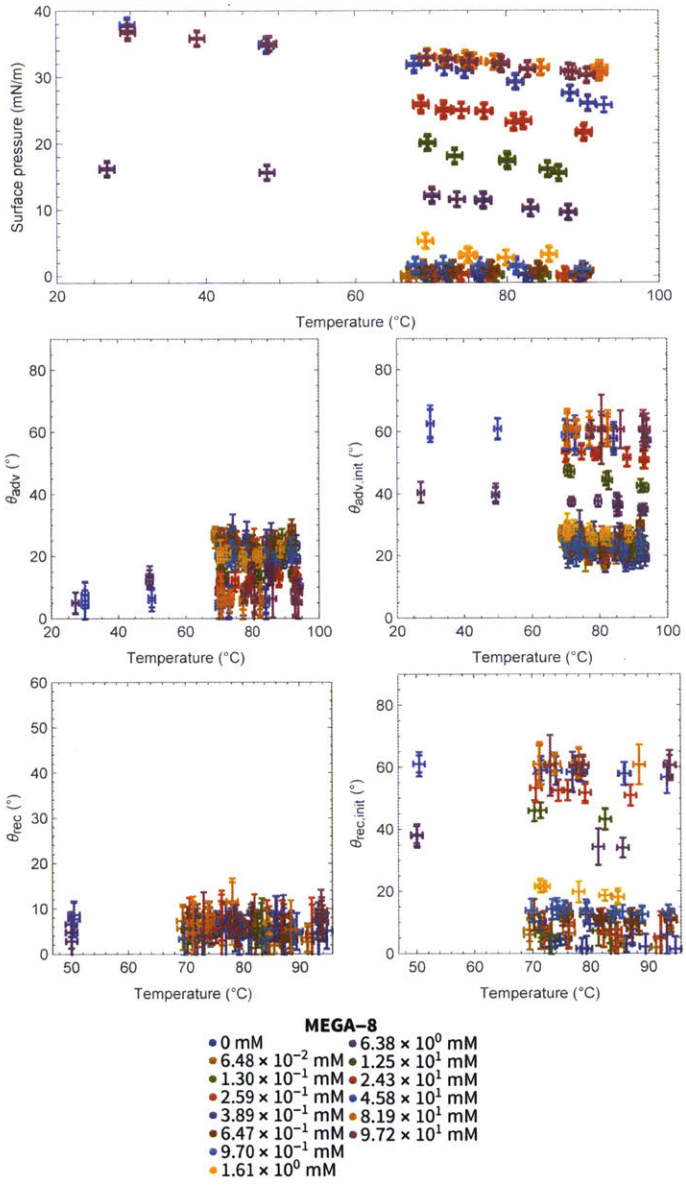

Figure A-10: **MEGA-8 surface pressure and contact angles on a gold surface.** Surface pressure measurements were obtained as described in Section 2.3.2. Advancing and receding contact angles were obtained as described in Section 2.3.4.

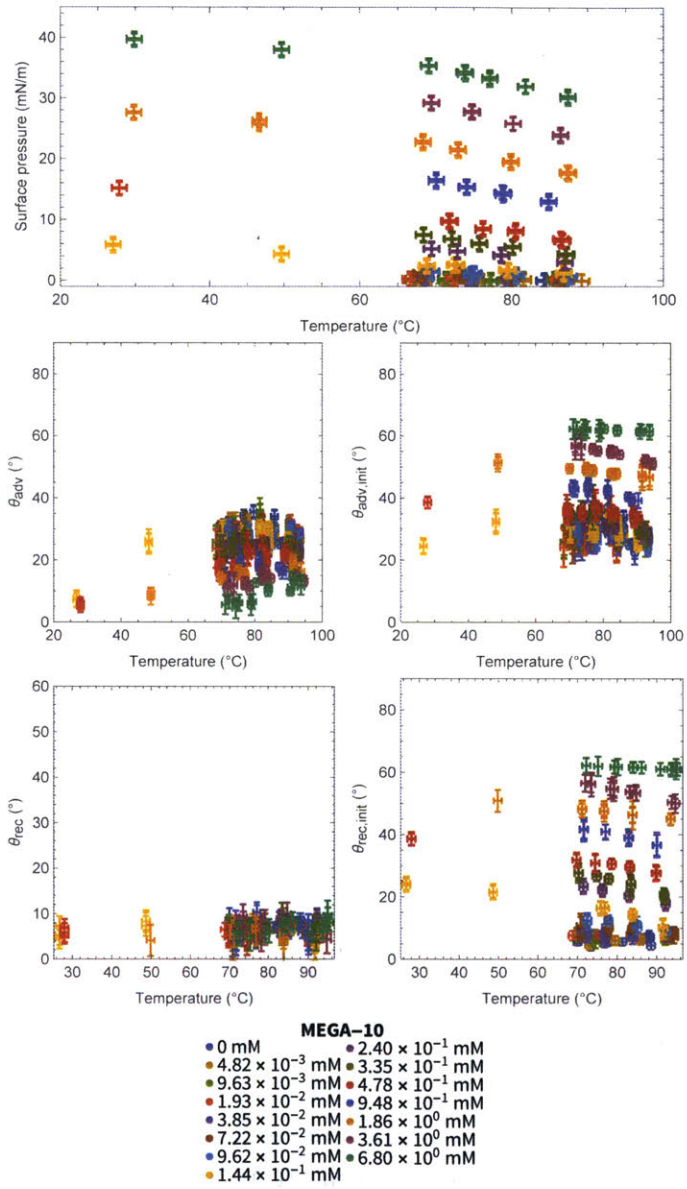

Figure A-11: **MEGA-10 surface pressure and contact angles on a gold surface.** Surface pressure measurements were obtained as described in Section 2.3.2. Advancing and receding contact angles were obtained as described in Section 2.3.4.

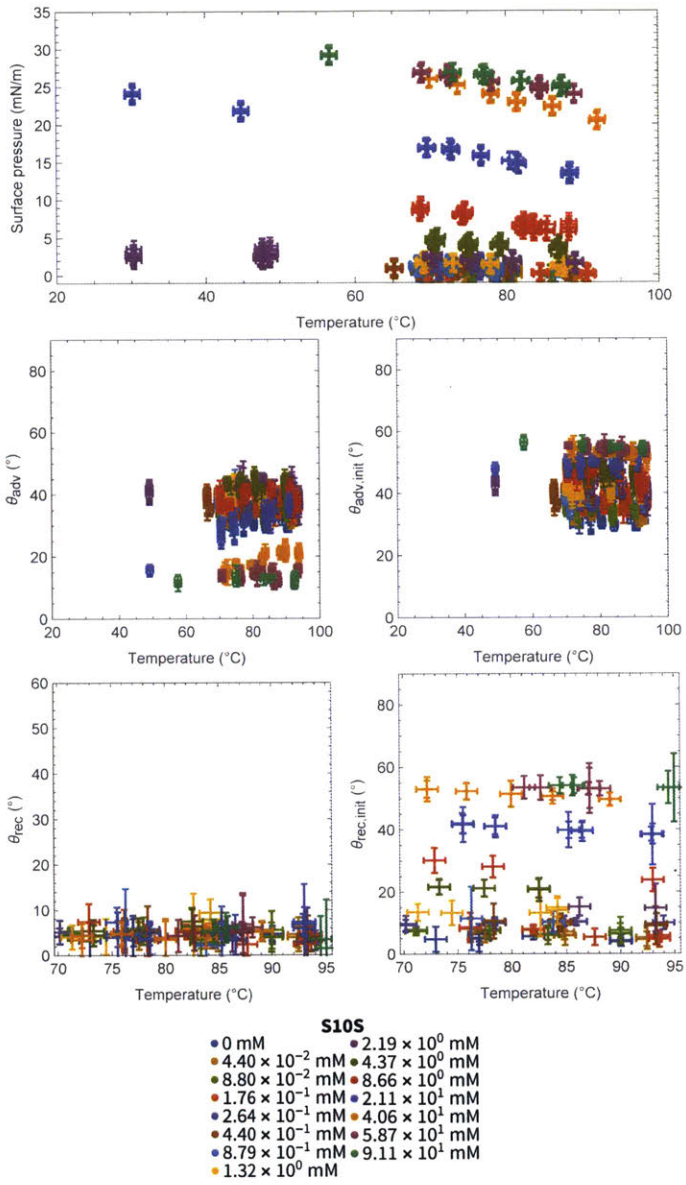

Figure A-12: **S10S surface pressure and contact angles on a gold surface.** Surface pressure measurements were obtained as described in Section 2.3.2. Advancing and receding contact angles were obtained as described in Section 2.3.4.

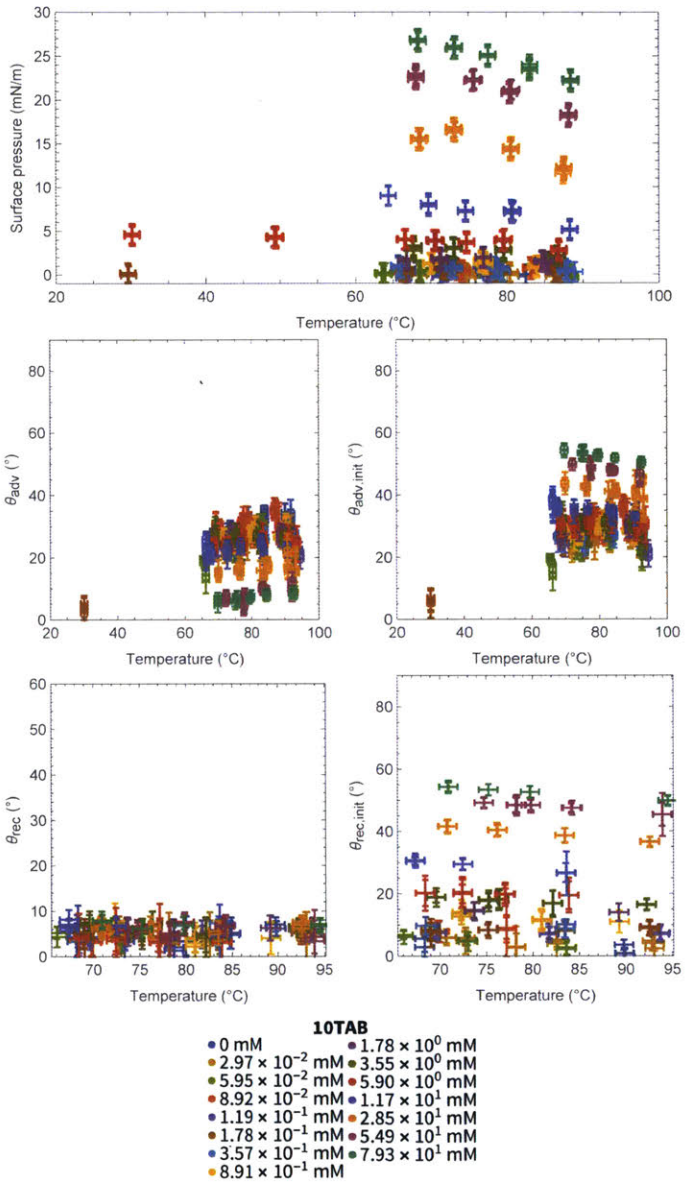

Figure A-13: **10TAB surface pressure and contact angles on a gold surface.** Surface pressure measurements were obtained as described in Section 2.3.2. Advancing and receding contact angles were obtained as described in Section 2.3.4.

A.3 Dynamic surface tension data

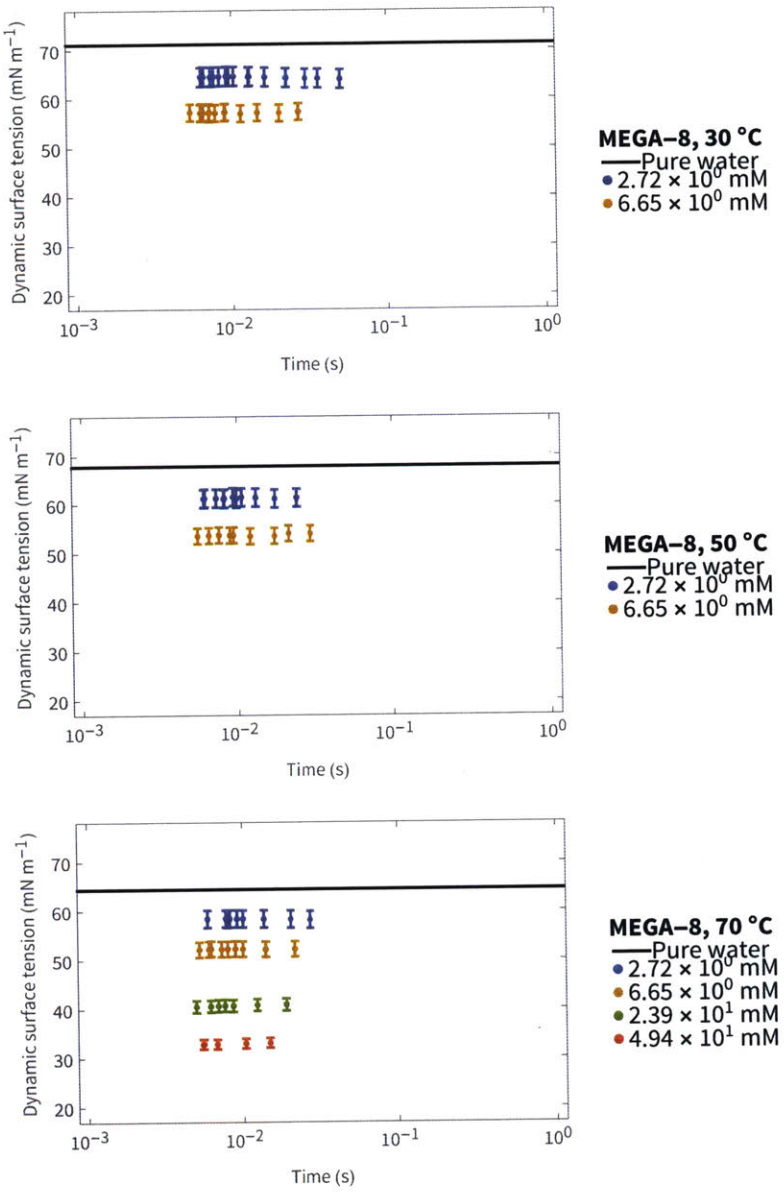

Figure A-14: **MEGA-8 dynamic surface tension data.** Dynamic surface tension data was obtained as described in Section 2.3.3.

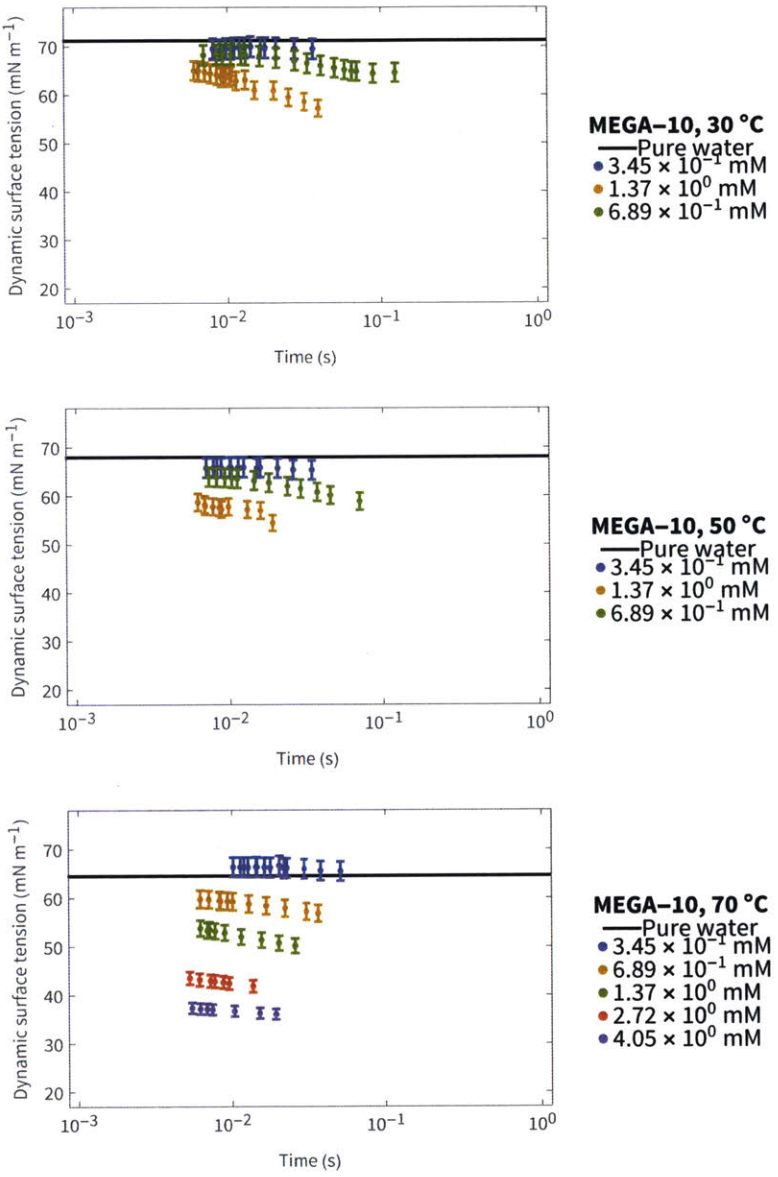

Figure A-15: **MEGA-10 dynamic surface tension data.** Dynamic surface tension data was obtained as described in Section 2.3.3.

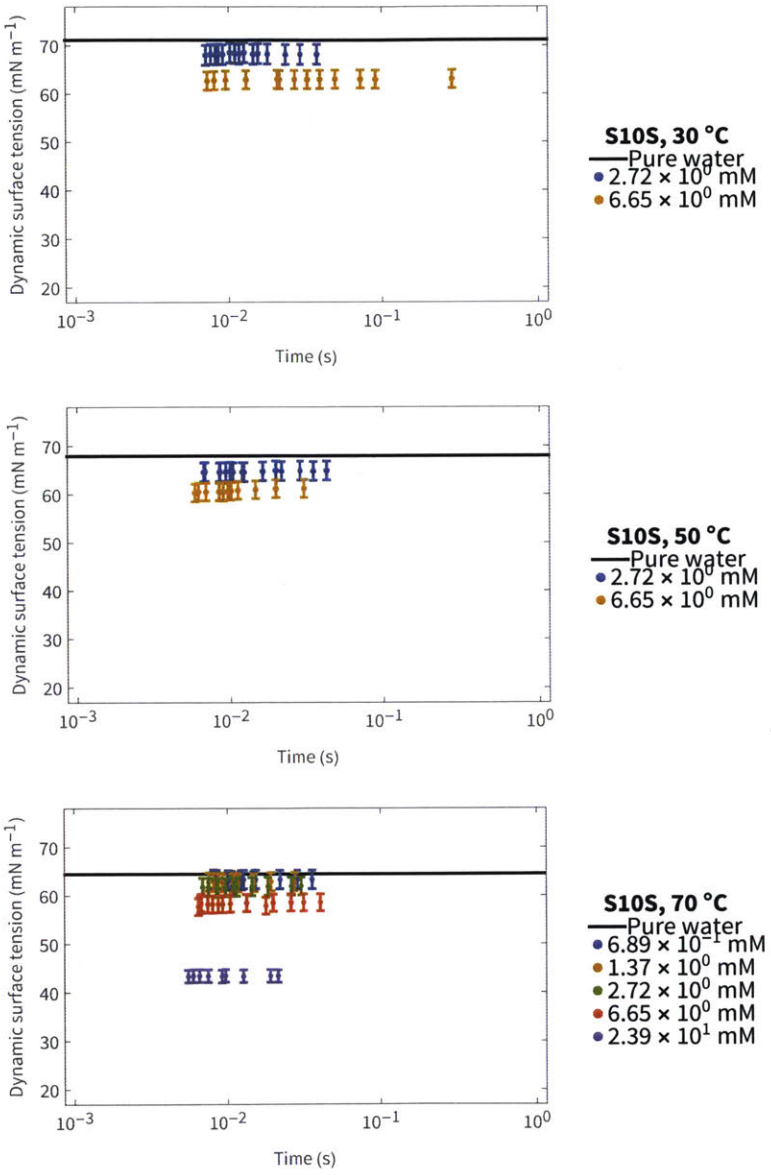

Figure A-16: **S10S dynamic surface tension data.** Dynamic surface tension data was obtained as described in Section 2.3.3.

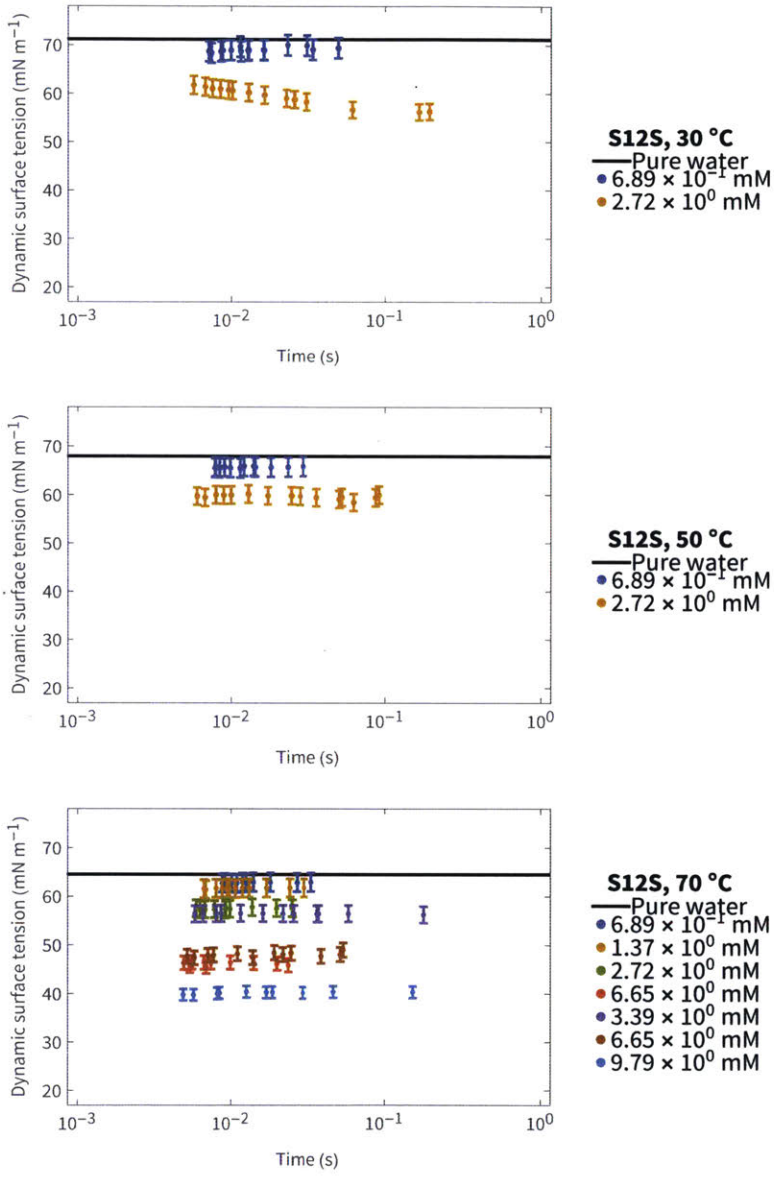

Figure A-17: **S12S dynamic surface tension data.** Dynamic surface tension data was obtained as described in Section 2.3.3.

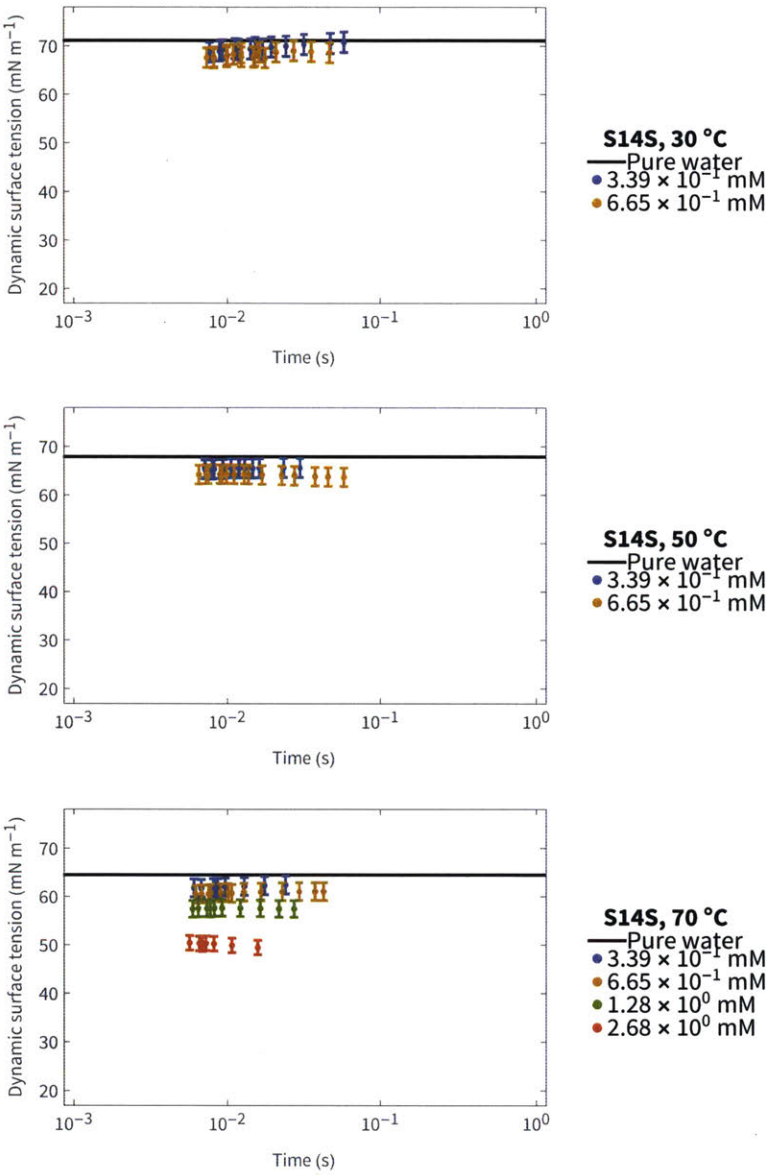

Figure A-18: **S14S dynamic surface tension data.** Dynamic surface tension data was obtained as described in Section 2.3.3.

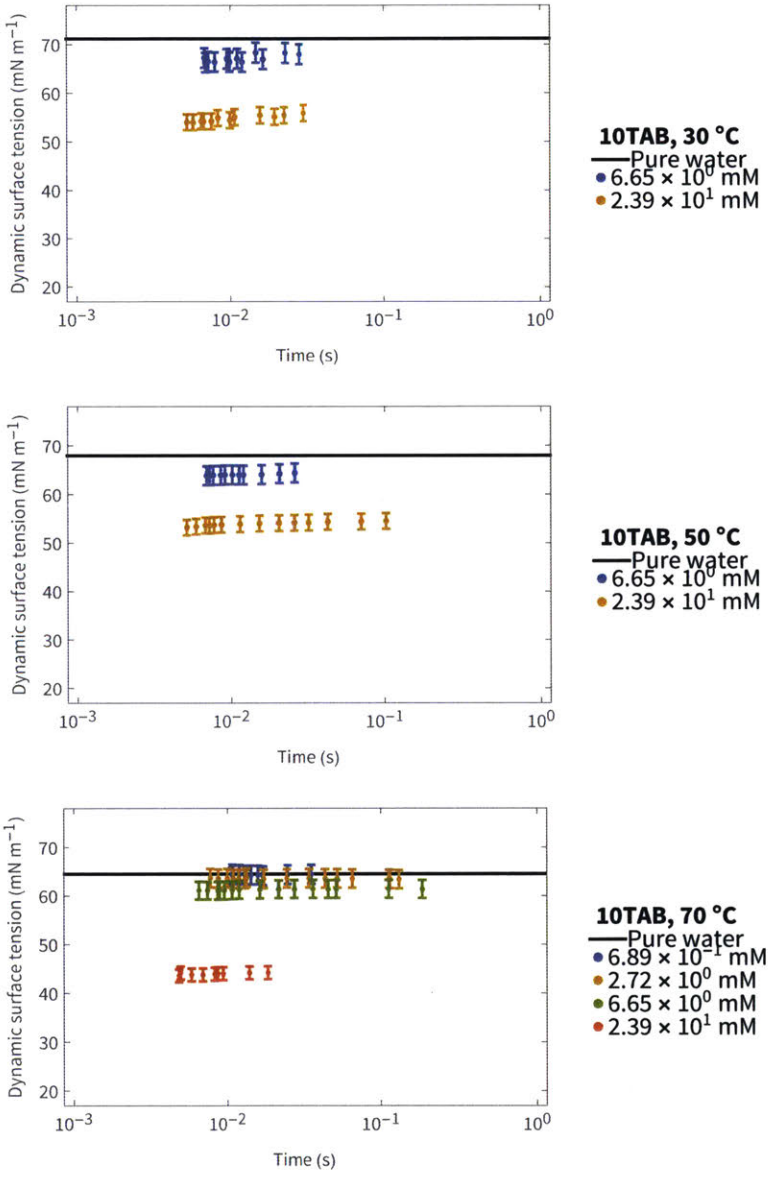

Figure A-19: **10TAB dynamic surface tension data.** Dynamic surface tension data was obtained as described in Section 2.3.3.

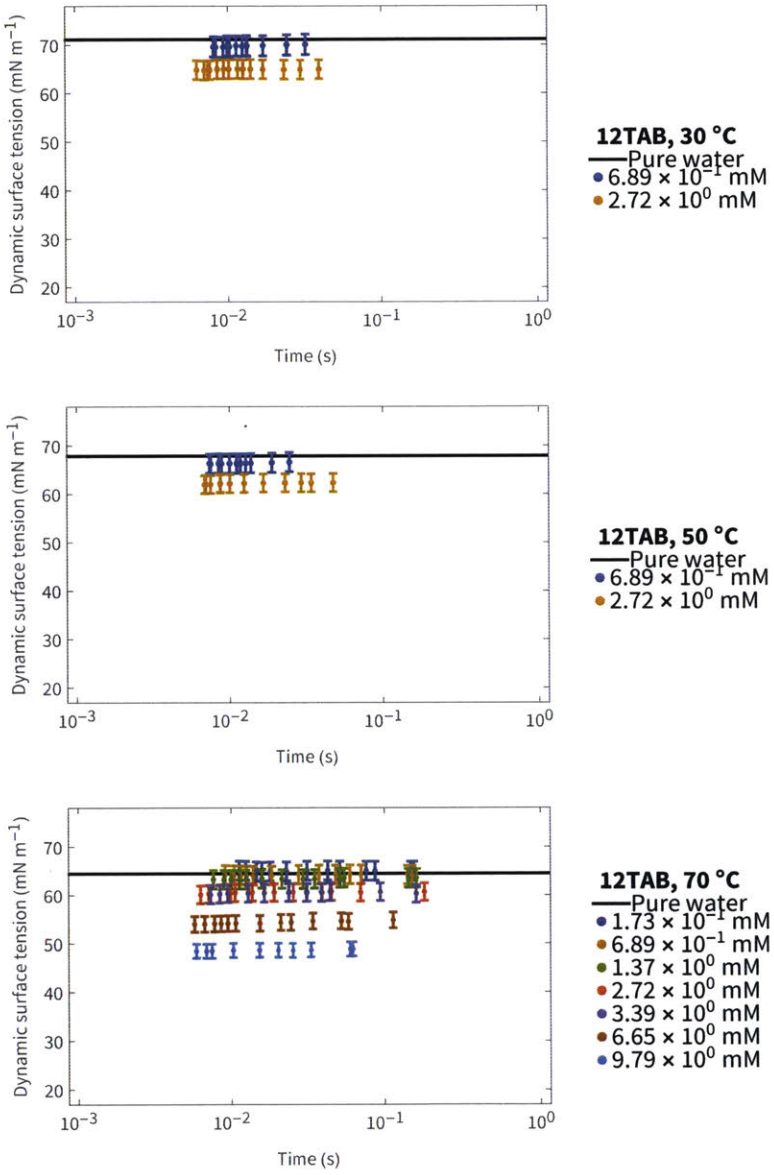

Figure A-20: **12TAB dynamic surface tension data.** Dynamic surface tension data was obtained as described in Section 2.3.3.

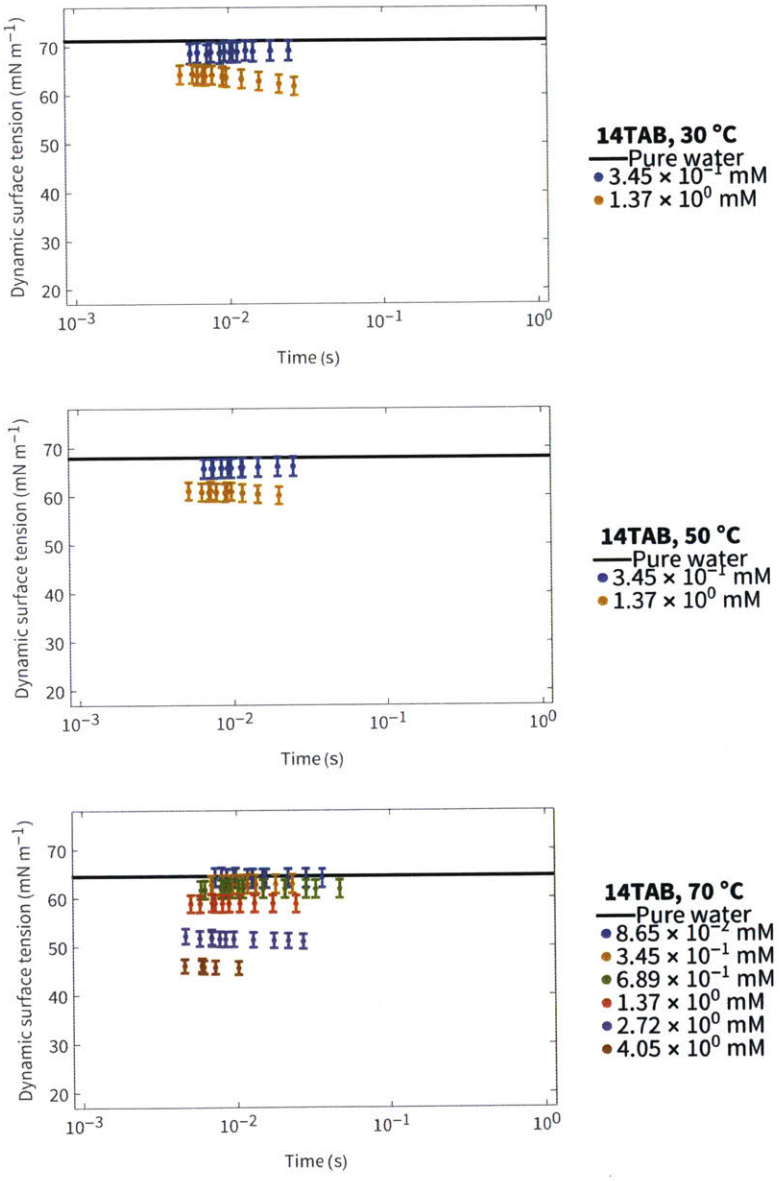

Figure A-21: **14TAB dynamic surface tension data.** Dynamic surface tension data was obtained as described in Section 2.3.3.

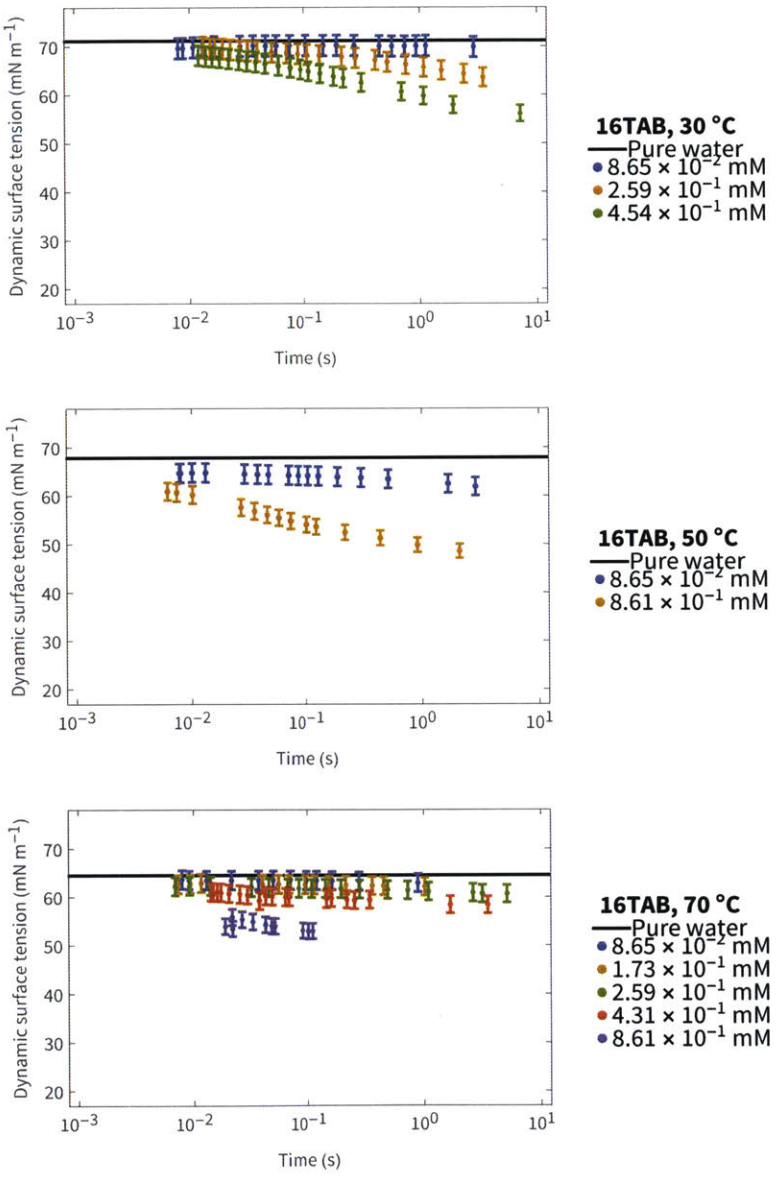

Figure A-22: **16TAB dynamic surface tension data.** Dynamic surface tension data was obtained as described in Section 2.3.3.

APPENDIX B

GENERAL THERMODYNAMIC CONCEPTS

Here, we will derive some basic thermodynamic concepts that are *always* true such as internal energy, the state of equilibrium, and the general definition of chemical potential. We will also show a general equation of surface tension as it relates to the chemical potential.

B.1 Euler equation of internal energy

Internal energy, or energy in its purest sense, is a fundamental quantity in physics and takes many forms. We often discuss energy in terms of thermal, mechanical, or chemical quantities. In this Section, we will show how these quantities relate to energy mathematically.

B.1.1 Mathematical derivation

First, consider a first-order homogenous equation, i.e. something that satisfies

$$f(\lambda X_1, \lambda X_2, \ldots, \lambda X_n) = \lambda f(X_1, X_2, \ldots, X_n) \tag{B.1}$$

We can think of X_1, X_2, etc. as being extensive variables like S, V, and N and the function, f, as total energy U. Thus, $f(X_1,X_2,X_3)$ is like $U(S,V,N)$. If we have some isotropic thermodynamic body with uniform intensive properties (like T, P, and μ) and we double the entropy, volume, and number of particles, then we should expect the energy to double ($U(2S,2V,2N) = 2U(S,V,N)$), which is exactly what Eq. B.1 states. Thus, internal energy is a first-order homogenous function of S, V, N and any other *independent* extensive variable that can describe the system. Then, according to Euler's homogeneous function theorem,[1] the following must be true:

$$f(X_1,X_2,\ldots,X_n) = X_1\frac{\partial f}{\partial X_1} + X_2\frac{\partial f}{\partial X_2} + \ldots + X_n\frac{\partial f}{\partial X_n}. \tag{B.2}$$

The partial derivatives relate two extensive variables yielding intensive quantities. If we substitute U, S, V, and N for f, X_1, X_2, and X_3, the partial derivatives become $\partial U/\partial S$, $\partial U/\partial V$, and $\partial U/\partial N$, which are T, $-P$, and μ respectively. So, from Eq. B.2 we arrive at the Euler equation:

$$\boxed{U = TS - PV + \mu N}. \tag{B.3}$$

B.1.2 Physical derivation

Salzman provides another more physical way of understanding this result [128]. Imagine we have a system in one container and we transfer it to another container one differential drop at a time while holding all intensive variables (T, P, and μ in this case) constant. We can parametrize this process with a variable, x, where $0 \leq x \leq 1$. When $x = 0$, everything is in the original container, and when $x = 1$, everything has been transferred to the new container. Since the change in an extensive quantity should be directly proportional to the size of the droplet, dx, we

[1] The generic theorem states that for a homogeneous function $f(\mathbf{X})$ with order k and $\lambda > 0$ such that $f(\lambda\mathbf{X}) = \lambda^k f(\mathbf{X})$, then $\mathbf{X}\cdot\nabla f(\mathbf{X}) = kf(\mathbf{X})$.

can parameterize the differential changes in U, S, V, and N in terms of x.

$$dU_{\text{new}} = U_{\text{tot}} dx$$
$$dS_{\text{new}} = S_{\text{tot}} dx$$
$$dV_{\text{new}} = V_{\text{tot}} dx$$
$$dN_{\text{new}} = N_{\text{tot}} dx$$

Here, the control volume is the new container, and U_{tot}, S_{tot}, V_{tot}, N_{tot} refer to the total quantities in the original and new containers. The differential change in U_{new} should be

$$dU_{\text{new}} = \frac{\partial U_{\text{new}}}{\partial S_{\text{new}}} dS_{\text{new}} + \frac{\partial U_{\text{new}}}{\partial V_{\text{new}}} dV_{\text{new}} + \frac{\partial U_{\text{new}}}{\partial N_{\text{new}}} dN_{\text{new}}.$$

Plugging in the definitions of T, P, and μ for the partial derivatives we obtain

$$dU_{\text{new}} = T dS_{\text{new}} - P dV_{\text{new}} + \mu dN_{\text{new}}.$$

Now, substituting what we know about dU_{new}, dS_{new}, dV_{new}, and dN_{new} in relation to their total quantities, we obtain

$$U_{\text{tot}} dx = T S_{\text{tot}} dx - P V_{\text{tot}} dx + \mu N_{\text{tot}} dx$$
$$\underbrace{U_{\text{tot}}}_{\text{constant}} dx = \underbrace{(T S_{\text{tot}} - P V_{\text{tot}} + \mu N_{\text{tot}})}_{\text{constant}} dx.$$

Since the integrand of both the left and right hand side are constants, this is easily integrable and the Euler equation is obtained:

$$U_{\text{tot}} = T S_{\text{tot}} - P V_{\text{tot}} + \mu N_{\text{tot}}.$$

B.2 Equilibrium as an equivalence of exchange rates

"Equilibrium" is a term that is commonly used across various disciplines. There is, however, a unifying principle and in this Section, I will attempt to explain that

principle from a fundamental standpoint. To use an analogy, I like to think of equilibrium as the point at which all parties involved in some sort of exchange agree on an exchange rate. In thermodynamics, energy is the currency and it *must* be conserved (first law of thermodynamics). Let us imagine two parties (or thermodynamic systems that are in communication with each other) A and B. Both A and B have some extensive quantity X_+. To each party, some quantity of X_+ is worth a different amount amount of currency (energy). That is, they have different exchange rates $\frac{\partial U}{\partial X_+}$. For this example, say $\frac{\partial U}{\partial X_{+,A}} > \frac{\partial U}{\partial X_{+,B}} > 0$. If A gives B 1 J worth of X_+ then this necessarily means B will gain 1 J of energy (conservation of energy) but since $\frac{\partial U}{\partial X_{+,A}} > \frac{\partial U}{\partial X_{+,B}}$, B will have to gain more X_+ than A lost. Hence, there is a net gain of X_+ globally. Since nothing restricts the further exchange of X_+ between A and B, this process can continue and we have a net transfer and generation of X_+. This situation describes a non-equilibrium process. Eventually, we should expect that any two parties should come to equilibrium when there is no observable change between the two systems. The only way this can be satisfied is if the exchange rate $\frac{\partial U}{\partial X_+}$ itself is a function of X_+ and the net X_+ is required to only increase after each transaction ($dX_{+,A} + dX_{+,B} > 0$ like the second law of thermodynamics). The exchange rate dependency on X_+ is analogous to the supply curve in economics where price (an exchange rate) increases as a function of quantity ($\frac{\partial^2 U}{\partial X_+^2} > 0$). Thus, if B continues to gain X_i, then each subsequent gain in X_i is worth more and more ($\frac{\partial U}{\partial X_{+,B}}$ gets larger with increasing $X_{+,B}$). On the other hand, as A loses X_i, each subsequent loss in X_i is worth less and less ($\frac{\partial U}{\partial X_{+,A}}$ gets smaller with decreasing $X_{+,A}$). Eventually, A and B will be exchanging the same quantity of X_i for the same amount of energy such that $\frac{\partial U}{\partial X_{+,A}} = \frac{\partial U}{\partial X_{+,B}}$. An extensive property that behaves like X_+ in the example described above would be entropy, S, and its associated exchange rate is temperature ($\frac{\partial U}{\partial S} = T$). Hence, when there is an equivalence of temperatures, we have *thermal* equilibrium as a result of an exchange of entropy.

Now, let us consider another extensive property X_- where $\frac{\partial U}{\partial X_-} < 0$. If $\frac{\partial U}{\partial X_{-,A}} < \frac{\partial U}{\partial X_{-,B}} < 0$, then as B transfers 1 J worth of X_- to A, B is actually gaining in X_- ($dX_{-,B} > 0$) while A is losing in X_- ($dX_{-,A} < 0$) by an amount that is less than what

B gained ($|dX_{-,B}| > |dX_{-,A}|$). The net effect is that X_- increases globally (assuming all other extensive properties that describe the systems are constant). Contrary to S (or X_+), X_- is free to increase or decrease as long as other extensive properties remain constant so transfer of X_- associated energy could move in either direction, i.e. there is no second law specifically for X_-. But, if we assume that there is a tendency of X_- to increase with S when at isothermal conditions, then equilibrium for the extensive property X_- would be reached when $\frac{\partial U}{\partial X_{-,A}} = \frac{\partial U}{\partial X_{-,B}}$ due to the second law of thermodynamics. This tendency can be illustrated by imagining a system wherein heat is involved and a differential change in energy is $dU = TdS + \frac{\partial U}{\partial X_-}dX_-$. The differential change in entropy, dS, as a function of the change in X_-, dX_-, should be evaluated for the specific temperature, T, and if dS is always positive for positive dX_-, then the sytem will tend toward equilibrium by exchange of X_-. An extensive property that behaves like X_- is volume, V, and its associated exchange rate is pressure ($\frac{\partial U}{\partial V} = -P$). Hence, when there is an equivalence of pressures, we have *mechanical* equilibrium as a result of an exchange of volume. The tendency toward mechanical equilibrium occurs because $dS > 0$ for $dV > 0$.[2]

According to the Euler equation B.3, the final extensive property we should consider is species number, N, and its associated exchange rate, the chemical potential, μ. When we have $\frac{\partial U}{\partial N}$ equal for A and B, we have *chemical* equilibrium (equivalence of chemical potentials from the exchange and generation/destruction of species). Chemical potential is a bit more difficult to grasp since we cannot actually observe molecules and atoms moving around, changing forms, etc. However, since an increase in N is associated with an increase in S isothermally, chemical equilibrium would be reached eventually due to the second law of thermodynamics. That is, for $\mu_{i,A} = \frac{\partial U}{\partial N_{i,A}} > \mu_{i,B} = \frac{\partial U}{\partial N_{i,B}}$, there should be a net flow of N_i from A to B.

More generally, a particular equilibrium associated with an extensive property X_j is reached when

$$\frac{\partial U}{\partial X_{j,A}} = \frac{\partial U}{\partial X_{j,B}}. \tag{B.4}$$

[2]For an ideal gas, $dS = Nk\frac{dV}{V}$ isothermally.

The system will tend toward this particular equilibrium as long as X_j increases with S in the isothermal condition since

$$dU = TdS + \frac{\partial U}{\partial X_j} dX_j. \tag{B.5}$$

If multiple extensive properties that increase with S isothermally are involved then

$$dU = TdS + \sum_j \frac{\partial U}{\partial X_j} dX_j \tag{B.6}$$

and eventually all types of equilibrium will be reached.

B.3 Generalized chemical potential

In this Section, we will generalize the definition of chemical potential. Consider the following generic Euler expression:

$$U = TS - PV + \sum_i \mu_i N_i + \sum_j \chi_j X_j \tag{B.7}$$

where χ_j is some intensive property for some extensive variable X_j. We also know from the Euler homogeneous function theorem that

$$dU = TdS - PdV + \sum_i \mu_i dN_i + \sum_j \chi_j dX_j. \tag{B.8}$$

From B.7, it is apparent that considering no additional contributions beside TS and PV, then the conventional Gibbs energy ($G \equiv U + PV - TS$) is $\sum_i \mu_i N_i$. But if other contributions are present, then conventional Gibbs energy is $\sum_i \mu_i N_i + \sum_j \chi_j X_j$. If we define a new, generalized Gibbs energy, $\tilde{G}$, where the Legendre transformation $\tilde{G} \equiv U + PV - TS - \sum_j \chi_j X_j$ is used then

$$\tilde{G} \equiv \underbrace{U + PV - TS}_{\text{conventional Gibbs}} - \sum_j \chi_j X_j = \sum_i \mu_i N_i \tag{B.9}$$

and one obtains the classical result that Gibbs potential should be the sum of chemical potentials. Differentiating Eqn. B.9 yields

$$dU+PdV+VdP-TdS-SdT-\sum_j \chi_j dX_j-\sum_j X_j d\chi_j=\sum_i \mu_i dN_i+\sum_i N_i d\mu_i. \quad \text{(B.10)}$$

If we plugin Eqn. B.8,

$$\cancel{TdS-PdV}+\cancel{\sum_i \mu_i dN_i}+\cancel{\sum_j \chi_j dX_j}+\cancel{PdV}+VdP-\cancel{TdS}-SdT-\cancel{\sum_j \chi_j dX_j}-\sum_j X_j d\chi_j=\cancel{\sum_i \mu_i dN_i}+\sum_i N_i d\mu_i$$

and we obtain a generalized Gibbs-Duhem equation:

$$\boxed{\sum_i N_i d\mu_i=-SdT+VdP-\sum_j X_j d\chi_j}. \quad \text{(B.11)}$$

We can see here the remarkable result that chemical potential is *only a function of intensive variables*. A molecule or atom does not care how big the container is, it only cares about the exchange rates (intensive properties) around itself. Effectively, molecules and atoms, acting on chemical potentials, are the agents of equilibration.

Usually, in a conventional system where surface energy is not considered, chemical potential is the partial molar ($\frac{\partial}{\partial N}$ operator) of the conventional Gibbs energy. However, if other properties besides T and P were involved, using the partial molar of the conventional Gibbs energy would result in an incorrect chemical potential where μ would depend on an extensive quantity. Instead, we should define chemical potential as the polar molar of the generic Gibbs free energy $\tilde{G}$:

$$\boxed{\tilde{G}\equiv U+PV-TS-\sum_j \chi_j X_j}. \quad \text{(B.12)}$$

This way, chemical potential remains a function of intensive quantities:

$$\boxed{\tilde{G}=VdP-SdT+\sum_i \mu_i dN_i-\sum_j X_j d\chi_j}. \quad \text{(B.13)}$$

B.4 Chemical potential and surface tension

Let us imagine a thin slab of some arbitrary phase with area A that is parallel to the interface and offset some distance $x-s$ where s is the location of Gibbs dividing surface. On the other side of the Gibbs dividing surface, the concentration is zero; thus, any excess quantity η_{excess} depending on an intensive quantity ζ can be calculated according to

$$\eta_{\text{excess}} = \int_s^\infty (\zeta - \zeta_\infty)\, dx. \tag{B.14}$$

The slab is in the presence of some sort of potential energy, e.g. an electric potential. This potential determines the concentration of a species at a particular location of x. The slab has a thickness δx that is sufficiently thin enough to consider the slab isotropic for all intensive properties T, P, μ_i, ψ_i (generalized potential energy), and $\varpi\delta x$ (lateral pressure of the slab). The $\varpi\delta x$ term is used to back out surface tension later by integrating it through the depth of the surface and has units of $\mathrm{N\,m^{-1}}$ (ϖ by itself is a lateral pressure with units of $\mathrm{N\,m^{-2}}$). We can think of this as a surface tension of a particular thin slab that we are examining. We should expect that $\varpi\delta x$ should approach zero into the depth of the fluid (surface tension in the bulk should be zero). This is just a quantity that allows us to keep track of changes to the pressure tensor in the lateral directions (yz plane) that occur. $\varpi\delta x$ is a convenient correction for anisotropies in the stress tensor expressed below.

$$\sigma = \begin{bmatrix} -P & 0 & 0 \\ 0 & -P-\varpi & 0 \\ 0 & 0 & -P-\varpi \end{bmatrix} \tag{B.15}$$

The total surface pressure can then be calculated as

$$\Pi = \int_s^\infty \varpi\, dx. \tag{B.16}$$

Recognizing that area, A, is an extensive quantity and its associated intensive quantity $\frac{\partial U}{\partial A}$ is $-\varpi\delta x$, then applying the generalized Gibbs-Duhem relation (Eq.

B.11) gives

$$\sum_i N_i d\mu_i = -SdT + VdP + A\delta x d\varpi. \tag{B.17}$$

Note that chemical potential is only a function of intensive properties, including the lateral pressure. At constant temperature and pressure,

$$\sum_i \frac{N_i}{A} d\mu_i = \delta x d\varpi. \tag{B.18}$$

Now let us focus our attention on $d\mu_i$. We know that it must be of the form

$$\mu_i = \mu_i^* + kT \ln\left(f_i \frac{n_i}{n_i^*}\right) + \psi_i \tag{B.19}$$

where f_i is the activity coefficient, n_i is the number density, and ψ_i is some generic potential energy (for an electric field, $\psi_i = z_i e\phi$). The differential chemical potential at constant T is then

$$d\mu_i = kT\left(\frac{1}{n_i} + \frac{1}{f_i}\frac{\partial f_i}{\partial n_i}\right) dn_i + d\psi_i. \tag{B.20}$$

The volume of this slab is $A\delta x$, so $n_i = \frac{N_i}{A\delta x}$. Combining Eqs. B.18 and B.20, we can express the differential lateral pressure as

$$d\varpi \cancel{\delta x} = \sum_i kT \cancel{\delta x} dn_i + \sum_i kT \frac{n_i}{f_i}\frac{\partial f_i}{\partial n_i} \cancel{\delta x} dn_i + \sum_i n_i \cancel{\delta x} d\psi_i. \tag{B.21}$$

Provided that we know the relationship between n_i and ψ_i (you would use the Poisson-Boltzmann equation in an electric field), we can integrate to find the lateral pressure, ϖ. Since the state of the system before the interface was created was the same as the bulk, the lower limit of integration is the property value associated with the bulk state ($n_{i,\infty}$ and $\psi_{i,\infty}$). This yields

$$\varpi = \sum_i kT\left(n_i - n_{i,\infty}\right) + \sum_i kT \int_{n_{i,\infty}}^{n_i} \frac{n_i}{f_i}\frac{\partial f_i}{\partial n_i} dn_i + \sum_i \int_{\psi_{i,\infty}}^{\psi_i} n_i d\psi_i. \tag{B.22}$$

To get the total surface tension, we have to integrate the lateral pressure through the depth of the phase:

$$\gamma = -\Pi = -\int_s^\infty \varpi dx. \tag{B.23}$$

Furthermore, the suface excess concentration should be

$$\Gamma_i = \int_s^\infty \left(n_i - n_{i,\infty}\right) dx. \tag{B.24}$$

Then, the surface tension of a generic system has the integral form

$$\boxed{-\gamma = \sum_i kT\Gamma_i + \sum_i kT \int_s^\infty \int_{n_{i,\infty}}^{n_i(x)} \frac{n_i}{f_i}\frac{\partial f_i}{\partial n_i} dn_i dx + \sum_i \int_s^\infty \int_{\psi_{i,\infty}}^{\psi_i(x)} n_i d\psi_i dx}. \tag{B.25}$$

Thus, if n_i and ψ_i are known as functions of x for all species, and f_i and ψ_i are known as functions of n_i, then this integral can be calculated.

APPENDIX C

GEOMETRY

C.1 Cone sliced by an angled plane

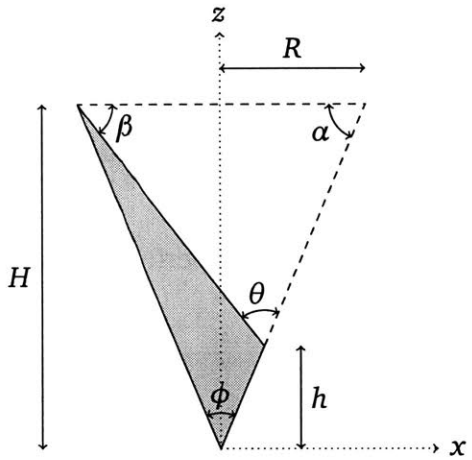

Figure C-1: Sliced cone geometry

From Fig. Figure C-1, we can deduce the following angle identies:

$$\alpha = \frac{\pi}{2} - \frac{\phi}{2} \tag{C.1}$$

$$\beta = \frac{\pi}{2} + \frac{\phi}{2} - \theta. \tag{C.2}$$

Using trigonometric identities, the total height, H, is

$$H = R\cot\left(\frac{\phi}{2}\right). \tag{C.3}$$

The bottom height, h, is

$$h = H - \frac{2R}{\cot(\alpha)+\cot(\beta)}. \tag{C.4}$$

The minimal bound of θ is ϕ, while the maximal bound is when $h = H$. Therefore,

$$\theta_{\min} = \phi \tag{C.5}$$

$$\theta_{\max} = \frac{\phi}{2} + \frac{\pi}{2}. \tag{C.6}$$

The equation of the intersecting plane in cartesian coordinates can be obtained by considering a line in the xz-plane having the slope-intercept form of

$$z = (x+R)\tan(-\beta) + H. \tag{C.7}$$

In spherical coordinates (Θ is the azimuthal angle, Φ is the polar angle), it is

$$\rho = R\frac{\cot\left(\frac{\phi}{2}\right)-\tan(\beta)}{\cos(\Phi)+\cos(\Theta)\sin(\Phi)\tan(\beta)}. \tag{C.8}$$

To obtain the volume of the sliced cone, we perform the triple integral

$$V = \int_0^{\frac{\phi}{2}}\int_{-\pi}^{\pi}\int_0^{R\frac{\cot\left(\frac{\phi}{2}\right)-\tan(\beta)}{\cos(\Phi)+\cos(\Theta)\sin(\Phi)\tan(\beta)}} \rho^2\sin(\Phi)\,d\rho\,d\Theta\,d\Phi. \tag{C.9}$$

Evaluating this integral, we obtain the remarkably simple result that [1]

$$\boxed{V = \frac{\pi R^3}{3}\cot\left(\frac{\phi}{2}\right)(\csc(\theta)\sin(\theta-\phi))^{\frac{3}{2}}}. \tag{C.10}$$

To obtain the lateral surface area, we integrate ρ up to the loop defined by Eq. C.8

[1] This result is equivalent to Eq. 8 in J. J. Lorenz' thesis [99]

where $\Phi = \phi/2$. Thus, our double integral is

$$A_{\text{lat}} = \int_{-\pi}^{\pi} \int_{0}^{R \frac{\cot\left(\frac{\phi}{2}\right) - \tan(\beta)}{\cos\left(\frac{\phi}{2}\right) + \cos(\Theta)\sin\left(\frac{\phi}{2}\right)\tan(\beta)}} \rho \sin\left(\frac{\phi}{2}\right) d\rho d\Theta. \tag{C.11}$$

The result is

$$\boxed{A_{\text{lat}} = \pi R^2 \cot\left(\frac{\phi}{2}\right) \csc(\theta) \sin\left(\theta - \frac{\phi}{2}\right) \sqrt{\cos(\phi) - \cot(\theta)\sin(\phi)}}. \tag{C.12}$$

To get the top surface area, consider the equation of the cone where

$$x^2 + y^2 = \left(z \tan\left(\frac{\phi}{2}\right)\right)^2. \tag{C.13}$$

Solving this for z and setting it equal to Eq. C.7 gives a relationship between x and y at the intersection of the plane and the cone:

$$\frac{\sqrt{x^2 + y^2}}{\tan\left(\frac{\phi}{2}\right)} = (x + R)\tan(-\beta) + H. \tag{C.14}$$

Transforming this into polar coordinates, where $x^2 + y^2 = r^2$ and $x = r\cos(\Theta)$, and solving for r,

$$r = \frac{H - R\tan(\beta)}{\tan(\beta)\cos(\Theta) + \cot\left(\frac{\phi}{2}\right)}. \tag{C.15}$$

Now, we can solve the area of the top of the cone by the double integral

$$A_{\text{top}} = \int_{-\pi}^{\pi} \int_{0}^{\frac{H - R\tan(\beta)}{\tan(\beta)\cos(\Theta) + \cot\left(\frac{\phi}{2}\right)}} r \sec(\beta)\, dr d\Theta, \tag{C.16}$$

which results in

$$\boxed{A_{\text{top}} = \pi R^2 \csc(\theta) \cos\left(\frac{\phi}{2}\right) \sqrt{\cos(\phi) - \cot(\theta)\sin(\phi)}}. \tag{C.17}$$

Note that this result is equivalent to calculating the area of an ellipse ($A_{\text{top}} = \pi ab$)

where the semi-major axis is

$$a = R\csc(\theta)\cos\left(\frac{\phi}{2}\right) \tag{C.18}$$

and the semi-minor axis is

$$b = R\sqrt{\cos(\phi) - \cot(\theta)\sin(\phi)}. \tag{C.19}$$

This is expected since the intersection is a conic section.

APPENDIX D

ELECTROHYDRODYNAMIC AND ELECTROWETTING EFFECTS

In this Appendix, we will discuss the physics of electrohydrodynamic (EHD) and electrowetting (EW) effects. We will show that these effects do not play a significant role in our work of active boiling control with electric fields and charged surfactants (Chapter 5).

D.1 Electrohydrodynamic effects

In any fluid system, conservation of mass and momentum require that

$$\frac{\partial \rho}{\partial t} + \nabla \cdot (\rho \mathbf{v}) = 0 \tag{D.1}$$

and

$$\rho\left(\frac{\partial \mathbf{v}}{\partial t} + \mathbf{v} \cdot \nabla \mathbf{v}\right) = -\nabla p + \nabla \cdot \mathbf{T} + \rho \mathbf{g} + \mathbf{f}_e \tag{D.2}$$

where ρ is the mass density, $\mathbf{v}$ is the velocity, p is the pressure μ is the viscosity, $\mathbf{g}$ is the acceleration due to gravity, and $\mathbf{f}_e$ is the body force due to electric fields. The

body force within the fluid due to an electric field, $\mathbf{E}$, has two components: a free charge component, $\mathbf{f}_{e,f}$, and a dielectric component, $\mathbf{f}_{e,d}$ [129, 40]:

$$\mathbf{f}_e = \underbrace{\rho_f \mathbf{E}}_{\mathbf{f}_{e,f}} + \underbrace{\left[-\frac{1}{2}|\mathbf{E}|^2 \nabla\varepsilon + \nabla\left[\frac{1}{2}\rho|\mathbf{E}|^2\left(\frac{\partial\varepsilon}{\partial\rho}\right)_T\right]\right]}_{\mathbf{f}_{e,d}}. \tag{D.3}$$

Here, the absolute permittivity, $\varepsilon = \varepsilon(\rho, T) = \varepsilon_r(\rho, T)\varepsilon_0$, is assumed to have a real number value since complex permittivity is not important until frequencies are on the order of several GHz [130]. The free charge density, ρ_f, is the net difference between positive and negative charge. Since free charges in the conductor must populate at the surface, ρ_f is zero everywhere in the bulk. Only in the vicinity of the electric double layer ($\frac{1}{\kappa} \approx 5\,\text{nm}$ for a system at 3 mM) will free charge density play a role. The dielectric term, $\mathbf{f}_{e,d}$, in equation (D.3) depends on gradients in density and temperature which only appear in the thermal boundary layer. The thermal boundary length can be estimated using $\delta_T = 3.22k/h_{boil}$ [131]. At the largest heat transfer coefficients observed in our experiments (approximately $4\,\text{W}\,\text{cm}^{-2}\,\text{K}^{-1}$), the thermal boundary length is calculated to be 0.05 mm. Since $\delta_T >> \frac{1}{\kappa}$, we ignore any contribution due to free charge density. To estimate the effect of electrostriction (dielectric body force effects) in the boundary layer, we first convert equation (D.3) to 1D and obtain

$$f_{e,d} = -\frac{1}{2}|\mathbf{E}|^2 \frac{dT}{dx}\left[\left(\frac{\partial\varepsilon}{\partial T}\right)_\rho + 2\left(\frac{\partial\varepsilon}{\partial\rho}\right)_T\left(\frac{\partial\rho}{\partial T}\right)_p + \rho\frac{\partial^2\varepsilon}{\partial\rho\partial T}\right]. \tag{D.4}$$

Then, we apply the scaling $\frac{dT}{dx} \sim -\frac{T_{wall}-T_{sat}}{\delta_T}$ to obtain

$$f_{e,d} \sim \frac{1}{2}|\mathbf{E}|^2 \frac{T_{wall}-T_{sat}}{\delta_T}\left[\left(\frac{\partial\varepsilon}{\partial T}\right)_\rho + 2\left(\frac{\partial\varepsilon}{\partial\rho}\right)_T\left(\frac{\partial\rho}{\partial T}\right)_p + \rho\frac{\partial^2\varepsilon}{\partial\rho\partial T}\right]. \tag{D.5}$$

Evaluating $f_{e,d}$ at a saturation temperature of 100 °C and with an estimated field strength of $35\,\text{V}\,\text{m}^{-1}$ yields a negligible value of $0.5\,\text{mN}\,\text{m}^{-3}$, which is more than six orders of magnitude smaller than the gravitational body force. Thus, EHD effects in the bulk and boundary layer are completely negligible.

D.2 Electrowetting effects

Since free charges accumulate at the surface (liquid-vapor and liquid-solid interfaces) at a very small characteristic Debye length, $\frac{1}{\kappa}$, the free charge body force, $f_{e,f}$, can affect interfacial tension [113]. As shown in Appendix B.4, the surface tension of a system is

$$-\gamma = \sum_i kT\Gamma_i + \sum_i kT \int_0^\infty \int_{n_{i,\infty}}^{n_i(x)} \frac{n_i}{f_i} \frac{\partial f_i}{\partial n_i} dn_i dx + \sum_i \int_0^\infty \int_0^{\phi(x)} z_i e n_i d\phi dx \quad \text{(D.6)}$$

where we have set $x = 0$ to the location of the Gibbs dividing surface and the electric potential, ϕ, far away to zero. From EDL theory (Section 3.3), it can be shown that the last term of this surface pressure is always positive (surface tension always decreases) since there is always a net excess of ions with the same polarity as the applied potential. The middle term could hypothetically be positive for highly attractive species; however, even with the highly interacting long-tail surfactants we have modeled, this term still remains positive. The first term, which is the 2D ideal gas component should always be positive given that there is always an excess of a surfactant at the interface. Thus, the effective solid-liquid interfacial energy is always reduced with an applied potential. As a consequence, any electrowetting effect always works to reduce the contact angle of the fluid and increase wetting regardless of the polarity of the applied potential. From nucleation theory, any decrease in contact angle should suppress bubble nucleation. However, in the NaBr control experiment, nucleation was not visibly suppressed nor did the boiling curve change substantially. The fact that the contact angle actually increased and nucleation was promoted with DTAB under applied voltage indicates that EHD or electrowetting effects are negligible at the solid-liquid interface in our experiments in Chapter 5.

BIBLIOGRAPHY

[1] R. Linton, "North American Cooking Pots," *American Antiquity*, vol. 9, no. 4, pp. 369–13, Apr. 1944.

[2] J. M. Skibo and E. Blinman, "Exploring the origins of pottery on the Colorado Plateau," in *Pottery and People*, J. M. Skibo and G. Feinman, Eds. University of Utah Press, 1999.

[3] E. Papadopoulos, "Heron of Alexandria (c. 10–85 AD)," in *Distinguished Figures in Mechanism and Machine Science*. Dordrecht: Springer Netherlands, 2007, pp. 217–245.

[4] F. M. Scherer, "Invention and Innovation in the Watt-Boulton Steam-Engine Venture," *Technology and Culture*, vol. 6, no. 2, pp. 165–24, 1965.

[5] R. Kehlhofer, *Combined-Cycle Gas & Steam Turbine Power Plants*. Tulsa, Okla: PennWell, 2009.

[6] J. D. Hansen, J. A. Johnson, and D. A. Winter, "History and use of heat in pest control: a review," *International Journal of Pest Management*, vol. 57, no. 4, pp. 267–289, Oct. 2011.

[7] T. Mattila Sandholm and G. Wirtanen, "Biofilm formation in the industry: A review," *Food Reviews International*, vol. 8, no. 4, pp. 573–603, Jan. 1992.

[8] A. Haryanto, S. Fernando, N. Murali, and S. Adhikari, "Current Status of Hydrogen Production Techniques by Steam Reforming of Ethanol: A Review," *Energy & Fuels*, vol. 19, no. 5, pp. 2098–2106, Sep. 2005.

[9] T. Humplik, J. Lee, S. C. O'Hern, B. A. Fellman, M. A. Baig, S. F. Hassan, M. A. Atieh, F. Rahman, T. Laoui, R. Karnik, and E. N. Wang, "Nanostructured materials for water desalination," *Nanotechnology*, vol. 22, no. 29, p. 292001, Jun. 2011.

[10] L. L. Vasiliev, "Heat pipes in modern heat exchangers," *Applied Thermal Engineering*, vol. 25, no. 1, pp. 1–19, Jan. 2005.

[11] J. R. Barbosa Jr., G. B. Ribeiro, and P. A. de Oliveira, "A State-of-the-Art Review of Compact Vapor Compression Refrigeration Systems and Their Applications," *Heat Transfer Engineering*, vol. 33, no. 4-5, pp. 356–374, Mar. 2012.

[12] G. Ni, G. Li, S. V. Boriskina, H. Li, W. Yang, T. Zhang, and G. Chen, "Steam generation under one sun enabled by a floating structure with thermal concentration," *Nature Energy*, vol. 1, no. 9, pp. 16 126–7, Aug. 2016.

[13] S. Yang, D. Xiang, A. Bryant, P. Mawby, L. Ran, and P. Tavner, "Condition Monitoring for Device Reliability in Power Electronic Converters: A Review," *Power Electronics, IEEE Transactions on*, vol. 25, no. 11, pp. 2734–2752, 2010.

[14] A. Shakouri, "Nanoscale thermal transport and microrefrigerators on a chip," *Proceedings of the IEEE*, vol. 94, no. 8, pp. 1613–1638, 2006.

[15] T. Young, "An Essay on the Cohesion of Fluids," *Philosophical Transactions of the Royal Society of London*, vol. 95, no. 0, pp. 65–87, Jan. 1805.

[16] V. P. Carey, *Liquid Vapor Phase Change Phenomena: An Introduction to the Thermophysics of Vaporization and Condensation Processes in Heat Transfer Equipment, Second Edition*, 2nd ed. Taylor & Francis, Nov. 2007.

[17] C. H. Wang and V. K. Dhir, "Effect of surface wettability on active nucleation site density during pool boiling of water on a vertical surface," *Journal of Heat Transfer*, vol. 115, no. 3, pp. 659–669, 1993.

[18] N. Shiro, "The maximum and minimum values of the heat q transmitted from metal to boiling water under atmospheric pressure," *International Journal of Heat and Mass Transfer*, vol. 27, no. 7, pp. 959–970, Jul. 1984.

[19] S. G. Kandlikar, "A Theoretical Model to Predict Pool Boiling CHF Incorporating Effects of Contact Angle and Orientation," *Journal of Heat Transfer*, vol. 123, no. 6, pp. 1071–1079, Dec. 2001.

[20] K.-H. Chu, Y. Soo Joung, R. Enright, C. R. Buie, and E. N. Wang, "Hierarchically structured surfaces for boiling critical heat flux enhancement," *Applied Physics Letters*, vol. 102, no. 15, pp. 151 602–5, 2013.

[21] M. M. Rahman, E. Ölçeroğlu, and M. McCarthy, "Role of Wickability on the Critical Heat Flux of Structured Superhydrophilic Surfaces," *Langmuir*, vol. 30, no. 37, pp. 11 225–11 234, Sep. 2014.

[22] N. S. Dhillon, J. Buongiorno, and K. K. Varanasi, "Critical heat flux maxima during boiling crisis on textured surfaces," *Nature Communications*, vol. 6, pp. 1–12, Aug. 2015.

[23] C. Li, Z. Wang, P.-I. Wang, Y. Peles, N. Koratkar, and G. P. Peterson, "Nanostructured Copper Interfaces for Enhanced Boiling," *Small*, vol. 4, no. 8, pp. 1084–1088, Aug. 2008.

[24] R. Chen, M.-C. Lu, V. Srinivasan, Z. Wang, H. H. Cho, and A. Majumdar, "Nanowires for enhanced boiling heat transfer," *Nano Letters*, vol. 9, no. 2, pp. 548–553, Feb. 2009.

[25] S. Kim, H. D. Kim, H. Kim, H. S. Ahn, H. Jo, J. Kim, and M. H. Kim, "Effects of nano-fluid and surfaces with nano structure on the increase of CHF," *Experimental thermal and fluid science*, vol. 34, no. 4, pp. 487–495, May 2010.

[26] K.-H. Chu, R. Enright, and E. N. Wang, "Structured surfaces for enhanced pool boiling heat transfer," *Applied Physics Letters*, vol. 100, no. 24, p. 241603, 2012.

[27] S. G. Liter and M. Kaviany, "Pool-boiling CHF enhancement by modulated porous-layer coating: theory and experiment," *International Journal of Heat and Mass Transfer*, vol. 44, no. 22, pp. 4287–4311, Nov. 2001.

[28] H. O'Hanley, C. Coyle, J. Buongiorno, T. McKrell, L.-w. Hu, M. Rubner, and R. Cohen, "Separate effects of surface roughness, wettability, and porosity on the boiling critical heat flux," *Applied Physics Letters*, vol. 103, no. 2, p. 024102, 2013.

[29] S. M. You, J. H. Kim, and K. H. Kim, "Effect of nanoparticles on critical heat flux of water in pool boiling heat transfer," *Applied Physics Letters*, vol. 83, no. 16, pp. 3374–3376, 2003.

[30] S. M. Kwark, R. Kumar, G. Moreno, J. Yoo, and S. M. You, "Pool boiling characteristics of low concentration nanofluids," *International Journal of Heat and Mass Transfer*, vol. 53, no. 5, pp. 972–981, Feb. 2010.

[31] H.-J. J. Cho, D. J. Preston, Y. Zhu, and E. N. Wang, "Nanoengineered materials for liquid–vapour phase-change heat transfer," *Nature Reviews Materials*, vol. 2, pp. 1–17, Dec. 2016.

[32] H. F. O'Hanley, "Separate effects of surface roughness, wettability and porosity on boiling heat transfer and critical heat flux and optimization of boiling surfaces." Ph.D. dissertation, Massachusetts Institute of Technology, 2012.

[33] Z.-h. Liu and L. Liao, "Sorption and agglutination phenomenon of nanofluids on a plain heating surface during pool boiling," *International Journal of Heat and Mass Transfer*, vol. 51, no. 9-10, pp. 2593–2602, May 2008.

[34] C. Li and G. P. Peterson, "Parametric study of pool boiling on horizontal highly conductive microporous coated surfaces," *Journal of Heat Transfer*, vol. 129, no. 11, pp. 1465–1475, Nov. 2007.

[35] M. M. Rahman, J. Pollack, and M. McCarthy, "Increasing Boiling Heat Transfer using Low Conductivity Materials," *Scientific Reports*, vol. 5, p. 13145, Aug. 2015.

[36] D. Cooke and S. G. Kandlikar, "Effect of open microchannel geometry on pool boiling enhancement," *International Journal of Heat and Mass Transfer*, vol. 55, no. 4, pp. 1004–1013, Jan. 2012.

[37] A. R. Betz, J. Jenkins, and D. Attinger, "Boiling heat transfer on superhydrophilic, superhydrophobic, and superbiphilic surfaces," *International Journal of Heat and Mass Transfer*, vol. 57, no. 2, pp. 733–741, 2013.

[38] A. Jaikumar and S. G. Kandlikar, "Ultra-high pool boiling performance and effect of channel width with selectively coated open microchannels," *International Journal of Heat and Mass Transfer*, vol. 95, no. C, pp. 795–805, Apr. 2016.

[39] H.-J. J. Cho, J. P. Mizerak, and E. N. Wang, "Turning bubbles on and off during boiling using charged surfactants," *Nature Communications*, vol. 6, pp. 1–7, Oct. 2015.

[40] T. B. Jones, "Electrohydrodynamically Enhanced Heat Transfer in Liquids—A Review," *Advances in heat transfer*, vol. 14, pp. 107–148, 1978.

[41] L. Cheng, D. Mewes, and A. Luke, "Boiling phenomena with surfactants and polymeric additives: A state-of-the-art review," *International Journal of Heat and Mass Transfer*, vol. 50, no. 13-14, pp. 2744–2771, Jul. 2007.

[42] G. W. Stroebe, E. M. Baker, and W. L. Badger, "Boiling-Film Heat Transfer Coefficients in a Long-Tube Vertical Evaporator," *Industrial & Engineering Chemistry*, vol. 31, no. 2, pp. 200–206, Feb. 1939.

[43] M. Bourrel and R. S. Schechter, *Microemulsions and Related Systems: Formulation, Solvency, and Physical Properties*, ser. Surfactant science series. Marcel Dekker, 1988.

[44] J. Zhang and R. M. Manglik, "Additive Adsorption and Interfacial Characteristics of Nucleate Pool Boiling in Aqueous Surfactant Solutions," *Journal of Heat Transfer*, vol. 127, no. 7, p. 684, 2005.

[45] A. F. H. Ward and L. Tordai, "Time-Dependence of Boundary Tensions of Solutions I. The Role of Diffusion in Time-Effects," *The Journal of chemical physics*, vol. 14, no. 7, p. 453, 1946.

[46] G. P. de, "Deposition of Langmuir-Blodgett layers," *Colloid and Polymer Science Kolloid Zeitschrift & Zeitschrift für Polymere*, vol. 264, no. 5, pp. 463–465, May 1986.

[47] V. Wasekar and R. Manglik, "Pool Boiling Heat Transfer in Aqueous Solutions of an Anionic Surfactant," *Journal of Heat Transfer*, vol. 122, no. 4, p. 708, 2000.

[48] ——, "The influence of additive molecular weight and ionic nature on the pool boiling performance of aqueous surfactant solutions," *International Journal of Heat and Mass Transfer*, vol. 45, no. 3, pp. 483–493, 2002.

[49] R. M. Manglik, V. M. Wasekar, and J. Zhang, "Dynamic and equilibrium surface tension of aqueous surfactant and polymeric solutions," *Experimental thermal and fluid science*, vol. 25, no. 1, pp. 55–64, 2001.

[50] G. Hetsroni, J. L. Zakin, Z. Lin, A. Mosyak, E. A. Pancallo, and R. Rozenblit, "The effect of surfactants on bubble growth, wall thermal patterns and heat transfer in pool boiling," *International Journal of Heat and Mass Transfer*, vol. 44, no. 2, pp. 485–497, 2000.

[51] V. K. Dhir, H. S. Abarajith, and D. Li, "Bubble Dynamics and Heat Transfer during Pool and Flow Boiling," *Heat Transfer Engineering*, vol. 28, no. 7, pp. 608–624, Jul. 2007.

[52] V. M. Wasekar and R. M. Manglik, "Short-Time-Transient Surfactant Dynamics and Marangoni Convection Around Boiling Nuclei," *Journal of Heat Transfer*, vol. 125, no. 5, pp. 858–9, 2003.

[53] D. J. Preston, N. Miljkovic, J. Sack, R. Enright, J. Queeney, and E. N. Wang, "Effect of hydrocarbon adsorption on the wettability of rare earth oxide ceramics," *Applied Physics Letters*, vol. 105, no. 1, pp. 011 601–6, Jul. 2014.

[54] T. Smith, "The hydrophilic nature of a clean gold surface," *Journal of Colloid and Interface Science*, vol. 75, no. 1, pp. 51–55, 1980.

[55] S. Miyagishi, K. Okada, and T. Asakawa, "Salt Effect on Critical Micelle Concentrations of Nonionic Surfactants, N-Acyl-N-methylglucamides (MEGA-n)," *Journal of Colloid and Interface Science*, vol. 238, no. 1, pp. 91–95, Jun. 2001.

[56] S. B. Sulthana, P. V. C. Rao, S. G. T. Bhat, T. Y. Nakano, G. Sugihara, and A. K. Rakshit, "Solution Properties of Nonionic Surfactants and Their Mixtures: Polyoxyethylene (10) Alkyl Ether [C_nE_{10}] and Mega-10," *Langmuir*, vol. 16, no. 3, pp. 980–987, Feb. 2000.

[57] N. J. Zoeller and D. Blankschtein, "Development of user-friendly computer programs to predict solution properties of single and mixed surfactant systems," *Industrial & engineering chemistry research*, vol. 34, no. 12, pp. 4150–4160, 1995.

[58] K.-H. Chu, "Micro and nanostructured surfaces for enhanced phase change heat transfer," Ph.D. dissertation, Massachusetts Institute of Technology, Cambridge, MA, 2013.

[59] C. E. Stauffer, "The Measurement of Surface Tension by the Pendant Drop Technique," *The Journal of Physical Chemistry*, vol. 69, no. 6, pp. 1933–1938, Jun. 1965.

[60] F. K. Hansen and G. Rødsrud, "Surface tension by pendant drop," *Journal of Colloid and Interface Science*, vol. 141, no. 1, pp. 1–9, Jan. 1991.

[61] V. B. Fainerman and R. Miller, "Maximum bubble pressure tensiometry—an analysis of experimental constraints," *Advances in Colloid and Interface Science*, vol. 108-109, pp. 287–301, May 2004.

[62] K. W. Bewig and W. A. Zisman, "The Wetting of Gold and Platinum by Water," *The Journal of Physical Chemistry*, vol. 69, no. 12, pp. 4238–4242, Dec. 1965.

[63] J. Eastoe and J. S. Dalton, "Dynamic surface tension and adsorption mechanisms of surfactants at the air–water interface," *Advances in Colloid and Interface Science*, vol. 85, no. 2-3, pp. 103–144, 2000.

[64] M. Gouy, "Sur la constitution de la charge électrique à la surface d'un électrolyte," *Journal de Physique Théorique et Appliquée*, vol. 9, no. 1, pp. 457–468, 1910.

[65] D. L. Chapman, "LI. A contribution to the theory of electrocapillarity," *Philosophical Magazine Series 6*, vol. 25, no. 148, pp. 475–481, Apr. 1913.

[66] O. Stern, "Zur Theorie der Elektrolytischen Doppelschicht," *Zeitschrift fur Elektrochemie*, vol. 30, pp. 508–516, 1924.

[67] J. T. Davies, "Adsorption of Long-Chain Ions. I," *Proceedings of the Royal Society A: Mathematical, Physical and Engineering Sciences*, vol. 245, no. 1242, pp. 417–428, Jun. 1958.

[68] ——, "The Distribution of Ions under a Charged Monolayer, and a Surface Equation of State for Charged Films," *Proceedings of the Royal Society A: Mathematical, Physical and Engineering Sciences*, vol. 208, no. 1093, pp. 224–247, Aug. 1951.

[69] E. H. Lucassen-Reynders, "Surface Equation of State for Ionized Surfactants," *The Journal of Physical Chemistry*, vol. 70, no. 6, pp. 1777–1785, Jun. 1966.

[70] J. A. V. Butler, "The Thermodynamics of the Surfaces of Solutions," *Proceedings of the Royal Society A: Mathematical, Physical and Engineering Sciences*, vol. 135, no. 827, pp. 348–375, Mar. 1932.

[71] R. P. Borwankar and D. T. Wasan, "Equilibrium and dynamics of adsorption of surfactants at fluid-fluid interfaces," *Chemical Engineering Science*, vol. 43, no. 6, pp. 1323–1337, Jan. 1988.

[72] P. A. Kralchevsky, K. D. Danov, G. Broze, and A. Mehreteab, "Thermodynamics of Ionic Surfactant Adsorption with Account for the Counterion Binding: Effect of Salts of Various Valency," *Langmuir*, vol. 15, no. 7, pp. 2351–2365, Mar. 1999.

[73] Y. J. Nikas, S. Puvvada, and D. Blankschtein, "Surface tensions of aqueous nonionic surfactant mixtures," *Langmuir*, vol. 8, no. 11, pp. 2680–2689, 1992.

[74] M. Mulqueen and D. Blankschtein, "Prediction of equilibrium surface tension and surface adsorption of aqueous surfactant mixtures containing ionic surfactants," *Langmuir*, vol. 15, no. 26, pp. 8832–8848, 1999.

[75] ——, "Prediction of Equilibrium Surface Tension and Surface Adsorption of Aqueous Surfactant Mixtures Containing Zwitterionic Surfactants," *Langmuir*, vol. 16, no. 20, pp. 7640–7654, Oct. 2000.

[76] L. Salem, "Attractive forces between long saturated chains at short distances," *The Journal of chemical physics*, vol. 37, p. 2100, 1962.

[77] C. G. Malmberg and A. A. Maryott, "Dielectric constant of water from 0° to 100°C," *J Res Nat Bureau Stand*, 1956.

[78] D. M. Ruthven, *Adsorption and Adsorption Processes*. New York: John Wiley & Sons, 1984.

[79] L. D. Landau and E. M. Lifshitz, *Statistical physics*. Oxford, New York: Pergamon Press, 1969.

[80] R. Subramanyam and C. Maldarelli, "Fluorescence Evidence That a Phase Transition Causes the Induction Time in the Reduction in Dynamic Tension during Surfactant Adsorption to a Clean Air/Water Interface and a Kinetic–Diffusive Transport Model for the Phase-Induced Induction," *Journal of Colloid and Interface Science*, vol. 253, no. 2, pp. 377–392, Sep. 2002.

[81] M. H. Abraham and E. Matteoli, "The temperature variation of the hydrophobic effect," *Journal of the Chemical Society, Faraday Transactions 1: Physical Chemistry in Condensed Phases*, vol. 84, no. 6, pp. 1985–2000, 1988.

[82] J.-S. Ko, S.-W. Oh, Y.-S. Kim, N. Nakashima, S. Nagadome, and G. Sugihara, "Adsorption and Micelle Formation of Mixed Surfactant Systems in Water. IV. Three Combinations of SDS with MEGA-8, -9 and -10," *Journal of Oleo Science*, vol. 53, no. 3, pp. 109–126, 2004.

[83] J. E. Carless, R. A. Challis, and B. A. Mulley, "Nonionic surface-active agents. Part V. The effect of the alkyl and the polyglycol chain length on the critical micelle concentration of some monoalkyl polyethers," *Journal of Colloid Science*, vol. 19, no. 3, pp. 201–212, Mar. 1964.

[84] S. R. Patil, N. Buchavzov, E. Carey, and C. Stubenrauch, "Binary mixtures of β-dodecylmaltoside (β-C12G2) with cationic and non-ionic surfactants: micelle and surface compositions," *Soft Matter*, vol. 4, no. 4, pp. 840–9, 2008.

[85] R. Zhang, L. Zhang, and P. Somasundaran, "Study of mixtures of n-dodecyl-β-d-maltoside with anionic, cationic, and nonionic surfactant in aqueous solutions using surface tension and fluorescence techniques," *Journal of Colloid and Interface Science*, vol. 278, no. 2, pp. 453–460, Oct. 2004.

[86] E. A. Simister, R. K. Thomas, and J. Penfold, "Comparison of neutron reflection and surface tension measurements of the surface excess of tetradecyltrimethylammonium bromide layers at the air/water interface," *Journal of Physical Chemistry*, vol. 96, no. 3, pp. 1383–1388, 1992.

[87] C. M. Phan, T. N. Le, and S.-i. Yusa, "A new and consistent model for dynamic adsorption of CTAB at air/water interface," *Dynamic effects in maximum bubble pressure experiments*, vol. 406, pp. 24–30, Jul. 2012.

[88] V. K. Michalis, O. A. Moultos, I. N. Tsimpanogiannis, and I. G. Economou, "Molecular dynamics simulations of the diffusion coefficients of light n-alkanes in water over a wide range of temperature and pressure," *Fluid Phase Equilibria*, vol. 407, no. C, pp. 236–242, Jan. 2016.

[89] L. S. Tee, S. Gotoh, and W. E. Stewart, "Molecular parameters for normal fluids: The Lennard-Jones 12-6 potential," *Industrial and Engineering Chemistry Fundamentals*, vol. 5, no. 3, pp. 356–363, Dec. 1966.

[90] X. Y. Hua and M. J. Rosen, "Dynamic surface tension of aqueous surfactant solutions: I. Basic paremeters," *Journal of Colloid and Interface Science*, vol. 124, no. 2, pp. 652–659, 1988.

[91] X. Li, R. Shaw, G. M. Evans, and P. Stevenson, "A simple numerical solution to the Ward–Tordai equation for the adsorption of non-ionic surfactants," *Computers & Chemical Engineering*, vol. 34, no. 2, pp. 146–153, Feb. 2010.

[92] H. Diamant and D. Andelman, "Kinetics of surfactant adsorption at fluid-fluid interfaces," *Journal of Physical Chemistry*, vol. 100, no. 32, pp. 13 732–13 742, Aug. 1996.

[93] D. K. Owens, "The dynamic surface tension of sodium dodecyl sulfate solutions," *Journal of Colloid and Interface Science*, vol. 29, no. 3, pp. 496–501, Mar. 1969.

[94] H. Jo, M. Kaviany, S. H. Kim, and M. H. Kim, "Heterogeneous bubble nucleation on ideally-smooth horizontal heated surface," *International Journal of Heat and Mass Transfer*, vol. 71, no. C, pp. 149–157, Apr. 2014.

[95] S. F. Jones, G. M. Evans, and K. P. Galvin, "Bubble nucleation from gas cavities - A review," *Advances in Colloid and Interface Science*, vol. 80, no. 1, pp. 27–50, Feb. 1999.

[96] B. B. Mikic and W. Rohsenow, "A new correlation of pool-boiling data including the effect of heating surface characteristics," *Journal of Heat Transfer*, vol. 91, no. 2, p. 245, 1969.

[97] Y. Y. Hsu, "On the size range of active nucleation cavities on a heating surface," *Journal of Heat Transfer*, vol. 84, no. 3, pp. 207–213, 1962.

[98] S. R. Yang and R. H. Kim, "A mathematical model of the pool boiling nucleation site density in terms of the surface characteristics," *International Journal of Heat and Mass Transfer*, vol. 31, no. 6, pp. 1127–1135, 1988.

[99] J. J. Lorenz, "The effects of surface conditions on boiling characteristics," Ph.D. dissertation, Massachusetts Institute of Technology, Feb. 1972.

[100] W. T. Brown, "A Study of Flow Surface Boiling," Ph.D. dissertation, Massachusetts Institute of Technology, Massachusetts Institute of Technology, 1967.

[101] M. S. Plesset and S. A. Zwick, "The Growth of Vapor Bubbles in Superheated Liquids," *Journal of Applied Physics*, vol. 25, no. 4, pp. 493–9, 1954.

[102] G. Son, V. K. Dhir, and N. Ramanujapu, "Dynamics and heat transfer associated with a single bubble during nucleate boiling on a horizontal surface," *Journal of Heat Transfer*, vol. 121, no. 3, pp. 623–631, Aug. 1999.

[103] H. S. Abarajith and V. K. Dhir, "A Numerical Study of the Effect of Contact Angle on the Dynamics of a Single Bubble During Pool Boiling," in *ASME International Mechanical Engineering Congress & Exposition*. New Orleans, Louisiana: American Society of Mechanical Engineers, Jan. 2002, pp. 467–475.

[104] A. Mukherjee and S. G. Kandlikar, "Numerical study of single bubbles with dynamic contact angle during nucleate pool boiling," *International Journal of Heat and Mass Transfer*, vol. 50, no. 1-2, pp. 127–138, Jan. 2007.

[105] Y. Nam, E. Aktinol, V. K. Dhir, and Y. S. Ju, "Single bubble dynamics on a superhydrophilic surface with artificial nucleation sites," *International Journal of Heat and Mass Transfer*, vol. 54, no. 7, pp. 1572–1577, Mar. 2011.

[106] B. B. Mikic, W. Rohsenow, and P. Griffith, "On bubble growth rates," *International Journal of Heat and Mass Transfer*, vol. 13, no. 4, pp. 657–666, 1970.

[107] A. F. Mills, *Heat Transfer*, 2nd ed. Prentice Hall, 1998.

[108] R. Cole, "Bubble frequencies and departure volumes at subatmospheric pressures," *AIChE Journal*, vol. 13, no. 4, pp. 779–783, Jul. 1967.

[109] W. Fritz, "Maximum volume of vapor bubbles," *Physikalische Zeitschrift*, vol. 36, no. 11, pp. 379–384, 1935.

[110] M. Q. Raza, N. Kumar, and R. Raj, "Surfactants for Bubble Removal against Buoyancy." *Scientific Reports*, 2015.

[111] S. G. Kandlikar, M. Shōji, and V. K. Dhir, *Handbook of phase change: boiling and condensation*. Philadelphia, PA: Taylor & Francis, 1999.

[112] M. Markels and R. L. Durfee, "The effect of applied voltage on boiling heat transfer," *AIChE Journal*, vol. 10, no. 1, pp. 106–110, 1964.

[113] F. Mugele and J.-C. Baret, "Electrowetting: from basics to applications," *Journal of Physics: Condensed Matter*, vol. 17, no. 28, pp. R705–R774, Jul. 2005.

[114] A. Shahriari, M. Hermes, and V. Bahadur, "Electrical control and enhancement of boiling heat transfer during quenching," *Applied Physics Letters*, vol. 108, no. 9, pp. 091 607–6, Mar. 2016.

[115] S. Ming-Heng, J. Ma, and W. Bu-Xuan, "Analysis on hysteresis in nucleate pool boiling heat transfer," *International Journal of Heat and Mass Transfer*, vol. 36, no. 18, pp. 4461–4466, 1993.

[116] D. W. Fuerstenau, "Equilibrium and nonequilibrium phenomena associated with the adsorption of ionic surfactants at solid–water interfaces," *Journal of Colloid and Interface Science*, vol. 256, no. 1, pp. 79–90, 2002.

[117] C. Lo, J. S. Zhang, A. Couzis, P. Somasundaran, and J. W. Lee, "Adsorption of Cationic and Anionic Surfactants on Cyclopentane Hydrates," *The Journal of Physical Chemistry C*, vol. 114, no. 31, pp. 13 385–13 389, Aug. 2010.

[118] C. A. Lucy and R. S. Underhill, "Characterization of the cationic surfactant induced reversal of electroosmotic flow in capillary electrophoresis," *Analytical Chemistry*, 1996.

[119] I. M. Banat, "Biosurfactants production and possible uses in microbial enhanced oil recovery and oil pollution remediation: A review," *Bioresource Technology*, vol. 51, no. 1, pp. 1–12, Jan. 1995.

[120] I. Kralova and J. Sjöblom, "Surfactants Used in Food Industry: A Review," *Journal of Dispersion Science and Technology*, vol. 30, no. 9, pp. 1363–1383, Sep. 2009.

[121] J. Falbe, *Surfactants in Consumer Products: Theory, Technology and Application*. Springer Berlin Heidelberg, 2012.

[122] M. Muradoglu and G. Tryggvason, "A front-tracking method for computation of interfacial flows with soluble surfactants," *Journal of Computational Physics*, vol. 227, no. 4, pp. 2238–2262, Feb. 2008.

[123] C. Gerardi, J. Buongiorno, L.-w. Hu, and T. McKrell, "Study of bubble growth in water pool boiling through synchronized, infrared thermometry and high-speed video," *International Journal of Heat and Mass Transfer*, vol. 53, no. 19-20, pp. 4185–4192, Sep. 2010.

[124] ——, "Infrared thermometry study of nanofluid pool boiling phenomena," *Nanoscale research letters*, vol. 6, no. 1, p. 232, Jan. 2011.

[125] N. Watanabe, S. Koyama, and H. Imoto, "Thermal decomposition of graphite fluoride. I. Decomposition products of graphite fluoride,(CF) n in a vacuum," *Bulletin of the Chemical Society of Japan*, vol. 53, no. 10, pp. 2731–2734, 1980.

[126] I. Mudawar, "Assessment of high-heat-flux thermal management schemes," *IEEE Transactions on Components and Packaging ...*, 2001.

[127] S. G. Kandlikar, "Fundamental issues related to flow boiling in minichannels and microchannels," *Experimental thermal and fluid science*, vol. 26, no. 2, pp. 389–407, 2002.

[128] W. R. Salzman. Dynamic Texbook of Physical Chemistry. [Online]. Available: http://cbc.arizona.edu/ salzmanr/480a/480ants/opensys/opensys.html

[129] L. D. Landau and E. M. Lifshitz, *Electrodynamics of Continuous Media*. Oxford, New York: Pergamon Press, 1960.

[130] U. Kaatze, "Complex permittivity of water as a function of frequency and temperature," *Journal of Chemical & Engineering Data*, vol. 34, no. 4, pp. 371–374, 1989.

[131] C. L. Tien, "A hydrodynamic model for nucleate pool boiling," *International Journal of Heat and Mass Transfer*, vol. 5, no. 6, pp. 533–540, Jan. 1962.